The SPEDE electron spectrometer

Thesis submitted in accordance with the requirements of
the University of Liverpool for the degree of Doctor in Philosophy
by
George G. O'Neill

October 2016

When old age shall this generation waste,
Thou shalt remain, in midst of other woe
Than ours, a friend to man, to whom thou say'st,
"Beauty is truth, truth beauty,"—that is all
Ye know on earth, and all ye need to know.

John Keats
Ode on a Grecian Urn (1820)

Acknowledgement

To begin, I would like to pay thanks to Prof. Peter Butler for the opportunity to work on the development of SPEDE, as well as for all the guidance, supervision, and knowledge that I have gained from working under him during my PhD. As the last in the long line of his many PhD students, I am immensely grateful.

Thanks should also be given to Dr. Janne Pakarinen, who has spearheaded the development of this spectrometer, and who I would have been at a loss without during my time in Finland and beyond. I hope this work has contributed to make his life at least a little easier! Thank you also to the rest of the SPEDE collaboration, especially to Jim Thornhill & Dave Wells for the construction of the spectrometer and helping me diagnose many initial problems in Liverpool.

There are many other people I should thank across the nuclear physics community for all their help in many aspects of my work, and although there are too many to list I hope they know I appreciate all their help and I look forward to working with them further in the future. One name however is particularly important to note here; Dr. Liam Gaffney. From the moment I started at Liverpool, he has guided me through the last 4 years, and the support offered is immeasurable, and to have someone like him always on hand to answer any of my many questions has been fantastic. Not only physics, the beer, cycling, and waffles (sans ice-cream) have been fantastic too; Liam, I am proud to call you my friend, and owe you at least one pint!

The other staff and students who are part of the Liverpool Nuclear Physics group (and also members of HEP) have been fantastic, and are too many to mention; although most time was not spent on physics, rather at the pub, playing football, or talking about all things bikes, it has always been a welcome distraction and I am glad to have made some close friends from members old and new, so to the Liverpool contingent, thank you. A special mention for Dr. Mark Drummond, especially for he & Úna giving me a place to stay when I was popping back up to Liverpool to finish everything off; same goes for Jon & Soph, and Hayley & Darren!

I must also acknowledge the STFC for their financial support, and for the many trips

abroad to develop my research skills in laboratories and workshops across Europe.

Thanks also to those at the University of York for allowing me to work for a couple of weeks and get back to normality during a difficult period of my studies.

I must also thank the Nuclear Spectroscopy Group at the University of Jyväskylä It has been essential during my development as an experimental physicist, and I had a great time, in a truly beautiful country. To have the opportunity to work in an always-active laboratory was an excellent experience, and to all my friends there, both from within physics and outside, including Otto, Marcus, Jorg, Hanna (whose friendship was especially appreciated during the more difficult periods), and many others, I will attempt to thank you with the 'vähän suomea' I learnt; Kiitos paljon, olen iloinen että olemme tutustuneet. Ilmatyynyalukseni on täynnä ankeriaita.

For the rest of the gang, there are too many languages for you all and I speak none, but Felipe, Giovanni, Laura, Mike etc...thanks for making the time there so great, may we meet again! To others closer to home, Russ & Alex, Kieron, Lee & family, Chris, Jamie, Rob, Joe, Luke, Andy, Toby, Simon & Joe A, Chrissi, and Emma, thanks for giving me a life outside physics too! The same goes for those across who's path I've been fortunate to come across in more recent times who made time fly by, and kept me sane when finishing the write up; your company was most excellent.

Finally, to my family. My many uncles, aunts, cousins, and grandma, for always having an open door for me, and making sure I stayed grounded (certainly, I'll never be allowed to forget Barcelona). To Charlotte, Gabriella, Rebecca, and Clarissa; you cheer me up more often than you know with your nonsense, and it has made me very happy to watch you all grow up and start making your own paths in life. I am proud of you all, and I hope I provide some inspiration. I am always here for you. To my late father Danny (08/10/1959-11/06/2014); I finally finished the PhD! It would not have been possible without you making sure I had the computing knowledge I have relied upon time and time again. We all miss you. A huge thank you to my grandfather Keith; you piqued my curiosity with the trips when I was younger, and I am not sure I have ever had a discussion with you I have not enjoyed. I certainly would not have started down this route if it were not for you, and I hope your faith in me has been rewarded. You instilled in me a thirst for knowledge which has yet to be quenched.

Last but not least, a separate paragraph is needed for my mother, Heather, who is an absolute inspiration, not only to me but my sisters, and probably countless others. How you managed to cope with all of us, and dad's illness, made us all realise we could do anything. More so than anyone else, this thesis is a result of your ability to always have an answer to my questions as a child, and even now in my mid-twenties; it is just one example of your constant unconditional support. All the obstacles I have overcome during my studies have been as a result of your stubbornness to never be stopped by anything. Thank you so, so much.

Abstract

This thesis presents SPEDE (SPectrometer for Electron DEtection) and documents its construction, testing and performance during commissioning at Jyväskylä, Finland, before deployment at the HIE-ISOLDE facility at CERN coupled with the MINIBALL array to perform in-beam electron-gamma spectroscopy using post-accelerated radioactive ion beams. Results from the Coulomb excitation of ^{221}Rn in 2012 are presented as an example of the need for the construction of a device like SPEDE. In-beam testing and initial commissioning experiments with stable beams took place in four stints during November, February, and May 2015, coupled with detectors from JUROGAMII.

This spectrometer will help aid in fully understanding exotic regions of the nuclear chart such as regions with a high degree of octupole deformation, and in those nuclei exhibiting shape coexistence.

For the first time, electron spectroscopy has been performed at the target position from states populated in accelerated nuclei via Coulomb excitation. The FWHM of SPEDE is approximately 7 keV at 320 keV, and Doppler correction was possible to improve Doppler broadened peaks to a resolution of 8.9 keV at a peak position of 186 and 196 keV.

The results are intended to give the reader a full understanding of the detector and electronics, as well as the performance, capabilities, and usefulness of the spectrometer, both in simulated and in real-world situations.

Contents

List of Equations

List of Figures

List of Tables

1 Motivation

"The way the mind will lean under stress is strongly influenced by training."

1.1 Introduction

There are four fundamental forces of nature described by our current knowledge of physics (although the existence of a fifth force is often speculated [1]). From weakest to strongest these are gravity, the weak nuclear force, electromagnetism, and the strong nuclear force.

The strong interaction, responsible for the strong nuclear force, is carried by gluons, binding quarks together within mesons and baryons. It is also responsible for binding nuclei together, with gluons bound within virtual π and ρ mesons transmitting a force within the quantum mechanical system. Nuclear physics attempts to understand and describe the strong nuclear force, to further humanity's understanding of our universe.

In the Rutherford model of the atom [2], which superseded the 'plum pudding' model by J. J. Thomson, an inner positively-charged nucleus of protons surrounded by a cloud of negatively-charged electrons, was developed in 1911 by Ernest Rutherford, following an experiment at the University of Manchester, U.K., by Hans Geiger and Ernest Marsden two years prior [3]. In 1920, Rutherford suggested particles with a neutral charge were also present in the nucleus [4], which were later detected in 1935 by James Chadwick at the Cavendish Laboratory, Cambridge [5]. Parallel to this, developments were made in the new field of quantum mechanics. Ultimately, these discoveries and theories led to the nuclear shell model, proposed by Dmitry Ivanenko and Gapon in 1932 [6], which structures the nucleus within energy levels using the Pauli exclusion principle [7]. The energy well that is binding nucleons together can be described (in a simple sense) by a Woods-Saxon potential, and through modification of this potential by incorporating a spin-orbit interaction 'magic numbers' can be predicted which give the number of nucleons needed for the most stable spherical nuclei [8].

As the number of nucleons within the nucleus increases, collective modes begin to dominate the shape of the nucleus, resulting in quadrupole, octupole, hexadecapole, dotriacontapole, and so on, deformations generally (but not exclusively) decreasing in magnitude as order increases [9]. Theorising the shape and exact energy level values of excited nuclei is challenging due to the many-body nature and finite size of the nucleus, and so therefore experimental information is needed across the nuclear chart to refine and determine model parameters. As a requirement for these experimental searches, detector and computational technology is continually improved, resulting in direct ‘real-world’ applications beyond a fundamental understanding of the world in areas such as chemical synthesis, environmental monitoring and healthcare.

In the last decade, there has been a number of radioactive ion beam (RIB) facilities that have come online, such as REX-ISOLDE (recently upgraded to HIE-ISOLDE) at CERN in Switzerland, ISAC at TRIUMF in Canada, and RIBF at Riken in Japan [10]. These allow previously unexamined areas of the nuclear chart to be studied in detail, but typically have a relatively low number of particles per second reaching the target position, compared to stable beam facilities (10^4-10^6 compared to rates as high as 10^{10}) [11]. Nevertheless, RIBs provide a new and exciting look on untouched areas of nuclear structure pushing current theories and models to their limits.

The consequence of the lower rates when using RIBs is that information needs to be extracted from fewer nuclei available, meaning examining levels or reactions that are populated with a low cross-section is more difficult. This is combined with the fact that many radioactive nuclei have limited existing spectroscopic information known, especially nuclei of odd-mass. Whilst there are several existing γ-ray array spectrometers that have been combined with the RIB facilities mentioned, such as MINIBALL, TIGRESS, and CNS-GRAPE respectively [12], there are currently no RIB facilities where γ-ray detection instruments are combined with those for detecting electrons to perform the spectroscopy of both simultaneously in-beam.

Information about nuclear structure can be obtained by looking at the resulting spectrum from the radiated particles emitted during the decay of a nucleus to a lower energy state. This includes emissions such as high-energy photons (γ-rays), α particles, protons, electrons, and so on, first identified by Madame Curie [13]. However, there are only three principal ways a nucleus can decay without changing the proton or neutron number; that is, they are electromagnetic decay processes. These are either internal pair production (which can be largely ignored apart from high energy decays over twice the mass of an electron at 1.022 MeV), γ-ray emission, or internal conversion.

1.2 On the nucleus

The atomic nucleus is a quantal many-body system, and so the properties of this system are determined by the number of protons and neutrons making it up. Macroscopic behaviour is however exhibited, and nuclear shapes are described by collective parameters and transition strengths. These can be measured both directly and indirectly by several methods suited for various different applications and areas of the nuclear chart.

Overall, the shape of the nucleus is given by

$$R\left(\theta,\phi\right) = R_0\left(1 + \sum_{\lambda,\mu} \alpha_{\lambda\mu} Y_{\lambda}^{\mu}\right) \qquad \text{(eq. 1.1)}$$

where R is the radius given as a function of the angles θ and ϕ, R_0 is the radius of a sphere with the same volume as the nucleus, Y_{λ}^{μ} are the normalised spherical harmonics, and $\alpha_{\lambda\mu}$ are expansion coefficients (which are the polar coordinate transformation of the deformation parameter β_{λ}). With axial symmetry, all coefficients with $\mu \neq 0$ are also 0. With reflection symmetry, all terms other than those where λ is even vanish.

The intrinsic multipole moment is related to the deformation parameter (to first-order, and where the multipolarity $\lambda \geq 1$), by

$$Q_{\lambda} = \frac{3R_0^{\lambda}\beta_{\lambda}}{\sqrt{\left(2\lambda+1\right)\pi}}. \qquad \text{(eq. 1.2)}$$

Single-particle effects are important for the matrix elements used to determine the dipole operator, but for greater multipolarities the collective nature of superimposed nucleons dominates [14].

1.3 Example applications: Octupole-deformed nuclei

Octupole deformation is expected to be greatest in regions just above closed shells, with proton or neutron numbers $\simeq$ 34, 56, 88 and 134, as octupole correlations are an essential contribution to the mean field interaction immediately above closed shells where (N, j, l) intruder orbitals interact strongly with the $(N-1, j-3, l-3)$ natural parity states. In these regions, the Fermi level is situated between these orbitals [15], with the strength of the octupole-octupole interaction dependent on the matrix elements of Y_3^0 between these single-particle states. As the energy difference between the interacting orbitals is minimised, and the density of the states is maximised, the interactions become strongest, implying octupole correlations increase with the mass of the nucleus, and are enhanced for doubly magic nuclei, as seen in ^{144}Ba [16].

The reflection asymmetry expected in octupole deformation gives rise to a pear shape (the nuclei are axially symmetric), which itself implies the centre of mass does not lie at the centre point of the nucleus spatially, and is instead displaced to one end. The centre of charge is also displaced from the centre of mass, as charged particles gather in the area where the radius of the electric potential contour is smallest, which is at the narrow end of the nucleus as it tapers [17]. This octupole shape presents itself with regards to the nuclear structure by having strong E1 and E3 transitions, due to the number of low-lying states with opposite parity, first observed in heavy nuclei such as ^{218}Ra [18] and ^{222}Th [19].

Nuclei exhibit static deformation due to spontaneous symmetry breaking; the eigenvalues of a single-particle Hamiltonian around the Fermi level are degenerate, but due to instabilities from shape vibrations, one state will always become lower in energy. The resulting asymmetric shape can be attributed to an odd-multipolarity parity violation of the weak interaction. One signature of octupole deformation then, the presence of strong E1 (dipole) transitions, is induced by the presence of an intrinsic electric dipole moment [20]. If a nucleus is permanently octupole deformed, all terms in eq. 1.1 except α_{20} and α_{30} vanish.

By using Coulomb excitation, the matrix element of the collective state can be measured directly in even-even nuclei via the reduced transition probability $B\left(E3; 0^{+} \rightarrow 3^{-}\right)$, and is the only way to provide unambiguous and direct evidence of octupole collectivity. This was done at the ISOLDE facility on ^{220}Rn and ^{224}Ra showing for the first time a permanent octupole deformation [21]. Pursuing odd-mass nuclei in particular is of interest due to parity doublets lying very close together in energy [22], enhancing the Schiff moment leading to a possible non-zero electric dipole moment (EDM).

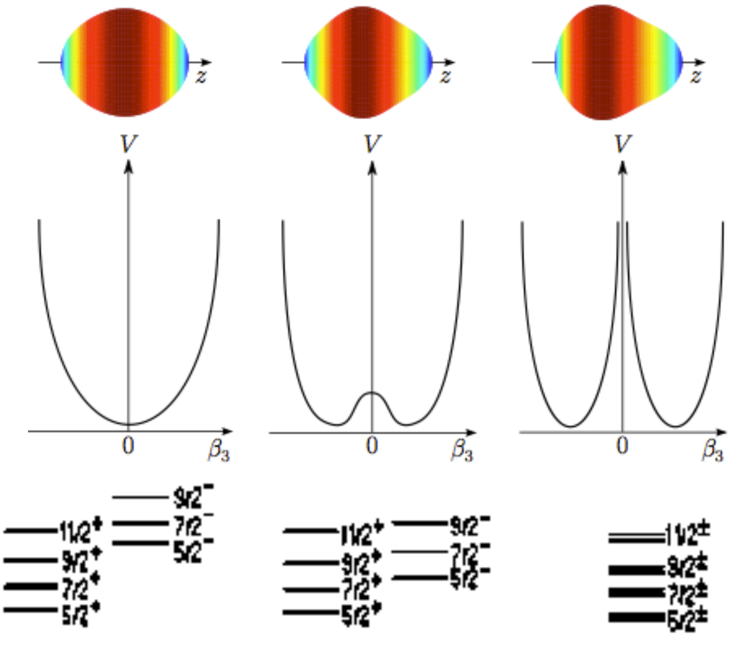

Figure 1.1: Nuclear potentials as a function of the octupole deformation parameter β_3 [23]; from left-to-right, a quadrupole deformed nucleus with an octupole vibration averaging zero, an intermediate case with a small potential barrier separating two degenerate deformed minima and an ideal rigid deformation. Red colours indicate the shape raising out of the page, with bluer colours representing areas less raised.

The Schiff theorem states that for a system made of point-like, charged particles which interact with each other and with an arbitrary external field, the electronic shielding is complete, and therefore, theoretically, in a neutral atom, the nuclear EDM is screened, however the finite size of the nucleus can break this. A nuclear Schiff moment can enhance the effect, which can lead to a non-zero static atomic EDM, implying (separately) charge-parity-, and time-, symmetry violation. This in turn provides good test extensions of the standard model that violate the symmetry. Reflection-asymmetric nuclear shapes enhance the Schiff moment by approximately 3 orders of magnitude [24], and so they offer much greater increased sensitivity for EDM searches.

The Schiff moment S is further enhanced by odd-mass nuclei in the octupole region, where parity-doublet splitting occurs, and is given by

$$S = -\frac{2J}{J+1}\frac{< \hat{S}_Z >< \hat{V}_{PT} >}{\Delta E}. \qquad \text{(eq. 1.3)}$$

where J is the total angular momentum of the nucleus, $\hat{V}_{PT}$ is the nucleon-nucleon interaction violating parity and time, ΔE is the difference in energy between the two states making up the parity doublet and $\hat{S}_Z$ is an operator dependent on the mean-square charge radius and number of protons in the nucleus.

An illustration of the effect of the octupole deformation parameter β_3 can be seen in Figure 1.1 for an odd-mass nucleus. Transitions between the doublets seen in odd-mass octupoles would have a very low energy, around 50 keV or lower, and are more likely to occur in heavier nuclei. The analysis of these odd-mass nuclei is complicated by the effect of the single valence particle on the collective effect of the coupled nucleons [25], thus experimental evidence is needed to provide limits on theoretical models. The parity doublets expected enhance the Schiff moment by a factor of 10^3. Leander and Chen [26] have had some success previously in calculating decoupling parameters using a reflection-asymmetric particle-plus-rotor model, to the same order, assuming non-zero β_3. A detailed review of odd-A actinide nuclei, and other nuclei around this region, is provided by Leander and Sheline [27], as well as Sheline and Sood [28] and others.

1.4 Example applications: Shape-coexistence

In the case of $0^+ \to 0^+$ $E0$ transitions, which are observed in shape coexistence, there is no angular momentum to give to an emitted photon (which must have a spin of 1); since there is no angular momentum available to the photon, any emission would be a violation of the conservation of angular momentum and break rotationally-invariant symmetry. This leaves two principal electromagnetic decay processes, the first being internal pair production, where an electron-positron pair are created and are emitted back-to-back; this requires a transition energy of at least 1.022 MeV, which is twice the rest-mass energy of an electron (0.511 MeV). The other possibility is for internal electron conversion (although higher order processes such as two-photon decay are possible, but rare [30]). Low-lying 0^+ excited states are indicative of shape coexistence, and so the importance of detecting $E0$ transitions is seen again as they can only proceed by internal conversion. The strengths of these transitions depend on the mixing of configurations with differing mean-square charge radii, and give a model-independent perspective of the 0^+ configurations resulting in the transition [31]. A prime example of shape coexistence can be seen with ^{186}Pb, as seen in Figure 1.2.

Shape-coexistence is a stringent test of microscopic nuclear models and mean-field descriptions [32], as it involves the complex interactions of nuclei in competing orbitals typically in regions far away from the stable nuclei where the empirical shell model was formed. A thorough review is undertaken by Heyde and Wood [33], where it is argued that modelling shape coexistence 'is arguably one of the greatest challenges faced by theories of nuclear structure'.

Shape coexistence is apparent due to a mixture of the stable, spherical shape of closed shells and sub-shells coupled with residual interactions between protons and neutrons driving the nucleus into a deformed shape. Regions of maximum coexistence tend to lie therefore far away from closed shells, at the 'magic numbers', where shell gaps have the greatest influence. The interpretation of low-energy vibration of nuclei has been proven incorrect in cadmium isotopes, and a reliable characterisation of these nuclei is needed to interpret the data in a cromulent way. Although some regions of shape-coexistence which lie along one stability line, such as Z $\simeq$ 50, are easily accessible, many other regions require the use of RIBs, especially to determine whether the emerging picture (that coexisting

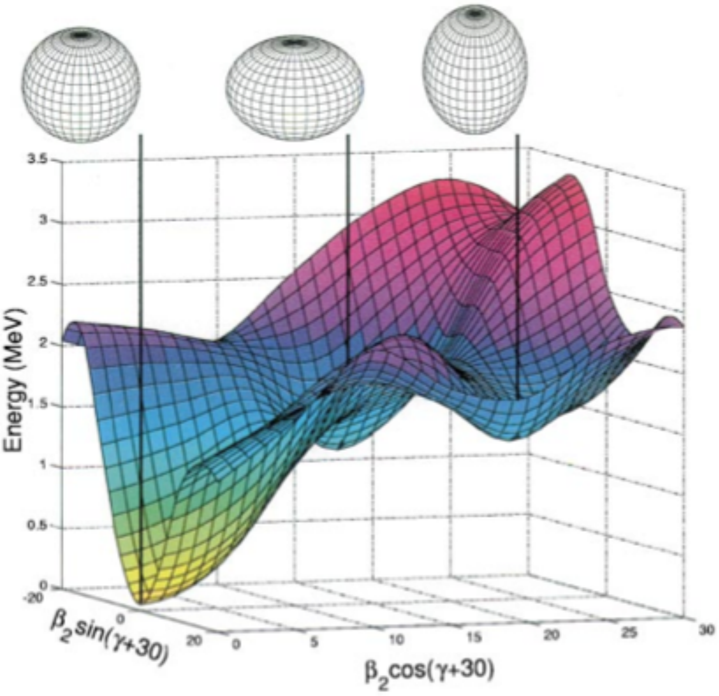

Figure 1.2: Calculated potential energy surface of ^{186}Pb [29]. Spherical, oblate and prolate shape deformations are respectively indicated from left to right by the thicker vertical lines.

structures are present in all nuclei) is true.

1.5 Why electron spectroscopy?

The benefits of an electron spectrometer compared to one used for γ-rays are apparent when looking at the internal conversion coefficient, α, which is given by

$$\alpha = \frac{\sum \textit{de-excitations via electron emission}}{\sum \textit{de-excitations via } \gamma\textit{-ray emission}} = \sum \alpha_i \qquad \text{(eq. 1.4)}$$

where the subscript i indicates the partial internal conversion coefficient, obtained from the conversion electrons from each individual electron shell (K, L, M, ...), or transition types ($E1$, $M1$, $E2$, ...). As the proton number Z of a nucleus increases, so does α, and the same is true for lower-energy decays; as the transition energy between two levels tends to 0, α tends to infinity:

$$\lim_{Z\to\infty,\ E\to 0} \alpha = \infty. \qquad \text{(eq. 1.5)}$$

This is of particular interest when looking at radioactive beams not only because these are often beams of heavy nuclei, and therefore high Z, but because some of these nuclei have low energy transitions of particular interest, such as in the octupole-deformed region, where low-energy transitions between parity doublets can be expected to be observed [34], or in regions where shape-coexistence is observed, where decays between $0^+ \to 0^+$ levels within the same nucleus are generally only observable by use of an electron spectrometer (unless the transition energy is over 1.022 MeV, where internal pair production can occur, or other rare instances), as a photon has a spin of 1 $\hbar$ [35] and therefore cannot be emitted for an $E0$ decay. In general, since octupole nuclei are predicted to have low-lying states, transitions between them are are highly converted, and thus often decay with the emission of a conversion electron, the likelihood of which only increases when considering odd-mass octupoles due to the parity doublets. In the actinide region, with Z $\simeq$ 88, there are currently very few measurements, and even fewer of the odd-mass nuclei in this region, due to the particular challenges odd-mass nuclei present. Therefore the need of an electron spectrometer when studying these nuclei is apparent. Proposals have been submitted to study this region further using radioactive beams at the ISOLDE facility in CERN, for which work presented here on ^{221}Rn was done to test the feasibility of such an experiment, and which is presented later in this thesis. Although no results of shape-coexistence will appear in this thesis, it is an important application of SPEDE in the future to study this region in more detail than has been possible until now with RIBs.

Additionally, the multipolarity and parity are directly observable from subshell ratios when looking at the resulting electron spectra, as is the possibility to directly access mixing ratios [36]. The transition multipolarities can be determined either by comparing α directly to theoretical predictions, or simply looking at the ratio between partial conversion coefficients. Similarly, looking at the ratio of α from differing transition types (commonly $M1$, $E2$) will directly give the value of the appropriate mixing (typically $E2/M1$).

SPEDE (SPectrometer for Electron DEtection) is a 500 μm thick 24-segmented n-type silicon detector that, through the detection of electrons, will yield information on transitions in nuclei excited via Coulomb excitation direct from the ground state. By being combined with the MINIBALL it will help to help unlock the secrets of nuclei and further collective knowledge in nuclear physics. Other internal conversion detectors coupled with γ-detecting facilities are under development, such as SPICE (SPectrometer for Internal Conversion Electrons) at TIGRESS [37], but SPEDE is the first internal conversion spectrometer studying beam excitation situated at the target position without electron transport.

This thesis will deal with the detection of electrons emitted during the internal conversion process using SPEDE, including the methodology of the work, the spectrometer design and simulated performance, and the results of in-beam commissioning experiments from the JYFL laboratory, Finland, using decays from nuclear states populated via Coulomb excitation, as well as results from a Coulomb excitation experiment on ^{221}Rn used to show direct motivation for this work.

2 Experimental methods

"Philosophy cannot be taught; it is the application of the sciences to truth."

2.1 Nuclear transitions

Nuclei in an excited state can decay by various pathways. However, for an internal transition, where a nucleus does not change isotope, three first-order processes are possible; internal pair production (for transitions with an energy over 1.022 MeV), γ-ray emission, or internal conversion. Internal transitions result in the emission of radiation with multipolarity L, corresponding to a change of state of a nucleus, as shown in eq. 2.1

$$|J_f, \pi_f\rangle = L\,|J_i, \pi_i\rangle \qquad \text{(eq. 2.1)}$$

where J is the total angular momentum of the state, π is the parity of the state, and the subscripts i and f correspond to the initial and final states respectively.

A series of selection rules apply for electromagnetic transitions. First, angular momentum must be conserved [38], such that $\vec{J_i} = \vec{J_f} + \vec{L}$. This leads to the fact that the allowed values of L are such that $|J_i - J_f| \leq L \leq |J_i + J_f|$. Secondly, parity must also be conserved; this leads to an equation where $\pi\left(TL\right) = \pi_i \pi_f = \left(-1\right)^{L+t}$, with $T \in E, M$, and $t \in 0, 1$ with a one-to-one correspondence.

2.1.1 Internal conversion

SPEDE will be used to detect electrons emitted during the process of internal conversion. Internally-converted electrons are monoenergetic electrons emitted due to a coupling of the electron and nuclear wavefunctions. This is then typically followed by an X-ray, with the vacancy in the atomic shell of the atom filled by an electron from a higher shell if available. This energy of the internally converted electron is given by

$$E_{IC} = E_i - E_f - E_b \qquad \text{(eq. 2.2)}$$

where E is energy, and the subscripts IC, i, f and b correspond respectively to the energy of the ejected electron, the energy of the initial state of the excited nucleus, the energy of the final state of the nucleus, and the binding energy of the atomic shell that the electron was ejected from.

It is important to note that the internally converted electron differs to that seen in, for example, β decay. Rather than a continuous distribution in emission energies, an internally converted electron is seen as a single, sharp peak, as seen in Figure 2.1. Three peaks above the β background can be seen, which correspond to the K-shell, L-shell, and (in the right tail of the L-shell peak) M-shell conversion electrons. The counts in these peaks show that the partial conversion coefficient varies for different electron shells and indeed sub-shells.

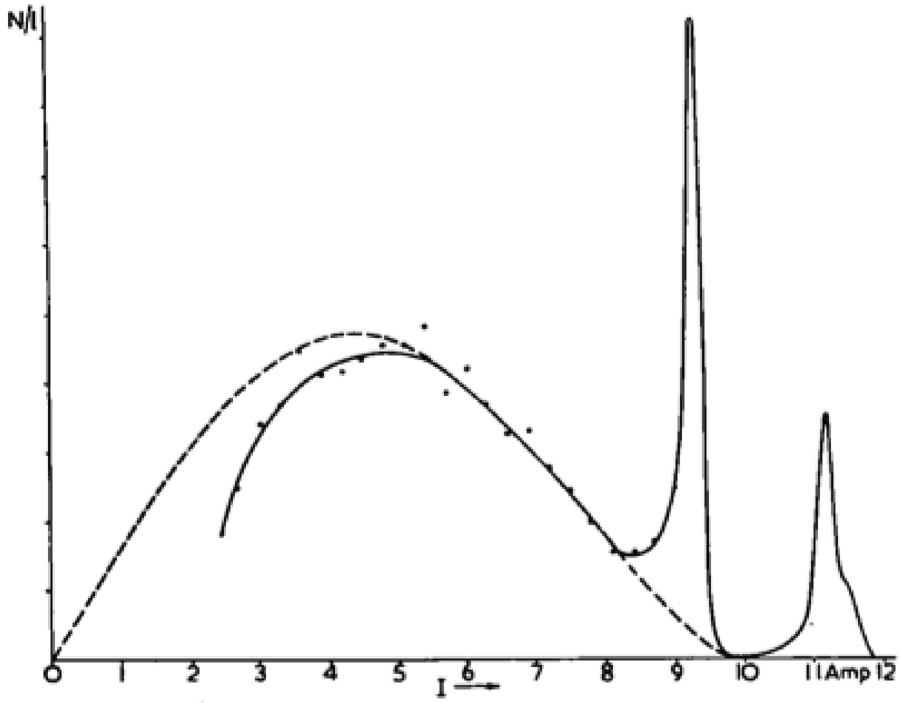

Figure 2.1: This plot shows the decay spectroscopy of ^{203}Hg. A broad peak can be seen, corresponding to β particles, with three peaks from internally converted electrons observable on the right-hand side [39].

The internal conversion process increases in likelihood as the mass of the nucleus increases; since atomic radius is generally proportional to number of nucleons, it is apparent to see that an electron is more likely to be influenced by nuclear effects. The probability also increases with multipolarity of the nuclear transition due to the fact that it is easier for an electron to carry more angular momentum from a nucleus and is thus the quicker, and therefore preferred, way for the nucleus to fall into the minimum of its potential well. The likelihood compared to γ-ray emission is dictated by eq. 1.4. An example of the internal conversion coefficient magnitude as a function of energy is demonstrated for a radon nucleus, using theoretical values, in Figure 2.2. This dependence on multipolarity means that the difference in spin and parity of a nucleus can be obtained directly by comparing either the total internal conversion coefficient, or the partial internal conversion coefficients, against theoretical values or each other to obtain an unequivocal transition type, therefore inplying the nuclear state that the detected electron could be emitted from.

Since internal conversion requires the emission of an atomic electron, there is a dependence on the atomic shells of the atom being filled. In a fully-ionised atom, with a net charge of Z, internal conversion could not occur since there are no electron wavefunctions for the nucleus to overlap with. Likewise, if the energy between the two states is higher than the binding energy of an electron shell, emission cannot occur from that shell. Therefore, nuclear transitions which lie below the binding energy of the innermost electrons in the K-shell, any converted electrons must come from a higher shell, such as one of the L shells. However, these are less likely to couple to the nucleus due to the quantum mechanical wavefunction of the electron-nucleus system resulting in the electrons spending less time in and around the nucleus, even though the number of electrons in higher-order atomic shells is greater than the two present in the K-shell. This is apparent from examining the real representations of the spherical harmonics, where increasing the quantum number for the electron shell results in a probability distribution of electrons which are increasingly further displaced from the origin.

2.1.2 $E0$ transitions

Monopole transitions ($L = 0$) cannot proceed via γ-decay due to the photon having unit intrinsic spin. A $0^+ \rightarrow 0^+$ decay then is strictly forbidden with the emission of only one photon. However, it is possible to observe an $E0$ transition via an internally converted electron.

For transitions between states, the wavefunctions must overlap in order for the configuration mixing to occur [41]. There is also a requirement that $\Delta K = 0$, and thus provide a probe of the K quantum number of a band (the projection of the total angular momentum J along the symmetry axis of the nucleus). $E0$ transition strengths offer a model independent description of off-diagonal matrix elements of the mean-square charge radius operator. Therefore, the mixing of configurations with different charge radii r^2 greatly influences the $E0$ transition strength, making them important probes of deformed nuclei. The transition strength ρ^2 of $E0$ decays can be expressed in terms of differences in r^2 or quadrupole deformation β^2 via [42]

$$\rho^2\left(E0\right) = \left(\frac{3Za\sqrt{1-a^2}\Delta\left\langle\beta^2\right\rangle}{4\pi}\right)^2 = \left(\frac{Z^2a\sqrt{1-a^2}\Delta\left\langle r^2\right\rangle}{R_0^4}\right)^2 \qquad \text{(eq. 2.3)}$$

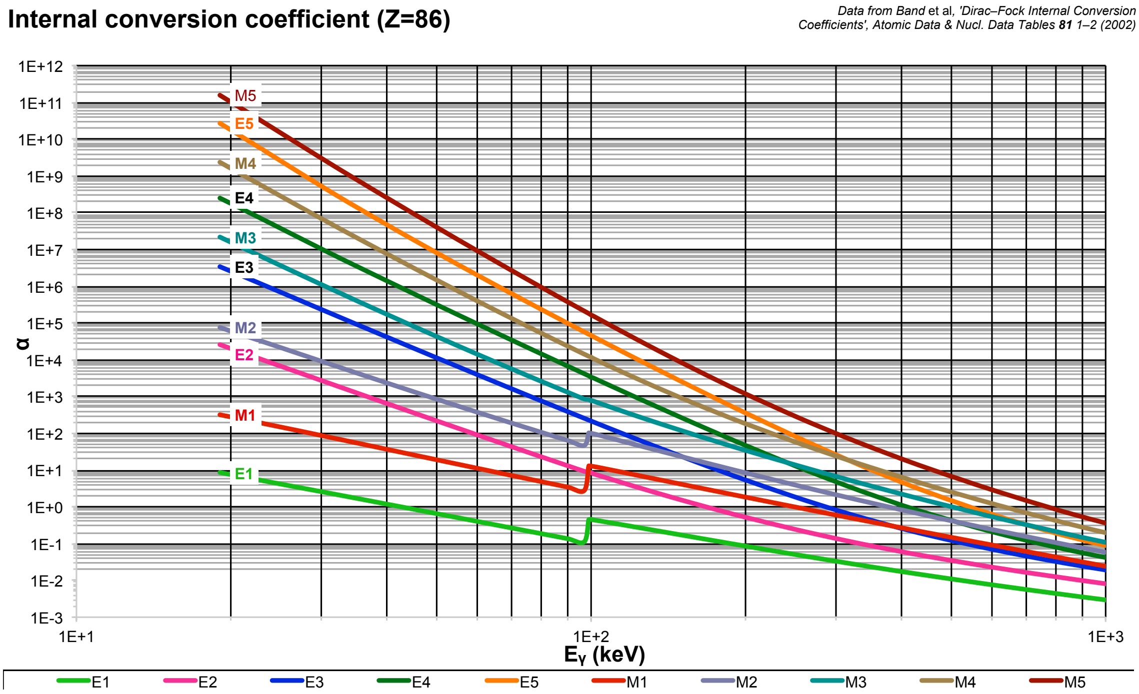

Internal conversion coefficient (Z=86)

*Data from Band et al, 'Dirac–Fock Internal Conversion Coefficients', Atomic Data & Nucl. Data Tables **81** 1–2 (2002)*

Figure 2.2: Theoretical values for internal conversion in radon, as a dependence of energy, and also multipolarity of the transition. Note the kinks in E1, M1, and M2 transitions, which are due to the K-shell binding energy. Data is obtained from calculations used for the BrIcc program [40].

where Z is the proton number of the nucleus, R_0 is the nuclear radius, and a is the mixing amplitude of the coexisting configuration.

A $0^+ \rightarrow 0^-$ transition violates parity rules with the emission of only one quanta, but can proceed via two photons or two conversion electrons being emitted. A magnetic monopole is not known to exist with currently known physics, although suggestions have been made that an $M0$ transition could occur with a cascade of virtual $E1$ and $M1$ pairs [43].

2.1.3 γ-ray emission

High energy photons are emitted by most radioactive sources and excited nuclei, for all transition multipolarities greater than one, due to the unit nature of the spin on a photon. These photons can be lower in energy than X-rays; however, γ-rays are categorised as being emitted from the nucleus, rather than as a consequence of electric transitions in atomic shells. It is typically the dominant mode of decay within excited nuclei. The energy of the detected photon is not the exact transition energy between states; to conserve momentum, the nucleus must have some recoil energy when emitting a photon, but this correction is of the order of 10^{-5} and so can be neglected for all but the most precise of measurements.

The likelihood of a high-order transition decreases with increasing L. Magnetic transitions are also slower. Assuming a spherical nucleus, so-called Weiskopff estimates [44] can be obtained for the transition rate of each state. For the fastest transitions, these are

$$\begin{gathered}\lambda(E1) = 1.0 \times 10^{14} A^{\frac{2}{3}} E^3 \\ \lambda(E2) = 7.3 \times 10^{7} A^{\frac{4}{3}} E^5 \\ \lambda(M1) = 5.6 \times 10^{13} E^3 \\ \lambda(M2) = 3.5 \times 10^{7} A^{\frac{2}{3}} E^5\end{gathered} \qquad \text{(eq. 2.4)}$$

where E is the energy of the transition and A is the mass number of the nucleus. These estimates can differ by large amounts according to the structure of the nucleus, such as $E1$ transitions occurring faster in octupole-deformed nuclei.

It is not possible to obtain direct information of the multipolarity of the transition, or of the type, from the detection of a γ-ray, although polarisation techniques can be employed to determine this, by cooling the nuclei to low temperatures, placing them in a magnetic field, or comparing observed distributions from a cascade of previous states. However, high-energy photons are essential to the study of nuclear physics as they are emitted in abundance across the nuclear chart at all energies and masses.

2.1.4 Internal pair production

If the energy difference between states is greater than twice the mass of an electron (1.022 MeV), mass-energy equivalence dictates that a positron-electron pair may simultaneously form, with excess energy given to the particles in the form of kinetic energy. The likeihood of this process increases as the transition energy increases, and is especially important in light elements, which often have large energy differences between states, although the dependence on the proton number otherwise is negligible. Pair production can occur anywhere within the field of the nucleus [45].

This is a valid process for all transitions, including $E0$, and can be used to determine multipolarities of transitions [46]. Detection can take place by either detecting the emitted positron and electron pair, or by detecting the two photons emitted when the positron annihilates with an electron within the material.

2.2 Coulomb excitation

Nuclei during the in-beam experiments used to test SPEDE were excited via Coulomb excitation. A nucleus can be excited from the ground state by a time-dependent electromagnetic field generated by passing another nucleus. This process is Coulomb excitation. Ensuring the energy used is below the Coulomb barrier, the interaction is purely an electromagnetic one, a force which is well understood. By keeping the energy low, distance between the nuclei involved in the reaction remains large enough that any effects from the nuclear forces can be ignored, since the range of the strong nuclear force is $\simeq 10^{-15}$ m, the size of a typical nucleus, and the range of the weak nuclear force around a thousand times smaller, with a range $\simeq 10^{-18}$ m.

Due to the computation required to complete a full quantum mechanical treatment of the nucleus, a numerical approach is needed. First- and second-order perturbation theory is sufficient for one- or two-step excitation, but is of no use when considering the population of many states with heavy ions. The equations describing this are summised here. For an exhaustive treatment, refer to Alder and Winther [47].

Coulomb excitation can be approximated using a semi-classical method, similar to that of Rutherford scattering, given by

$$\frac{d\sigma}{d\Omega} = \left(\frac{Z_p Z_t e^2}{8\pi\epsilon_0 m v^2} \right)^2 \csc^4 \frac{\theta}{2} \qquad \text{(eq. 2.5)}$$

where Z_p and Z_t are the proton number of the projectile and target respectively, m is the reduced mass of the projectile-target system, v is the velocity of the projectile and θ is the deflection angle in the centre of mass reference frame.

For this classical treatment to be valid, the quantum-mechanical wave packet must be smaller than the distance between nuclei, which requires the Sommerfeld parameter

$$\eta = \frac{\pi b}{\lambda} = \frac{Z_p Z_t \alpha}{\beta} >> 1 \qquad \text{(eq. 2.6)}$$

where b is the distance of closest approach between the projectile nucleus and the target, λ is the de Broglie wavelength of the beam, α is the fine-structure constant and β is the speed of the projectile relative to the speed of light c. The Sommerfeld parameter is a dimensionless quantity that represents the number of exchanged photons needed to force the nuclei on a hyperbolic orbit.

Rutherford scattering trajectories are symmetrical about the point of scatter, and so also requires the scattering to be inelastic. Although this is not true for Coulomb excitation, inelastic scattering can be approximated to elastic scattering if the energy transfer, ΔE, is much smaller than the projectile energy E_p, implying incoming and outgoing energies are similar enough to be treated classically. This results in the condition

$$\frac{\Delta E}{E_p} << 1. \qquad \text{(eq. 2.7)}$$

For heavy-ion beams, such as those that will be typically used with SPEDE at HIE-ISOLDE, the condition on the Sommerfeld parameter is met, and typically, due to the production method and acceleration of the beams, the beam energy is much greater than the excitation energy. Therefore, the semi-classical approximation is valid. The final Coulomb excitation cross-section is then given by a product of the Rutherford cross section σ_R and the probability P_n of exciting a given state $|n\rangle$. Thus, the Coulomb excitation cross-section is

$$\frac{d\sigma_n}{d\Omega} = P_n \frac{d\sigma_R}{d\Omega} \qquad \text{(eq. 2.8)}$$

The collision time in these reactions is of the order of 10^{-21} seconds, around 10^8 times quicker than the nuclear lifetimes of the low-lying states typically involved. Therefore the excitation and subsequent decay can be treated as separate processes. Using this fact, and the knowledge that in the expansion of the electromagnetic potential the mutual multipole-multipole interaction is weak and can be neglected, the Schrödinger equation can be expressed, independently for target and projectile, as

$$ih\frac{\partial}{\partial t}\left|\psi_{1,2}\right\rangle = \left(H^0_{1,2} + V_{1,2}\left(\bar{r}\left(t\right)\right)\right)\left|\psi_{1,2}\right\rangle \qquad \text{(eq. 2.9)}$$

where the V term with an index of 1 represents the monopole-multipole interaction between an unexcited (monopole) nucleus and the excited (multipole) nucleus, and vice-versa with an index of 2. The H term represents the monopole-monopole interaction and determines the time-dependence of the potential by the classical trajectory $\bar{r}\left(t\right)$.

To solve the time-dependent Schrödinger equation given by eq. 2.9, the wavefunction $\left|\psi\left(\bar{r},t\right)\right\rangle$ can be represented as a superposition of individual nucleon wavefunctions $\phi\left(\bar{r}\right)$, along with time-dependent coefficients $a\left(t\right)$, such that

$$\left|\psi\left(\bar{r},t\right)\right\rangle = \sum_n a_n\left(t\right)\left|\phi_n\left(\bar{r}\right)\right\rangle e^{\frac{-iE_nt}{\hbar}} \qquad \text{(eq. 2.10)}$$

where $H^0\left|\phi_n\right\rangle = E_n\left|\phi_n\right\rangle$.

It can be shown (as it is in the GOSIA manual [48]) that the excitation amplitudes a_k, taken into account the orthonormality of the nucleon wavefunctions $\left|\phi_n\right\rangle$ such that $\left\langle\phi_k|\phi_n\right\rangle = \delta_{kn}$, when differentiated by the dimensionless orbit parameter ω (such that $t = \frac{a}{\nu_I}\left(\epsilon\sinh\omega+\omega\right)$, $\epsilon = \sin\frac{\theta}{2}^{-1}$, θ is the centre-of-mass scattering angle, a is half the distance of closest approach if the nuclei collide head on and v_I is the magnitude of the interaction velocity), is given by

$$\frac{da_k}{d\omega} = -i\sum_{\lambda\mu n} Q_{\lambda\mu}\left(\epsilon,\omega\right)\zeta^{\lambda\mu}_{kn}\left\langle I_k\right|\left|M\left(\lambda\right)\right|\left|I_n\right\rangle a_n\left(\omega\right)e^{i\xi_{kn}\left(\epsilon\sinh\omega+\omega\right)} \qquad \text{(eq. 2.11)}$$

where Q represents the dimensionless collision functions for electric or magnetic excitations, $\zeta = \eta_k - \eta_n = \frac{Z_1Z_2e^2}{\hbar}\left(\frac{1}{v_k} - \frac{1}{v_n}\right)$ is the symmetrized adiabaticity parameter that represents the difference in wavenumber between the initial and final states, and the reduced matrix elements replace the multipole operator matrix elements $\left\langle I_sM_s\right| M\left(\lambda,\mu\right)\left|I_fM_f\right\rangle$ via the Wigner-Eckart theorem such that

$$\langle I_s M_s | \, M(\lambda,\mu) \, | I_f M_f \rangle = (-1)^{I_s - M_s} \begin{pmatrix} I_s & \lambda & I_f \\ -M_s & \mu & M_f \end{pmatrix} \langle I_s | \, | M(\lambda) | \, | I_f \rangle \qquad \text{(eq. 2.12)}$$

where $\begin{pmatrix} I_s & \lambda & I_f \\ -M_s & \mu & M_f \end{pmatrix}$ is the 3-j symbol.

The complex expansion coefficients defined by $a_k(t)$ can be expressed before the interaction as $a_k(t=-\infty) = \delta_{k,O}$, where O is the ground state (the typical initial state), and k represents a state of the nucleus. After the collision, the nucleus is then described by the set of $a_k(t=-\infty)$ defining excitation probabilities where $P_k = a_k a_k^*$, before which the excited nuclei can then decay back to the ground state by either γ-ray emission or by internal conversion.

The electromagnetic matrix elements connecting two states can be calculated by using the above Wigner-Eckart theorem in eq. 2.12 for electric transitions, such that

$$\langle I_s | \, | E\lambda | \, | I_f \rangle = \sqrt{2I_f + 1} \, \langle I_f m_f \lambda m_s | I_s m_s \rangle \, Q_\lambda a_\lambda \qquad \text{(eq. 2.13)}$$

where $\langle I_f m_f \lambda m_s | I_s m_s \rangle$ is the Clebsch-Gordan coefficient, and $a_\lambda = \begin{cases} \sqrt{\frac{3}{4\pi}} & \lambda = 1 \\ \sqrt{\frac{2\lambda+1}{16\pi}} & \lambda \geq 2 \end{cases}$. Q_λ is given in eq. 1.2. The strength of an electromagnetic transition can then be defined as

$$B(E\lambda; I_s \to I_f) = \frac{1}{2I_s + 1} | \, \langle I_s | \, | E\lambda | \, | I_f \rangle \, |^2 = \frac{2I_f + 1}{2I_s + 1} \langle I_f m_f \lambda m_s | I_s m_s \rangle^2 \, Q_\lambda^2 a_\lambda^2. \quad \text{(eq. 2.14)}$$

3

Radiation detection and measurement

"In nature's infinite book of secrecy
A little I can read."

3.1 Electron spectroscopy

Electron spectroscopy is an analytical technique used to study the structure of atoms and nuclei. It encompasses the study of electrons emitted from atomic systems by a variety of different processes, such as electrons emitted from β decay, Auger electrons (electrons emitted from atomic shells to fill in a hole akin to X-ray photons), or, as in the case of SPEDE, conversion electrons.

3.1.1 Electron interaction

Electrons are directly ionising radiation. In general, when a charged particle enters a material, it will slow down and change direction due to electromagnetic interactions with atoms in the incident material. The reduction in velocity of a charged particle is given by the Bethe-Bloch formula [49], which is

$$-\frac{dE}{dx} = \left(\frac{ze^2}{c\beta\epsilon_0}\right)^2 N_A Z \rho 4\pi A \left(ln\frac{2m_e c^2\beta^2}{I\left(1-\beta^2\right)} - \beta^2 - \delta - \frac{C}{Z}\right) \qquad \text{(eq. 3.1)}$$

where z is the incoming particles charge in terms of e, e is the charge on an electron, c is the speed of light, $\beta = \frac{v}{c}$ is the speed of the incoming particle relative to the speed of light, ϵ_0 is the permeability in a vacuum, N_A is the Avogadro number, Z is the atomic number of the material, ρ is the density of the material, A is the molar mass of the material, m_e is the mass of an electron, I is the mean excitation potential, δ is a density correction term and C is the shell correction parameter.

However, due to the small mass of an electron, a key assumption for eq. 3.1 (that an incoming particle will not alter direction after interacting with the material) cannot hold. Additionally, when two electrons interact, the resulting wave function is inseparable. Bremsstrahlung ('braking') radiation must also be accounted for as the energy of the electron increases to around 1 MeV; this radiation is the result of photons emitted as a particle changes velocity as a result of an electromagnetic interaction with another particle, which must be emitted to conserve momentum. The cross-section for this Bremsstrahlung radiation [50] is given by

$$\sigma = \left(\frac{e^2}{mc^2}\right)^2 . \qquad \text{(eq. 3.2)}$$

In a detector, a bias voltage is applied, creating an electric field within the detector itself. When particles interact with matter, they cause electron-hole pairs to be created, with electrons removed from atomic orbitals by the ionising radiation. Electrons and holes then move to the positively-charged anode, which causes a current to flow with a voltage corresponding to the energy incident on the detector.

The current incident on an electrode from moving charges is given by the Shockley-Ramo theorem [51], which states that

$$i = q\vec{v} \cdot \vec{E_0}\left(\vec{r}\right) \qquad \text{(eq. 3.3)}$$

where $\vec{v}$ is the velocity of charge q, and $\vec{E_0}\left(\vec{r}\right)$ is the electric field at the position of the charge.

Assuming a particle that enters the detector does not leave the detector again (that is, escapes), the detector captures the full energy of the incident radiation. This can be worked out directly; knowing the ionisation potential of a material or gas (such as the band-gap between the valence band and conduction band in a semiconductor), and knowing the number of electron-hole pairs created by the incident radiation, it is possible to establish the initial energy of the particle.

3.1.2 δ-electrons

A major difficulty in performing electron spectroscopy is dealing with the δ-electron background. These are produced when heavy particles, such as the beam nuclei used in experimental studies, collide with electrons in the atoms of other nuclei, such as within a target, leading to a large low-energy background of scattered electrons. These electrons can then go on to collide with other electrons and produce further ionisation. However, the δ-electron distribution is not isotropic, and as can be seen as seen in Figure 3.1, is concentrated in the direction of the beam, as well as being generally a much lower energy than the conversion electrons of interest., The background can be significantly reduced by placing the detector in the backwards direction, upstream of the target. This technique is

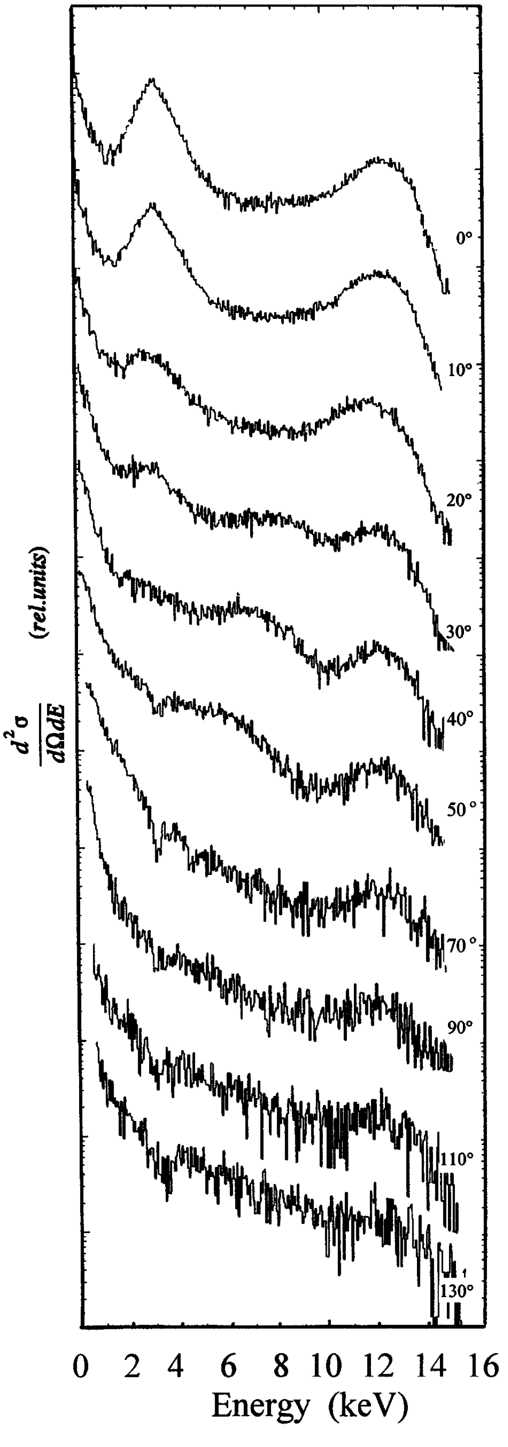

Figure 3.1: δ-electrons produced from a collision between $5.88MeV/u$ U^{29+} *on* C_3F_8 *[52]. The energy range is low, and drops quickly within the first 10 keV.*

used with SPEDE, meaning the setup is much simplified by avoiding the use of magnetic transport fields; these can severely decrease the efficiency of the detector and complicate the setup greatly.

3.2 γ-ray spectroscopy

γ-ray spectroscopy is a technique using an energy-sensitive detector for photons emitted from the nucleus, akin to electron spectroscopy. By collecting the radioactive emissions, a characteristic spectrum can be produced which can be used to infer properties of the radioactive nucleus or source under study [53].

All materials used for this spectroscopy are sensitive to photons, interacting via the photoelectric effect, Compton scattering, and pair production, as shown in Figure 3.2. The dominating process of interaction is energy-dependent.

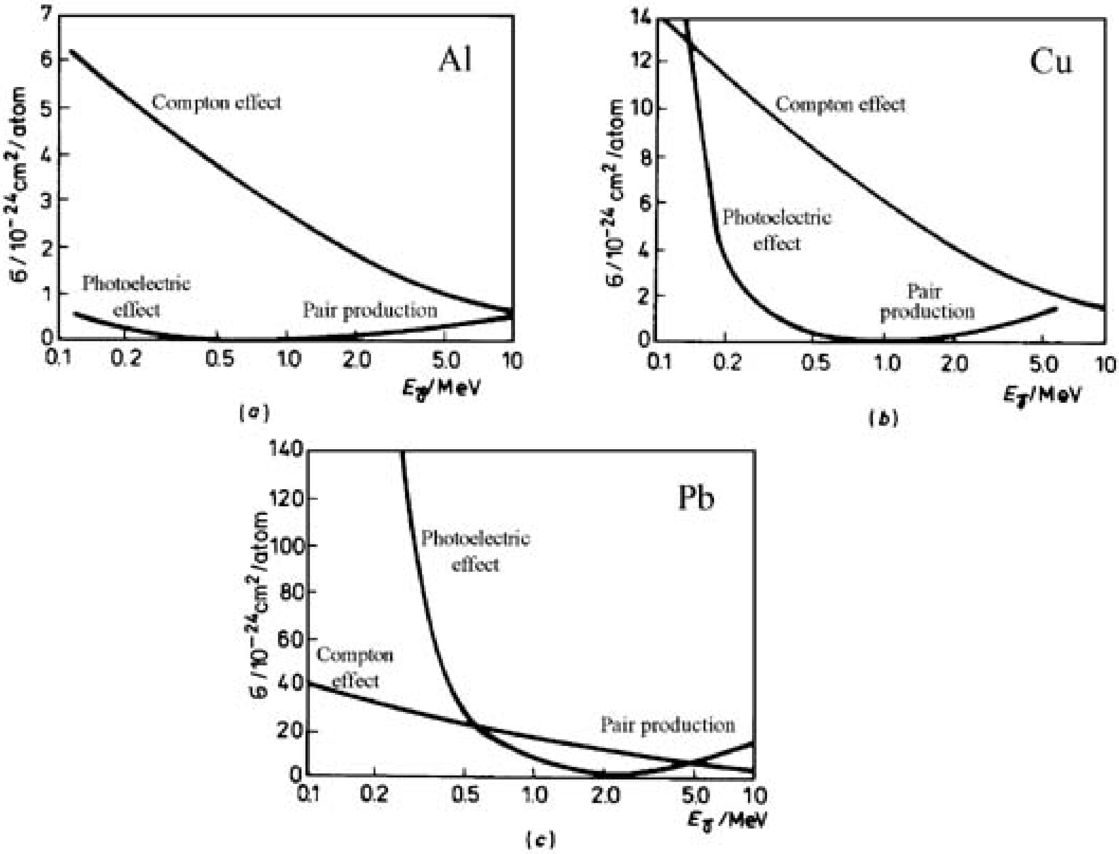

Figure 3.2: Photon interaction methods in aluminium (a), copper (b) and lead (c). Note the energy dependence of all effects, and the starting energy of pair production (1.022 MeV), as well as the Z dependence of the interactions, with the dominating interaction varying with element [54].

In the photoelectric process, all of the energy of the incident γ-ray is transferred to a bound electron of an atom in the detector. This electron is then ejected from the atom with a kinetic energy given by the Planck-Einstein relation

$$E = h\upsilon - \phi \tag{eq. 3.4}$$

where υ is the frequency of the incoming photon, and ϕ is the energy needed to remove the bound electron. This process mainly involves electrons closely bound to the nucleus in the K- and L-shells. If the energy of the incident photon is less than the work function ϕ of the K-shell then the photoelectric effect can not occur.

The second process that can occur is Compton scattering, where the incoming photon transfers only part of its energy to an electron, with the remaining energy carried by a new photon of lower energy in a scattered direction. The probability of a Compton interaction increases with the atomic number of the detector, however depending on geometry of the detector array not all the energy of the original γ-ray photon may be absorbed. Since the scattering is not constrained purely to the detector, and since any real detector must have a finite size, there is a probability photons can scatter out of the detector, taking with it any excess energy. This results in an effect on the spectrum called the Compton continuum. Another effect from Compton scattering is backscatter, which can cause γ-rays that did not originally enter the detector material, but rather the surrounding shielding and equipment, to enter the detector and also result in less than the full energy being absorbed [55].

The third effect seen in Figure 3.2 is pair-production. As a consequence of energy-mass equivalence, from the special theory of relativity, particles can be converted from an amount of energy, assuming all other conservation laws and symmetries are held. Therefore, photons with an energy greater than 1.022 MeV (twice the mass of an electron, 511 keV) can spontaneously create an electron-positron pair, which then travel in opposite directions with any excess energy from the photon shared equally between the pair as kinetic energy, in an effect seen also in high-energy transitions within nuclei. The positron then annihilates with electrons in the detector, causing two 511 keV photons to be emitted, again in opposite directions, which are subsequently detected, causing an annihilation peak at 511 keV in any resultant spectra [56].

3.3 Heavy-ion detection

Many nuclear physics experiments require particle identification. Identifying the particle is important for decrease background levels, kinematic correction, or radiation identification using techniques such as recoil decay tagging. Particles can be identified directly from energy and position, or by searching for subsequent β electrons, γ rays, or α particle (another heavy ion).

Heavy ion detection differ to the detection of particles already discussed in several ways. They will often have more energy, between 10^0 and 10^1 MeV for an α particle, or up to 10^3 for heavy nuclei from beam or target interactions. Their masses are several times that of an electron, and they are often in a highly charged state. These properties are both important in the stopping power defined in eq. 3.1. Most deposition of energy occurs at the end of a particle's trajectory; as a heavy particle slows down, it deposits an increasing amount of its energy, until coming to a stop. This differs to photons, neutrons, or electrons, which deposit most of their energy near the surface of a material. The effect is demonstrated for different ions in Figure 3.3, with the sharp increase and subsequent decrease in energy depositied for hydrogen and carbon ions known as the Bragg peak of the ion. Heavier ions shed some energy after the Bragg peak via a fragmentation of the particle; the effect of this is especially important when studying damage from ion beams.

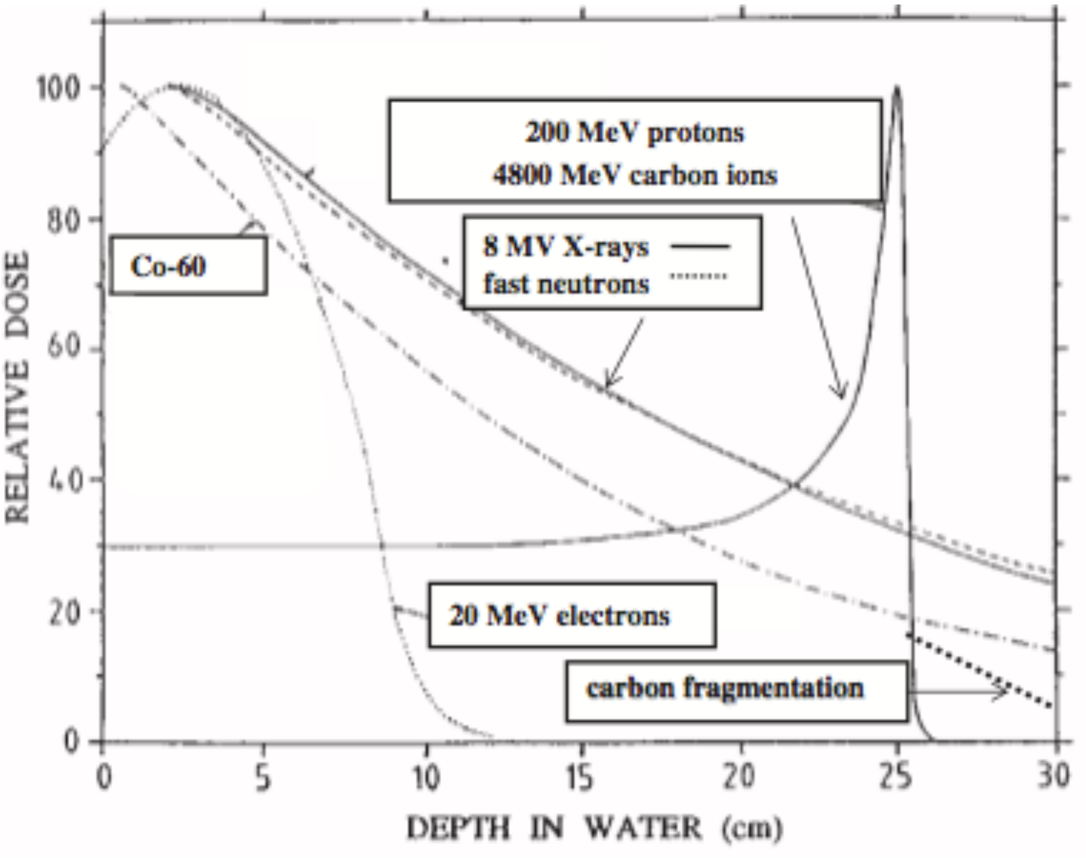

Figure 3.3: Energy deposition of particles in water as a dependence of depth. Relative dose, which is proportional to $-\frac{dE}{dx}$, varies with depth for different types of particles [57].

The requirements for any particle detector follow from the above properties. Clearly, a resolution on the order of 1 keV is not needed, since the energy magnitude is much larger, although good resolution is always desirable. Detector thickness is very important and dependent on what the detector will be used for, since most of the energy of the heavy ion is deposited at the end its path. The position is also integral to the experimental setup; with most ions from a beam focused in the forward direction, a particle detector placed at a backwards angle would see much fewer counts, whereas the distribution of α particles would be much more isotropic. For reasons common to much of spectroscopy, segmentation is desirable to be able to clarify position and increase count rate capabilities.

3.4 Doppler correction

SPEDE will be used with post-accelerated beams at HIE-ISOLDE, at energies of 4-5 MeV/u. For the heaviest beams, this could mean a total energy of around 1.1 GeV, approximately 10% of the speed of light for the nuclei in question. Therefore, any radiation from excited recoiling nuclei, either from the beam or target, will have an observed energy shifted in the laboratory frame compared to the actual radiation energy in the nuclear frame of reference. Classically, a wave which has been Doppler shifted will have its frequency f' altered by

$$f' = \frac{f_0}{1 + \frac{|\vec{v}|}{c}} \qquad \text{(eq. 3.5)}$$

where f' is the frequency of the observed wave, f_0 is the frequency of the wave in the source frame of reference, $\vec{v}$ is the velocity of the source away from the observer, and c is the velocity of the waves in the medium.

In the case of a photon, the velocity of the waves can be taken to be absolute, and therefore the speed of light c_0. The source is either a beam or target nucleus, scattering at different angles . Using eq. 3.4, and changing the reference frame to that of the motion of the source, this can be rewritten as

$$E_0 = \frac{E'}{1 - \beta \cos\theta} \qquad \text{(eq. 3.6)}$$

where E' is the energy of the observed radiation at the detector, E_0 is the energy of the radiation emitted in the nuclear frame of reference, $\beta = \frac{v}{c_0} = \sqrt{\frac{2E_p}{m_p {c_0}^2}}$ is the speed of the projectile relative to the speed of light c_0 (and E_p, m_p are the energy and rest-mass of the detected particle, respectively), and θ is the angle of the emitted radiation relative to that of the emitting particle; at 0 radians, the source is travelling towards the observer, hence the change in sign when compared to eq. 3.5.

Due to relativistic effects at the high speeds of the nuclei, the time period of the massless de Broglie waves will be retarded by the Lorentz factor

$$\gamma = \frac{1}{\sqrt{1 - \frac{v^2}{c^2}}}, \qquad \text{(eq. 3.7)}$$

and since frequency is the reciprocal of (and therefore energy is inversely proportional to) the time period, the equation for the massless Doppler shift is given by

$$E_0 = \frac{E'}{\gamma\,(1 - \beta \cos\theta)}. \qquad \text{(eq. 3.8)}$$

However, since the electrons have mass, eq. 3.8 must be modified according to relativistic dynamics. Under the same treatment as for a photon, the Lorentz shift for the radiated electron is

$$E_0 = \gamma E' \left(1 + \frac{p'c}{E'}\beta\theta\right). \qquad \text{(eq. 3.9)}$$

It can be shown through a detailed treatment of the Lorentz transformation of the momentum four-vector that

$$E_0 = \gamma E' \left(1 - \beta\sqrt{1 + \frac{2m_e c^2}{E'}}\cos\theta\right) + m_e c^2 \left(\gamma - 1\right) \qquad \text{(eq. 3.10)}$$

where symbols are analogous to that seen for the Doppler shift for a photon, and m_e represents the electron mass. Further, $\cos\theta$ must be measured as a function of detector angles.

A z-axis can be defined as that which the 'perfect beam' travels on; that is, an infinitesimal beamspot travelling exactly through the centre of the system. The x- and y-axis then bisect this, x running vertically and y horizontally. In spherical coordinates, a variable ϑ can be defined corresponding to the angle, clockwise, in the detectors, φ corresponding to the angle between the hit and the beam axis, and r as magnitude. By rearranging eq. 3.11 (vector dot product)

$$\vec{A} \cdot \vec{B} = |\vec{A}||\vec{B}|\cos\theta, \qquad \text{(eq. 3.11)}$$

and using trigonometric identities, it is possible to relate $\cos\theta$ in terms of angles in the detector system by

$$\cos\theta = \sin\varphi_1 \sin\varphi_2 \cos\left(\vartheta_1 - \vartheta_2\right) + \cos\varphi_1 \cos\varphi_2 \qquad \text{(eq. 3.12)}$$

where the subscript 1 corresponds to the CD detector, and 2 corresponds to a detector segment in MINIBALL, JUROGAM, or SPEDE.

Therefore the fractional relativistic Doppler shift in terms of laboratory angles is given by

$$\frac{E_0}{E'} = \gamma \left(1 - \beta\sqrt{1 + \frac{2m_e c^2}{E'}}\left(\sin\varphi_1 \sin\varphi_2 \cos\left(\vartheta_1 - \vartheta_2\right) + \cos\varphi_1 \cos\varphi_2\right)\right) + m_e c^2 \left(\gamma - 1\right). \qquad \text{(eq. 3.13)}$$

Care should be taken since the particle and electron detectors are facing in an opposite direction to each other. If the ϑ angle is given clockwise around the detector, then the detector facing in a 'backwards' angle (that is, behind the target position) has segments in ϑ equal to $2\pi - \theta$. Thus, the $\cos\vartheta$ term in eq. 3.13 becomes $\cos\left(\vartheta_{PIN} + \vartheta_{SPEDE}\right)$ in terms of detector angles. Equally, φ for the detector should be taken from π in order to preserve the coordinate system.

Due to a variety of different recoiling energies, and a variety of angles of emission of the radiation, different amounts of Doppler shift occur. With no kinematic correction, this results in a peak that is Doppler broadened. In order to correct this, good position resolution is required. This then leads to a requirement for segmentation of a detector, not only to be able to increase possible count rate and reduce capacitance, but to be able to correct for the effect of Doppler shift as much as possible. The same is applicable to the recoiling particle itself; since the amount of Doppler shift is dependent on the energy of the particle the radiation is emitted from, it is critical to be able to measure the energy and angle of incidence of the particles of study. Uncertainties in the precise position of de-excitation, path taken through the target, uncertainties in angles due to strip or crystal width, and in the recoil velocities will all result in the fact that an experiment which requires Doppler correction will never get as good a resolution as that from a static source. These can be mitigated to a certain extent however by various methods such as using thin targets and small segments.

Other effects can contribute to diminish the resolution of a detector, other than that dealt with in this section, but these are minimal compared to the effect of studying nuclei with a high β. It is however important to note that there will always be some finite resolution due to the uncertainty principle contributing to a 'natural line-width'. Another broadening effect, from the nuclei themselves as opposed to the detector, includes the Boltzmann distribution of the velocities arising from the thermal motion of the particles under study. Resolution can also be affected by so-called pressure broadening. However, this is mostly applicable to much lower energy radiation, and arises typically in molecular spectroscopy, where the low energy of the states of study mean these factors are a larger component of the error from the resolution.

3.4.1 Kinematics

To be able to accurately determine the Doppler correction factor for emitted radiation from nuclei, the position and angle of the emitting nucleus must be determined, with more precise measurements of these values leading to a more accurate correction. Due to experimental configuration, it may not always be possible to detect the nucleus of interest, owing to for example the finite size of a particle detector not being able to detect nuclei scattered at certain angles, or because of dead-time in a detector.

In experiments where nuclei are excited via a Coulomb interaction, a correction can still be made if one of the particles is detected. For the trivial case where the particle corresponds to that of interest, θ and ϕ angles are those as detected. For the more complex case, where the corresponding beam or target nucleus is detected but the nucleus of interest is not, angles can be determined by using the laws of conservation of energy and of momentum. In the closed system of the interacting nuclei, energy is conserved, with the difference in the kinetic energy of the sum of the final velocities to the sum of the initial velocities equal to the energy of the emitted radiation. To conserve momentum in the centre of mass frame, the nuclei scatter with a difference of π in the centre-of-mass system, but in the lab system the scattering angle will be such that the forward direction of the momentum vector in the lab system is still preserved. This then reduces to a trigonometric problem to determine the angle of scattering for the undetected particle, as seen in Figure 3.4.

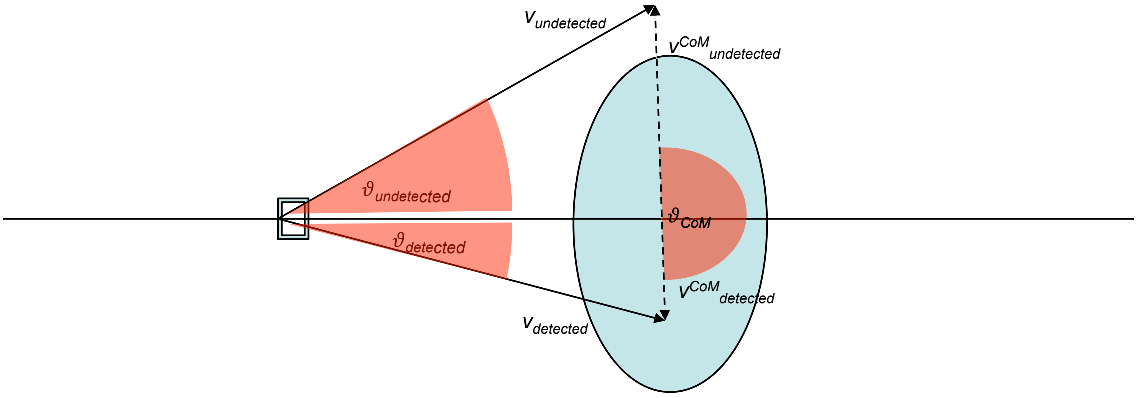

Figure 3.4: The detector may not always be able to detect both nuclei scattered during a collision. However, a solution can still be found via the use of trigonometric identities.

Using the above, it is apparent that by precisely determining the position of the scattered nuclei, and precisely knowing the value of the emitted radiation, recoil velocities of the scattered nuclei can be accurately determined generally to better precision than the resolution of the particle detector. The problem becomes more complicated in inverse kinematics, where the solution for the recoiling particles is two-valued, but by placing a gate on the energy of the nuclei, the solution becomes single-valued.

3.4.2 Mott scattering

In the case of two identical particles scattering, the scattering angles are modified by a quantum mechanical effect [58]. Under the operation of the interchange of particles $\hat{X}$ in the Hamiltonian, the symmetry of the wavefunctions must be taken into account, and the positions defined by $\hat{R}$ do not commute, resulting in a phase factor difference of $\kappa \in \mathbf{R}$, as described by

$$\left[\hat{R}, \hat{X}\right] = i\kappa. \qquad \text{(eq. 3.14)}$$

When the identical particles are fermions, the wavefunctions are symmetric, α is zero and there should be no change in the resulting wavefunction. In the case of bosons, where the wavefunctions are anti-symmetric, and a shift occurs when considering the resulting wavefunctions of the scattered particles. However, it remains impossible to determine which nucleus radiation is emitted from. Therefore, the resulting correction Doppler correction is only correct for half the particles; in half the cases, the scattered nucleus detected corresponds to the detected electron, whereas in the other half the scattered nucleus detected is not excited and the radiation quanta emerges from the undetected nucleus.

3.5 Detector types

There are three types of detectors in regular use, each with advantages for different types of applications.

The first, gas detectors, are most typically used for neutron detection and ion tracking, and are not particularly suited for the spectroscopic detail required, and thus will not be discussed in this thesis. For a detailed review see [59].

3.5.1 Scintillation detectors

The second is the scintillation type, which emit light when γ-rays interact with atoms in the crystal lattice. The intensity of the light is proportional to the energy deposited in the crystal. Scintillators are connected to photomultipliers in a light-tight environment, which converts the photons emitted by the detector into electrons and amplifies the signal. Sodium iodide (NaI) detectors can be produced in large crystals, meaning they have a high efficiency, but suffer from poor resolution, mostly due to the thermal motion of electrons varying the light output of the crystal, and lanthanum(III) bromide ($LaBr_3$) crystals are particularly suited for fast-timing applications [60].

3.5.2 Solid-state detectors

The third type of detector, a solid-state device, is semiconductor-based. The SPEDE spectrometer is a solid-state device made from silicon.

Interactions from incident radiation excite electrons from the valence band of the semiconductor to the conduction band, which respond to a bias voltage applied to the detector that creates an electric field, and moves electrons to the anode. The corresponding hole moves to the cathode. These electrons cause a current to flow which is then amplified and processed [61].

To process the pulses from the detecting semiconductor requires electronics to amplify and process the signal. A high-voltage power supply will be used to bias the detector where needed and supply necessary voltages to the rest of the system. Normally, the output signal from the detector will be passed through a preamplifier to increase the size of the signal, the output from this then subsequently sampled by digital electronics using an analogue-to-digital conversion (ADC) process to convert the analogue voltage information to a digital format that can be processed by a computer [62].

The majority of modern detector arrays typically use HPGe-type detectors for γ-rays, which have excellent resolution, but are not readily an option for any portable application, and silicon for the detection of directly ionising particles, such as electrons or α particles. To minimise thermal noise, detectors are typically cooled; silicon requiring much less coolant to deplete due to a smaller band gap, and being cooled to temperatures around 250 K. With germanium liquid nitrogen cooling is required in order to minimise the thermal noise resulting from the very small band gap of the material (0.74 eV at 0 K, compared to Si with 1.17 eV at the same temperature of absolute zero).

3.6 Historical review

The progress of electron spectrometers compared to γ-ray spectrometers has often been much slower. There are some similarities between the types, such as materials used or features such as high degrees of segmentation, and of course many differences due to the different interaction processes and energies. Spectrometer materials can be gas, liquid, or solid, and can vary from devices such as Geiger-Müller tubes, electron or photon multipliers, semiconductors, or Cherenkov detectors. Additionally, for electrons only, the detectors can be combined with electromagnetic fields for electrostatic- or magnetic-type devices.

3.6.1 γ-ray spectroscopy

The first detection materials used were Geiger-Müller tubes, gas-filled cavities where radiation causes electrons to be ionised which are then collected at an anode. These have been displaced in modern times eventually by solid-state detectors, where the charge produced by photon interactions is collected directly. A semiconductor, which has electrons and holes that can move freely, is used as the bulk volume, typically germanium, coupled with an electrode biased at a relatively high voltage to create a high electric field in the crystal, which is then passed to a preamplifier to increase the voltage pulse from this charge collection. These can be combined with other electronics, for example with Compton-suppression shields, to result in spectra with high peak-to-background ratios. Combining multiple detectors in turn led to the development of arrays currently at the forefront of γ-ray detection development, named GRETINA (Gamma Ray Energy Tracking In beam Nuclear Array, US collaboration) [63] and AGATA (Advanced GAmma Tracking Array, 12 country European collaboration) [64]. These are arrays of highly segmented Ge detectors that track γ-rays through the array, eliminating the need for shields, with excellent position resolution and efficiency, that ultimately will cover a full 4π geometry.

More on these arrays, including other arrays not mentioned here, can be found in [65], and illustrations can be seen in Figure 3.5. One array in particular, MINIBALL, has been a focus of this work. A brief summary is given in Table 3.1.

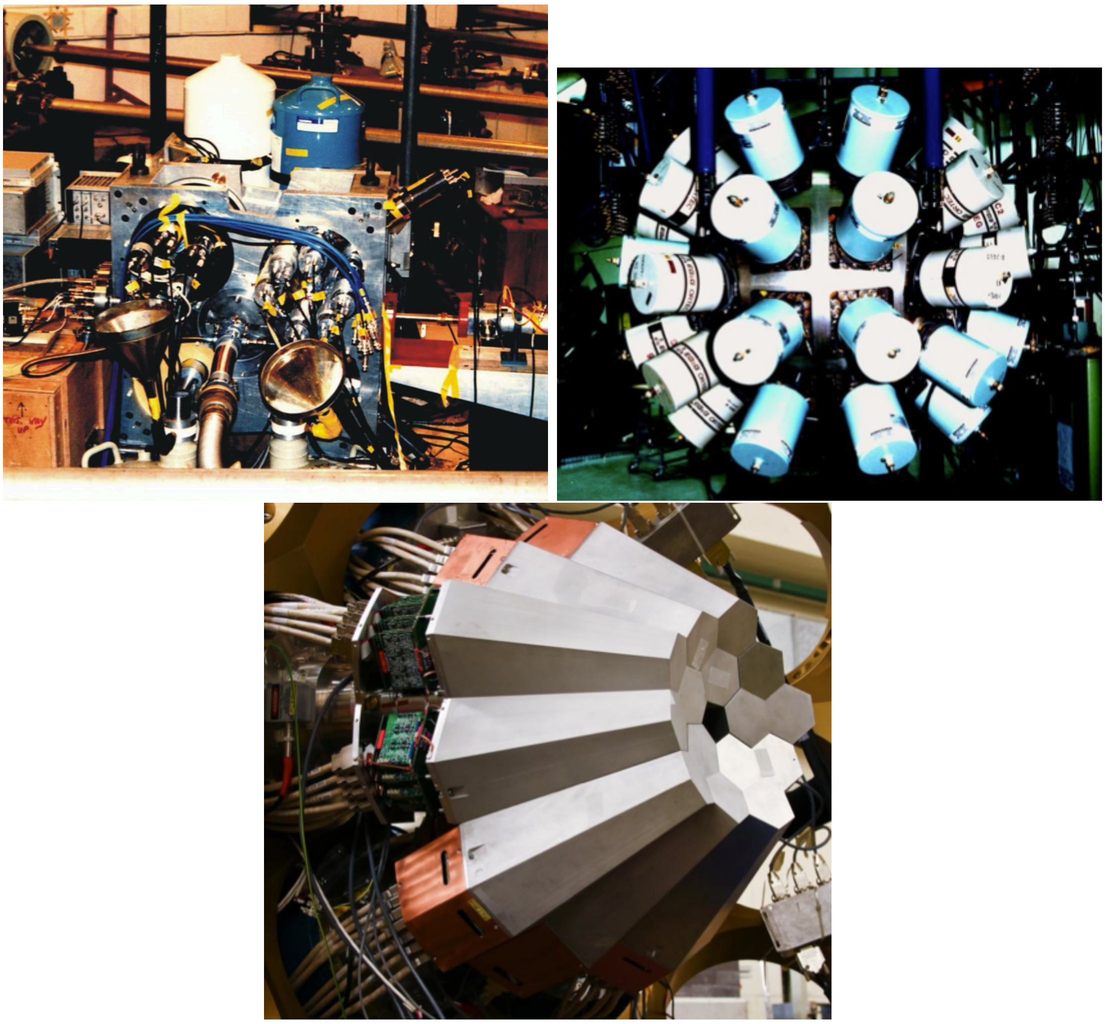

Figure 3.5: A variety of previous γ-detecting arrays are seen in the figure, clockwise from top-left: TESSA, EUROGAMII, AGATA. References are given in the text.

3.6.2 Electron spectroscopy

There are three main categories of in-beam electron spectrometers. These either use an arrangement of magnets transverse to the direction of electron travel to transport electrons around a barrier, a solenoid to transport electrons to the detector (with a longitudinal magnetic field), or use no magnetic fields to transport the electrons. This latter category is what SPEDE falls into, and is currently unique. Another in-beam spectrometer, SPICE (SPectrometer for Internal Conversion Electrons) is under development, but will incorporate a magnetic lens to increase the natural angular coverage of the detector. Some examples on different types follow.

Name	**Year**	**Location**	**Effective Segments**	**Resolution** @ 1 MeV *keV*	**Relative Efficiency** %
NaI(Tl)	1948	-	-	60	1 (for $3'' \times 3''$)
Ge(Li)	1964	-	-	~2	-
HPGe	1978	-	-	~2	-
TESSA	1980	Risø, Denmark	4	~2	25 (per detector)
TESSA3	1986	Daresbury, UK	16	~2	25 (per detector)
HERA	1987	Berkeley, USA	21	~2	25 (per detector)
EUROGAM	1992	Daresbury, UK	45	~2	65 (per detector)
GaSp	1992	Legnaro, Italy	40	~2	85 (per detector)
JUROGAMII	2008	Jyväskylä, Finland	39	2.1	60 (per clover detector)
MINIBALL	2007	CERN, Switzerland	40	2.3	53.9 (per detector)
AGATA	-	Europe	180	2.1	43.3 (total)

Table 3.1: A selection of γ-ray detecting setups, showing progress through the years

3.6.2.1 'Mini-orange'

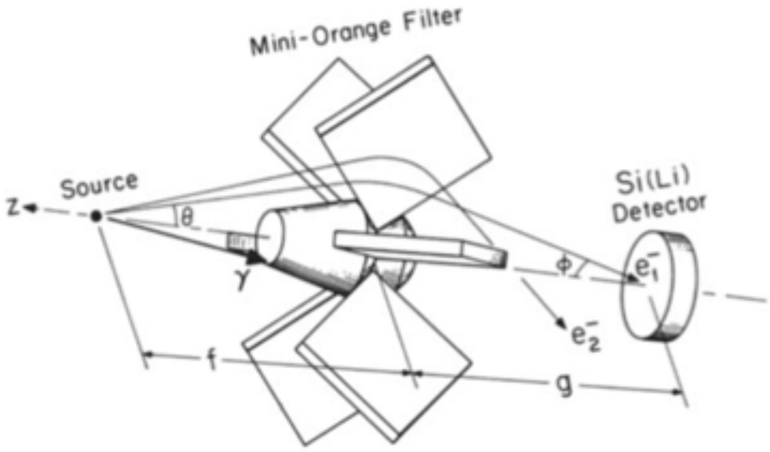

Figure 3.6: Typical layout of 'mini-orange' type detector [66]. The design was later combined into a multiple-element array called Pitt ICEBall (Pittsburgh Internal Conversion Electron Spectrometer Array) (akin to how TESSA was a combination of γ-ray detectors), and was placed inside an array of γ-ray detectors.

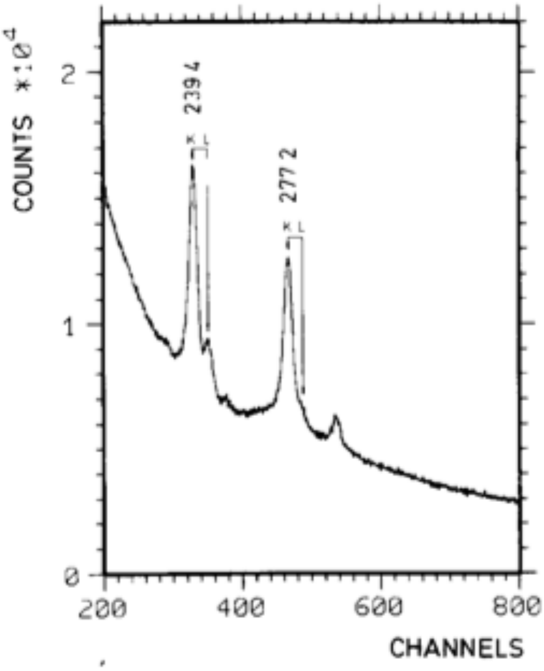

Figure 3.7: Electron spectrum from a mini-orange type detector [67]. The resolution in this uncalibrated spectrum is enough to make out electrons emitted from different shells.

Mini-orange detectors, so-called because of their size and geometry, are a combination of permanent magnets that enhances the detection efficiency of conversion electrons and suppresses background such as positrons and alpha particles, resulting in peak-to-background ratios by a factor of up to 80. It falls into the first category as introduced at the start of this section, and the layout can be seen in Figure 3.6. First developed by J. van Klinken in Germany [68], the method relies on the principle that a charged particle moving through a magnetic field experiences a different path depending on its charge and velocity, and advanced earlier toroidal electron spectrometers ('orange' detectors) by making use of small permanent magnets to make the size of the device more compact. Using a magnetic transport field to transport the electrons, and a shield such as lead to absorb direct radiation from the target, relatively clean spectra can be obtained. To select for different energies of emitted electrons, the position of the target, the strength of the magnetic field, or the position of the spectrometer must be altered in order for the radiation to reach the detector, which can increase beamtime requirements substantially. An example spectrum using such a detector setup is shown in Figure 3.7. Separation can be seen between K- and L-shell electrons on top of a smooth background.

3.6.2.2 SACRED

SACRED (Solenoid and Array for ConveRsion Electron Detection) as seen in Figure 3.8 was another type of spectrometer situated in Jyväskylä using a 25x25 mm square matrix of PIN (positive-intrinsic-negative) silicon consisting of 25 individual elements, each 5x5 mm,

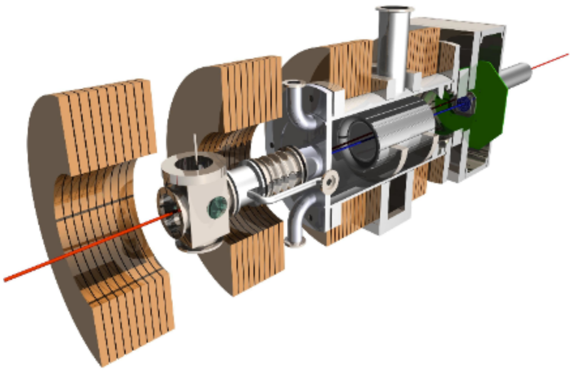

Figure 3.8: The SACRED detector [69].

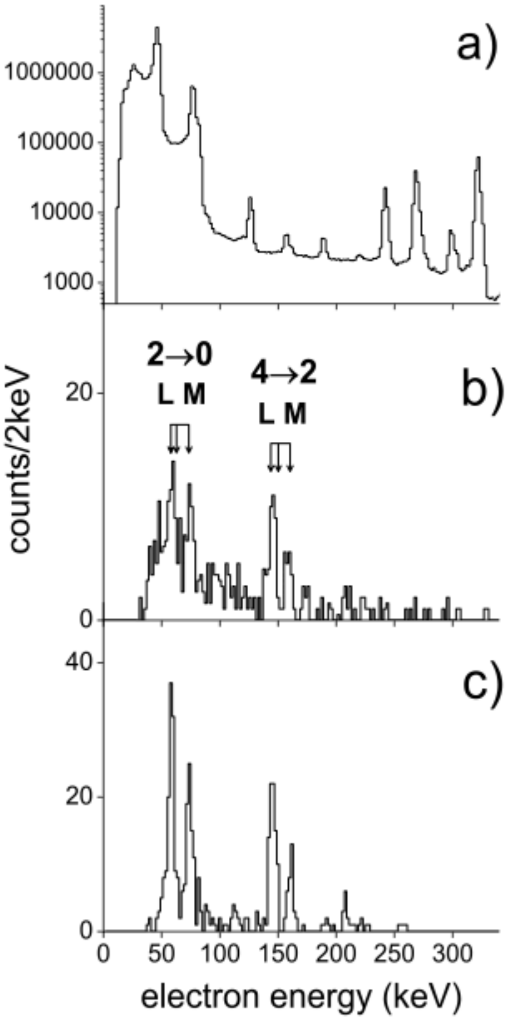

Figure 3.9: Electron spectra from SACRED [70]. Spectrum a) was obtained using a static ^{133}Ba source. Spectrum b) shows the conversion electron spectrum gated on the characteristic α decay of ^{226}U. Spectrum c) is the simulated equivalent to b).

where electrons are transported to the detector array by means of 3 superconducting coils creating a solenoidal field, combined with a high voltage electrostatic barrier to remove low energy delta electrons. As the name suggests, the magnetic field lies along the axis of electron travel. SACRED could also be combined with a germanium detector, to obtain γ-ray spectroscopic information at the same time as obtaining spectroscopic information from the electrons. Compared to the spectrum from a mini-orange device, Figure 3.9 shows peaks with a much better resolution. Primarily, SACRED allowed a precise kinematic correction to be applied to the electrons and obtain energies closer to the true value, with a resolution comparable to that seen from a static source.

Latterly, SACRED was combined with RITU (Recoil Ion Transport Unit) in order to do recoil-decay tagging [71]. This is a method of using the time-of-flight information for recoiling products of reactions that are magnetically separated, combined with a silicon strip detector for detecting the fragments, which can remove large amounts of background and result in much cleaner spectra.

3.6.2.3 SAGE

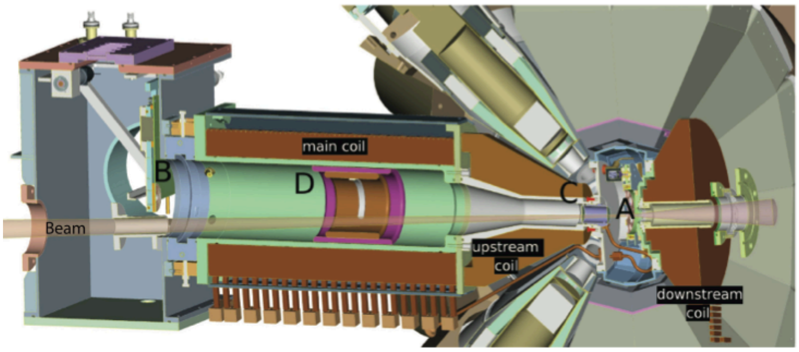

Figure 3.10: The SAGE detector [72].

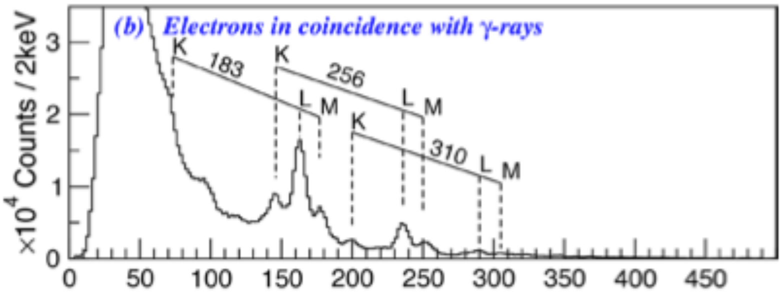

Figure 3.11: Gated electron spectrum from SAGE [73]. Here, electrons detected in coincidence with γ-rays are shown, resulting in a clean spectra where multiple transitions from different shells can be observed.

SAGE (Silicon And GErmanium) as seen in Figure 3.10 is a highly-segmented spectrometer with 90 channels that is coupled with the JUROGAMII γ-ray detector array in Jyväskylä, and builds on the experience with similar setups such as SACRED. Electrons are transported from the target position again with the use of a solenoid, and is placed in the backwards geometry with a HV (High Voltage)) barrier, in order to further reduce background, similar to SPEDE. SAGE is specifically designed to be used with the RITU separator for recoil-decay tagging experiments at JYFL, and employs the use of a carbon foil to separate the spectrometer from the helium-filled volume of RITU. It has proven successful in the study of superheavy elements, and at simultaneously examining electrons and γ-rays, as seen in Figure 3.11.

A major limitation of SAGE however is the effect on γ-detecting efficiency of the setup and the added complication of using a longitudinal magnetic field used to transport the electrons to the target; although the size is kept to a minimum by avoiding superconducting cells as in SACRED, it introduces difficulties in making the experimental setup more complicated. This magnetic field however is required, since the detector is positioned at a fixed angle relative to the target, the magnetic field increases the effective angular acceptance of the spectrometer. SAGE is also situated at an angle of 3.2° off the centre of the beam-axis in order to improve the detection efficiency. Work with SACRED showed Doppler broadening was minimised when there is a collinear geometry between the beam axis and the detector, as SPEDE is (although SPEDE will not employ a solenoidal magnetic field like the others).

These design choices are made with a particular view to the experiments that SAGE is especially designed for, namely high-multiplicity experiments and investigations into superheavy nuclei, and thus is not suitable the low beam intensities typically seen in radioactive beam facilities. The laboratory where SAGE is situated uses stable beams, limiting the nuclei where the strength of the B(E3) transition can be measured directly (although isotopes with relatively long half-lives, such as ^{226}Ra can be analysed directly from the ground state). SPEDE however will be situated at MINIBALL where very clean beams of a particular isotope of interest can be coupled with Coulomb excitation experiments to result in low-contaminant experiments exciting a much wider selection of beam nuclei from the ground state.

3.7 Beam production and transport

Many nuclear physics experiments use a charged particle beam, directed by magnets, impinging on a target. Different beam energies result in different processes dominating, such as fusion evaporation, Coulomb excitation, or deep inelastic scattering.

The main aims of beam delivery are several [74]. A beam delivery system should ensure that it is clean as possible; only isotopes of interest should be sent to the target and detector position. It should deliver beams of high intensity, to ensure that good statistics or rare events can be observed during the experiment. It should also be consistent; energy spread across the beam at the target position should be at a minimum, to minimise errors in experimental analysis, as well as to ensure the expected reactions occur.

Beams can be produced in a variety of ways. For stable, or very long-lived, nuclei, beams are often extracted from an ion source of that material, which can then be accelerated to a given energy. Radioactive beams, first produced in the 1950s [75], are produced as a result of secondary reactions (known as the Isotope Separation On Line (ISOL) technique), since their often short-lived nature means that having a source of the isotope is not possible. These can be produced using either thin or thick target reactions, with different setups suitable for particularly short-lived isotopes or production cross-sections. In production techniques using a thick target, the product must be able to diffuse out of the target at a reasonable time. A thorough review of ISOL production techniques is given in [76].

Beam particles, ionised either in their production or with lasers, have an overall charged, and so experience a force as per eq. 3.15

$$\vec{F} = q\left(\vec{E} + \vec{v} \times \vec{B}\right) \qquad \text{(eq. 3.15)}$$

where $\vec{E}$ and $\vec{B}$ represent the electric and magnetic field respectively. This means their path can then be manipulated with magnets. Typically, one or two dipole magnets are put in place to bend the beam and separate particles using a selection based on mass number A divided by the charge on the atom Q. Tuning the magnet strength means only a targeted $\frac{A}{Q}$ selection will be bent the required amount. A clean beam can then be accelerated to a given energy, in either a linear accelerator, cyclotron or synchrotron (which is essentially a linear accelerator in a loop), before being delivered to an experimental setup. Quadrupole or hexapole magnets are often used after this to focus the beam so that the resulting beam spot at the target position is small. Several additional steps may occur in addition to these steps, for example to increase the ionisation of the particles, to bunch them together, or to further separate them.

3.7.1 ISOLDE beam lines

Housed within the ISOLDE hall at CERN, Switzerland, is the HIE-ISOLDE (High Intensity and Energy at ISOLDE) linear accelerator, which is capable of producing radioactive beams with a final energy of 5.0 MeV/u. This is recently upgraded from the REX-ISOLDE (Radioactive beam EXperiment at ISOLDE) facility, which was capable of producing beams up to 3.1 MeV/u; the upgrade also increased the quality and intensity of the beams [77], and will eventually be upgraded to produce beams with energies up to 10.0 MeV/u.

A schematic of this HIE-ISOLDE beamline is shown in Figure 3.12. 1.2-2 μA DC proton beams from the proton synchrotron booster of energy 1.4 GeV are incident upon a thick target of metal, carbide or oxide, for example thorium oxide, which creates a variety of radioactive nuclides by fission, fragmentation or spallation. These beams are passed to one of two separators; either the General Purpose Separator (GPS), which allows three different simultaneous beams to be selected and sent to the experimental hall via one bending magnet, or the High Resolution Separator (HRS) which delivers one isotope at a time through two bending magnets. Beams from either separator can be sent into the HIE-ISOLDE beamline.

1^+ ions are bunched together in a Penning trap, REXTRAP, and cooled, with bunches then sent to REXEBIS, a charge breeder that strips electrons from the ions to give a mass-to-charge ratio below 4.5. Ions from REXEBIS are then sent through a mass analyser and on to the linear accelerator, which has a total length of approximately 10 m, consisting of 7 sections. The output from this device results in a pulsed beam which typically decreases in flux over the pulse time. Initially the ions are boosted in energy from 5 to 300 keV/u using a RFQ (Radio Frequency Quadrupole) accelerator, and re-bunched. The beam then passes through an interdigital H-type structure that boosts the energy to 1.2 MeV/u, followed by three seven-gap resonators. These resonators control the final energy of the beam. They are then followed by a 9-gap resonator, before the beam is sent to experiments at the end of the beamline. More detail on the ISOLDE facility is given in Kugler (2000) [78].

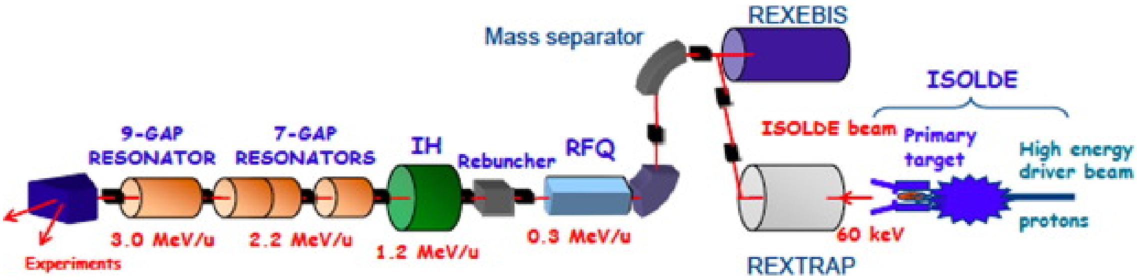

Figure 3.12: A schematic of the HIE-ISOLDE linear accelerator [79].

3.8 Electronics

Interactions of radiation with detectors results in a change in voltage, resistance, or capacitance in the device. For the energy of the radiation to be quantified, the detector is coupled with a pre-amplifier. These can be voltage-, current-, or charge-sensitive [80]. Current-sensitive are useful for large or fast rising signals with very low impedance devices. Voltage-sensitive simply amplifies any voltage at the input of the amplifying circuitry. However, they require the capacitance of the detector to remain constant, and since semiconductor intrinsic capacitance varies with temperature (altering theke current), they are not typically suitable for silicon or germanium devices. A charge-sensitive preamplifier allows the incoming charge to be integrated over a feedback capacitor placed in parallel to the amplifier. SPEDE uses the charge-sensitive Amptek 250NF preamplifier.

The output of the preamplifier can be passed to an acquisition system using analogue or digital electronics. By using digital electronics, the signal, which is digitized into a binary sequence immediately after the preamplifier, additional noise from analogue processing and shaping is minimised. Triggering can also be done offline, or changed quickly online, with digital electronics. Additionally, a large factor in maximising collected data for an experiment is to minimise dead time; this is much easier to avoid using digital electronics compared to traditional analogue systems [81].

SPEDE uses the Lyrtech digital electronic system used to acquire data have a MWD (Moving Window Deconvolution) to capture data from pulses. An ADC (Analogue-to-Digital converter) captures the analogue voltage signal and samples it, quantising the amplitude into a discrete signal which is then interpreted by the data reader. The software produces a trapezoid from the captured pulse, from which information of the pulse can be read. A series of parameters is input into the MIDAS control software in order to shape this trapezoid, in order that the captured data is an accurate representation of the energy deposited in the detector. A detailed treatment of this process is given in [82]

4 SPEDE

"It's the job that's never started as takes longest to finish."

4.1 Specifications

Three n-type silicon wafers, of diameter 47.6 mm, were ordered. Each is 500 μm thick, although there are plans to possibly order thicker variants (1000, 1500 μm) in the future. The detector is electronically segmented into 24 areas (average size 53.2 mm^2), with 3 rings of 8, arranged as can be seen in Figure 4.1. This geometry was chosen in 2012 from Geant4 simulations by J. Konki. Five options, shown in Figure 4.2, were tested, with various angular and radial segmentations. The final design had a FWHM of 9.2 keV after Doppler correction, compared to the best of 8.1 keV from option 5. The third option has larger segments and thus larger capacitance and leakage current, but this is negligible compared to the resolution being decreased from kinematic broadening. With 24 channels, as opposed to 36 or 48, the number of electronic channels needed is minimised, meaning that the overall size of the detector is kept as small as possible, and the effect on γ-ray efficiency is as negligible as possible. Guard rings, designed to minimise leakage current at the edge of the depletion zone in the detector [83], take up 3 mm of the inner and outer circumference of the detector.

The dead-layer of the detector is 0.5 μm, or 0.1% of the thickness. The expected penetration depth of δ electrons of 1 keV directly incident on the silicon, as calculated by ESTAR [85], would be approximately 57 μm, which is about 100 times the dead layer thickness of the silicon. It should be noted however that anything that would stop in the dead layer does not necessarily imply none of the interaction is seen. An example of this typical elementary model of the dead layer resulting in no charge collection being incorrect is demonstrated by Wall *et al.* [86] for the KATRIN neutrino-mass experiment. A plot of the stopping power of electrons in silicon, generated using ESTAR, is seen in Figure 4.3. The thickness of SPEDE means that electrons with an energy of up to approximately 600 keV can be detected. This figure cannot be determined exactly as it depends on the distance from target to detector and the angle that an electron strikes the detector at, as

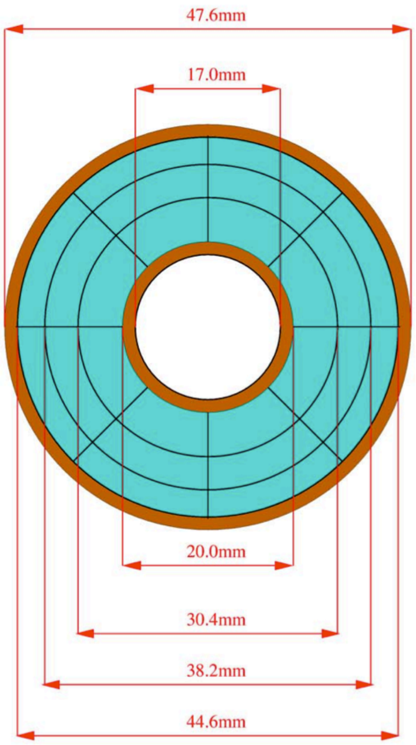

Figure 4.1: Inner and outer diameters of SPEDE are shown above. Detector segments are shown as blue areas between black lines, with guard rings illustrated by brown colouring.

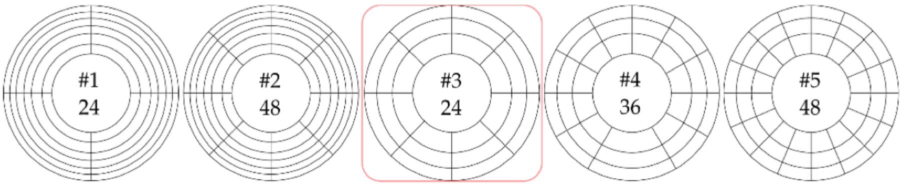

Figure 4.2: 5 designs for SPEDE are shown [84].

the apparent thickness will generally be larger than 500 μm.

The detector sits on a printed circuit board (PCB) with a diameter of 120 mm with all signal processing taking place on-board using Amptek 250NF preamplifiers. This board then clips into a copper cooling block with fins on ensuring good thermal contact between the heat-producing preamplifiers and the copper, as well as ensuring thermal noise in the silicon is kept to a minimum, with the setup being cooled to -20°C.

In place in the chamber, the detector sits in the backwards angle. That is, the beam passes through the centre of the detector before interacting with the target, thus minimising the direct exposure to delta electrons. In order to further suppress the delta electron flux incident on SPEDE, the target ladder is also biased with a positive voltage in order to attract the low-energy electrons back towards the ladder. Additionally, to suppress the effect of UV light and further reduce the low-energy electron background, an aluminised

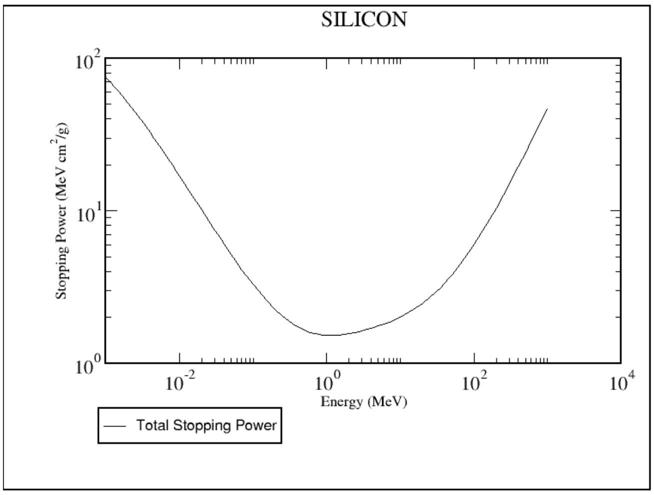

Figure 4.3: Stopping power of electrons in silicon, generated using the ESTAR program.

Mylar foil is placed directly in front of the silicon, on a tri-star rig. A cross-section of this simulated setup, without the foil, can be seen in Figure 4.4.

4.2 MINIBALL array

SPEDE will be coupled with the MINIBALL array at the ISOLDE (Isotope Separator On Line Detector) facility located at CERN near Geneva on the Franco-Swiss border.

MINIBALL is situated at the end of this beamline, and is shown in Figure 4.5. MINIBALL consists of 8 cluster detectors each consisting of 3 individually encapsulated 6-fold segmented HPGe detectors, giving a total of 144 segments, covering 65% solid angle. This granularity is important in order to reduce the Doppler-broadening of γ-rays emitted by nuclei, which are travelling at speeds of up to 0.1 c. Full-energy peak efficiency is given as 20% for $E_\gamma = 1.3$ MeV, and 5% for $E_\gamma = 11.7$ MeV. Geant4 simulations show a resolution of about 7 keV at a γ-ray energy of 1.3 MeV at 0.045 c for an observation angle of $90°$ with respect to the direction of the velocity vector of the emitting nucleus.

The target chamber consists of a thin target foil made of isotropically pure material, which the beam is aimed at, resulting in the (separate) Coulomb excitation of nuclei in both the target and beam. Particles are detected by a double-sided silicon strip detector (DSSSD), called the CD-detector. Data from this is used to determine if γ-rays detected by the MINIBALL array are prompt or random, and whether they are emitted from the beam nuclei or the target; since Coulomb excitation has well defined scattering angles, there is a maximum scattering angle for the projectile, which can be used to separate the nuclei.

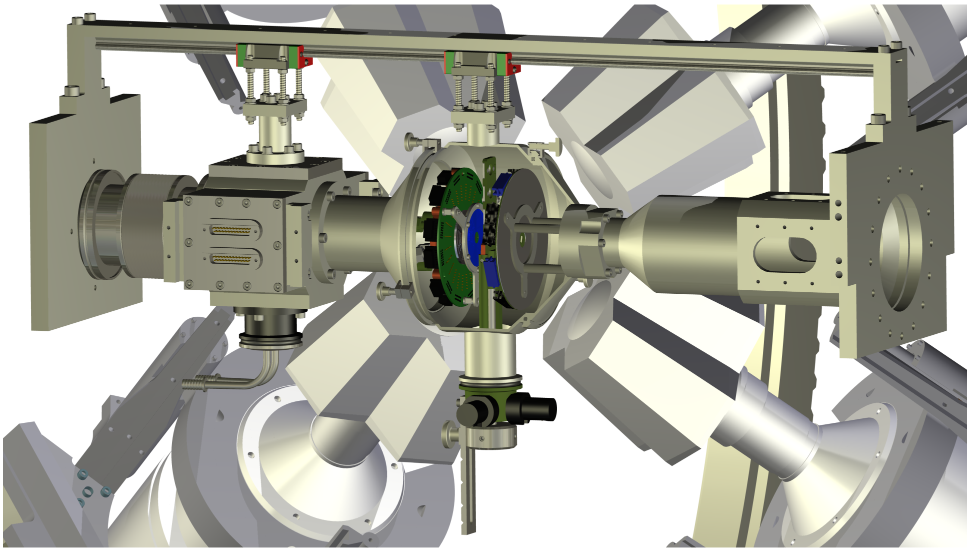

Figure 4.4: A computer-aided design (CAD) drawing of SPEDE is seen on the left of the picture. The beam enters from the left side, through the centre of the detector, interacting with the target in the position selected by the adjustable target ladder. Decays from excited nuclei are subsequently detected by SPEDE and the surrounding MINIBALL detectors. Particles are detected in the CD detector on the right.

4.3 Simultaneous electron-gamma spectroscopy

As outlined in the introduction of this thesis, combining electron- and γ-spectroscopy is a powerful tool of nuclear spectroscopy, but is fraught with challenges. The detectors outlined above have all been combined with other detector facilities to enhance the information available from any experiments, but have failed to maximise the potential for both full electron and γ-ray spectroscopic information, with the exception of SAGE which was built expressly to be combined with JUROGAMII.

There are several challenges to performing electron spectroscopy coupled with gamma-ray spectroscopy. Perhaps the largest, in any spectroscopic study, is a high level of background counts drowning out any real signals. This can be because of two reasons; number one being low-energy pile-up in the detector or the electronics smothering any real signal, or number two because of a broad range of electron energies being detected with high count rates. Secondly, there is a problem with balancing the efficiency of each type of spectroscopy. It is important to ensure any electron spectrometer included with an existing γ-ray array attempts to minimise any loss of efficiency of this array, whilst maximising the efficiency of the electron spectrometer. This can lead to a problem with, for example, mini-orange type spectrometers, which are large and contain a lot of excess material beyond the detector component. Thirdly, there is the issue of Doppler broadening. Since nuclei especially suited for simultaneous spectroscopy will typically be moving at speeds up to 0.2 c it is very important that the position of source emission can be determined precisely [87].

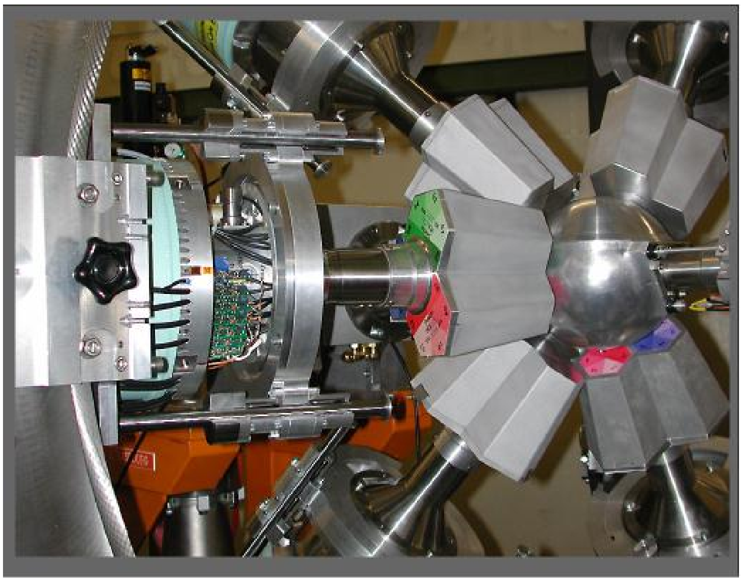

Figure 4.5: The MINIBALL array of HPGe detectors, in place at the end of REX-ISOLDE.

There are several methods to minimise these problems however, by the choice of electronics used, the geometry of the detector and positioning, and increasing the granularity of the device.

4.4 Electronic tests

The first tests of electronics took place in March 2013, at the University of Jyväskylä, and used a simple setup of an Amptek test board in conjunction with a PIN (positive-intrinsic-negative) diode to determine whether the 250NF amplifiers could be used in order to drive a 50 Ω output directly into a Lyrtech digital electronic system. The test board had the same layout as an individual SPEDE channel, and is described in Figure 4.6. The setup was placed inside a small aluminium enclosed vacuum chamber shown in Figure 4.6, in order to provide a dark, low pressure environment for the electronics and PIN diode to be situated, to minimise unwanted noise. Two open ^{133}Ba sources were used. Initially, source JYFL-66 (strength 16.2 kBq) was used, before being replaced by the stronger JYFL-90 (284.7 kBq), which were attached to the ceiling of the chamber using a bespoke aluminium hanger.

A PB-5 pulse generator by Berkeley Nucleonics Corp was used to generate a 1 kHz square wave, with a rise time of 50 ns, fall time of 500 ns, delay of 250 ns, width of 100 μs, and amplitude 40 mV. This waveform, plus the output after passing through the Amptek preamplifier, can be seen in Figure 4.7.

It was noted that although the tests were successful and proved a direct Lyrtech connection was possible, results were better with a GO (Gain-Offset) box, however the

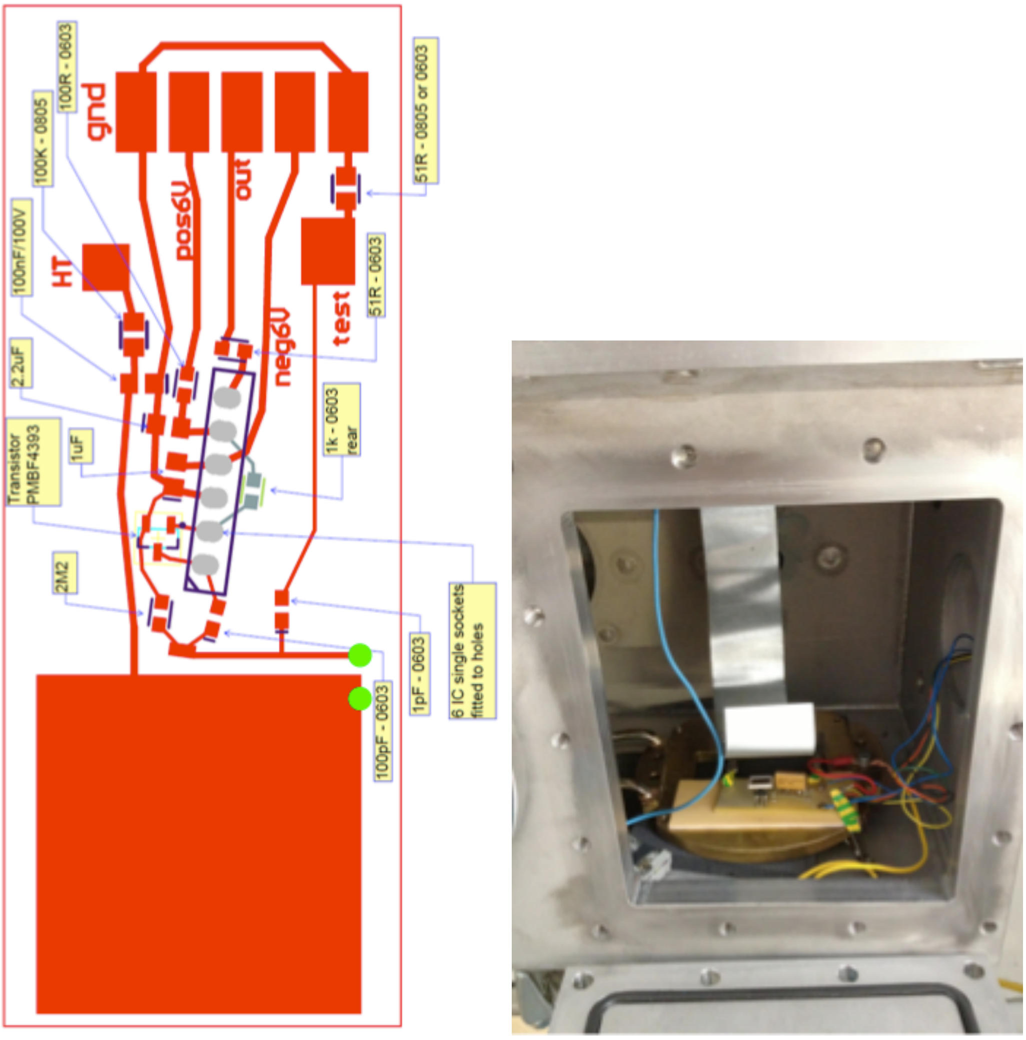

Figure 4.6: The figure on the left shows the PCB layout for an individual SPEDE channel, with the large pad on the left indicating the detector and the top line the bias connection. The bottom circuit, labelled test, was only present during preamplifier tests in March 2013. The testing chamber is seen on the right.

resulting pulses do not remain sharp, with a smooth transition between the rise and decay time, as opposed to the sharp well defined edge of a peak one would expect. This effect is due to the time constant used in the GO boxes effectively smearing the signal such that it becomes rounded, illustrated in Figure 4.8. Data from the ^{133}Ba source was collected, and is shown in Figure 4.9.

Initial electronics tests with the SPEDE PCB were carried out in the Oliver Lodge laboratory at the University of Liverpool, UK, during Autumn 2013. A large steel vacuum chamber, shown in the centre of Figure 4.10, was used in order to provide a dark, low pressure environment for the electronics and detector silicon to be situated in during the first tests. Thermal foam was used to attach a cooling block inside the chamber to the copper cooling block on the SPEDE PCB, in order to help facilitate heat transfer from the

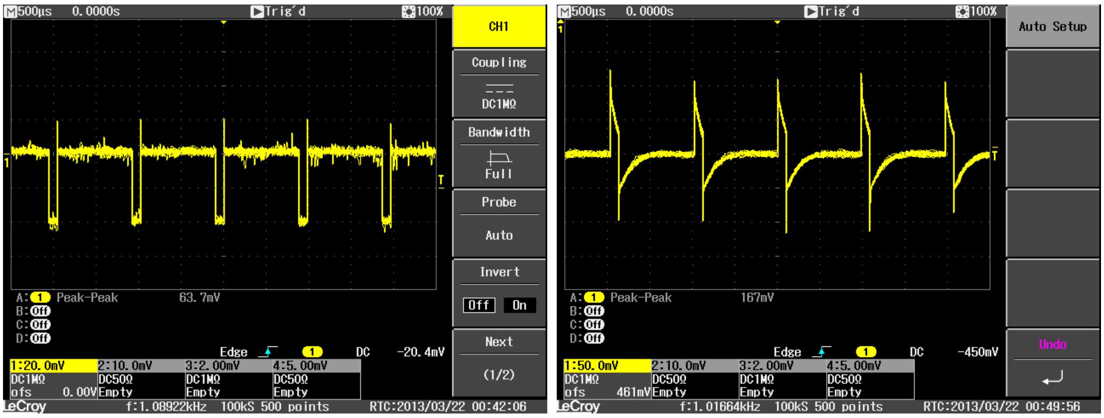

Figure 4.7: The input pulse is shown on the left, and the output on the right. The output has a rise time of about 100 ns, and returns to the baseline after about 350 ns.

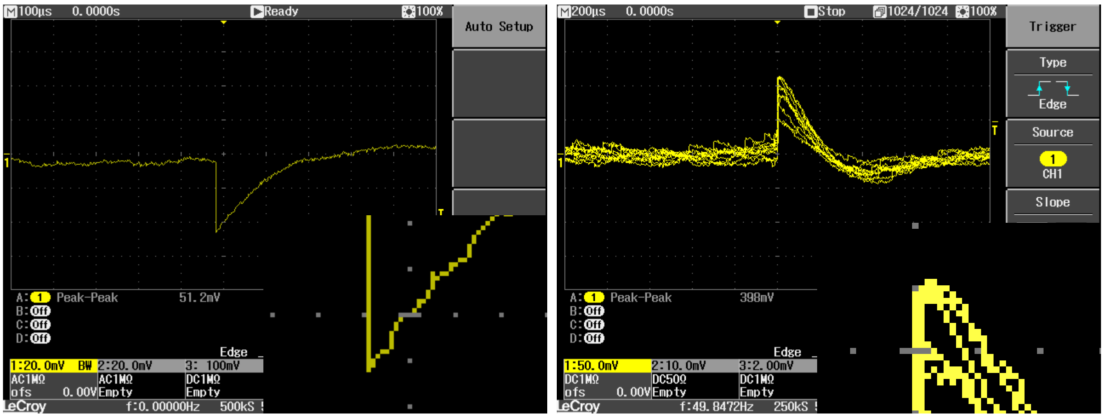

Figure 4.8: The pulse directly from the preamplifier is shown on the left, and from the GO box on the right, with each pulse zoomed in on the lower right of the picture. The top of the pulse from the GO box is elongated and appears flat before decaying, although the effect is slight and not an issue for pulse detection using Lyrtech electronics, which uses the initial sharp rise of the pulse for information. The two images are not directly comparable in terms of amplitude as the GO box has a gain of -2.5, and the time division for the scope has also been doubled to view pulses from the GO box.

detector itself, with an active refrigerator circulating ethanol at approximately -20 °C. An open ^{133}Ba source, of strength 72 kBq, was again attached to a bent piece of aluminium for the same purpose as the initial preamplifier tests, approximately 30 mm above the detector.

Due to the final SPEDE chamber not having been produced, and its dimensions not decided upon, only two ribbon cables were available to provide power to the preamplifiers, and to get the signals out. Thus, four channels were tested at a time using several Amptek 250NF amplifiers, each of which was also tested. Two of these proved to be faulty, and another failed during testing due to a faulty resistor. A 15-pin D-type connector was used to provide the power and signals to and from the PCB using boards identical to the ones used in the final design. Data acquisition was done using two Ortec Aspec 927 dual-

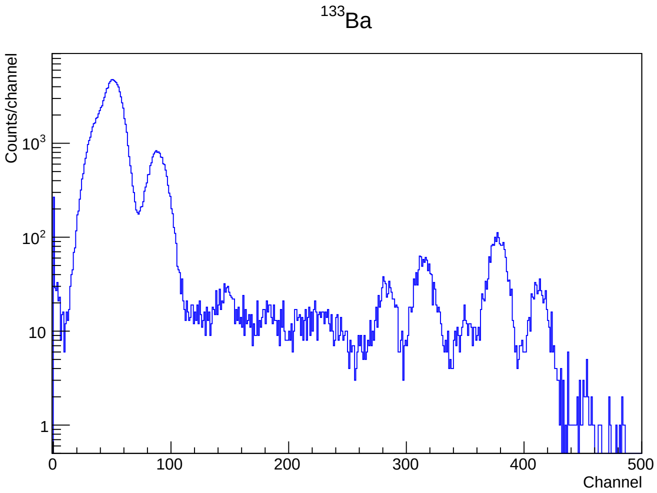

Figure 4.9: ^{133}Ba spectrum from preamplifier test, March 2013. This is uncalibrated; the 320 keV peak corresponding to the strongest transition at channel 377.5(2) has a FWHM of 13.9(4), which using a single point calibration would correspond to a FWHM of 11.9 keV.

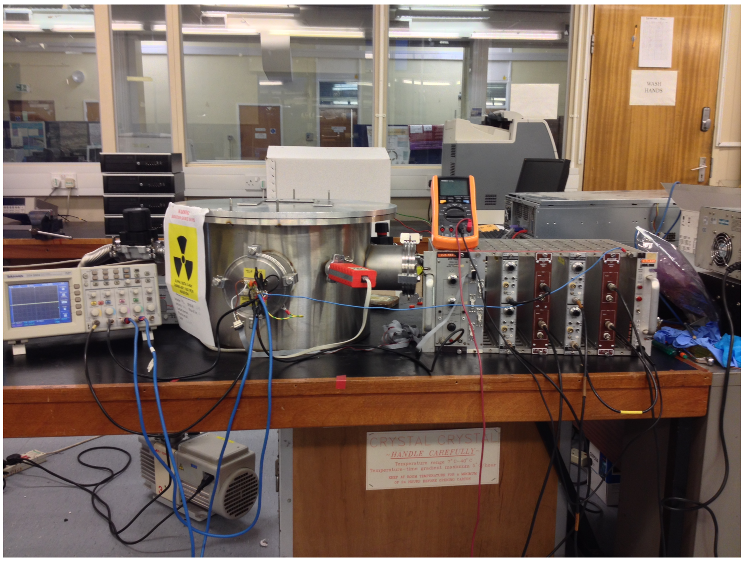

Figure 4.10: The setup used for initial testing of SPEDE in the Oliver Lodge laboratory, Liverpool

channel analysers, passing through an Ortec 671 amplifier, recording data to the maestro data acquisition software suite. An energy spectrum of channel 1 from SPEDE is shown in Figure 4.11.

Several problems were identified on the PCB itself, but no issues were seen with the detector silicon. As expected, The application of a bias voltage decreased the leakage current, shown in Figure 4.12, resulting in a slight reduction of peak-to-peak noise on the baseline.

Several frequencies were identified on the oscilloscope using a fast Fourier transform,

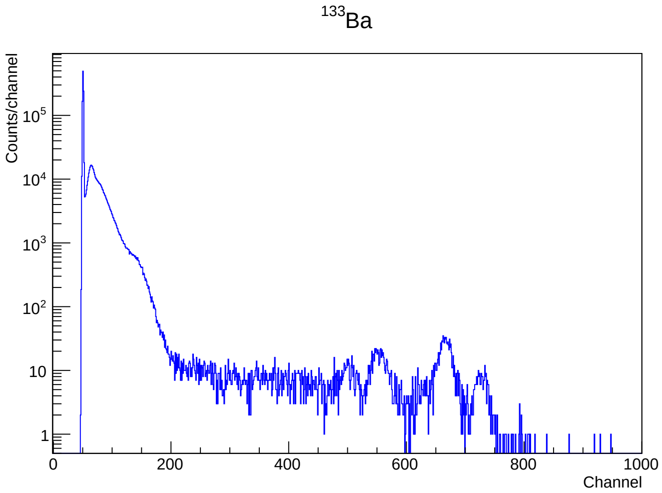

Figure 4.11: ^{133}*Ba spectrum from SPEDE channel 1, during initial electronics testing, November 2013. This is uncalibrated; the peak corresponding to 320 keV at channel 665.7(5) has a FWHM of 22.6(1.0), which using a single point calibration would correspond to a FWHM of 10.9 keV.*

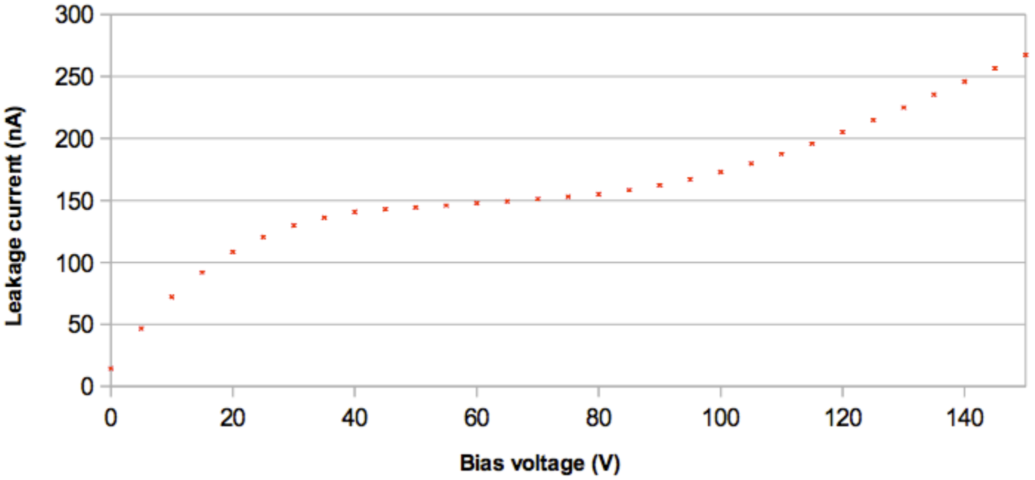

Figure 4.12: Plot of voltage against current, illustrating the saturation voltage of the SPEDE detector at room temperature in a vacuum, with the flat area at approximately 50 V.

which were investigated using the OFCOM (UK regulatory body for communications) website [88], and were possibly identified as seen in Table 4.1.

Upon the completion of the final SPEDE chamber, final electronic tests were done with a dedicated Lyrtech system in situ, with all channels connected to the digital electronics. This resulted in a drop in the baseline peak-to-peak noise of about 2 mV when compared to the system only having 1 channel connected, most likely because each channel was fully grounded and could not introduce stray charge into the system.

The final electronics setup tested was subsequently used for in-beam tests and com-

Frequency *MHz*	**Possible source**
0.05	Unknown
2.4	Railway/shipping radio
7.75	Railway/shipping radio
50-62.5	University of Liverpool security
115	Aviation
2000	Mobile phone networks
6000	Point-to-point fixed links

Table 4.1: Frequency components in noise in the Oliver Lodge laboratory

missioning. It consisted of an Ortec 428 bias supply, as used in testing in Liverpool, an unnamed power supply for preamplifiers, Lyrtech VHS-200 system for recording data, and a bespoke GO box with a gain of -1 designed at the University of Liverpool, used to ensure the signal from the detector was able to traverse the long cabling in the experimental hall to the data acquisition (DAQ) systems.

4.5 Mechanical tests

The SPEDE chamber was produced at the University of Jyväskylä engineering workshop and was designed by Kimo Kohtiolevy. The design is partly based upon the T-REX chamber [89] that was previously used in conjunction with the MINIBALL array, as opposed to the typical spherical MINIBALL chamber which allows for optimum position of the γ-ray detectors but only has room for one PCB. In order to minimise any impact on the efficiency of MINIBALL, the chamber was designed with two wide-angled cones joining onto a short cylinder, necessary to facilitate the insertion and removal of the target ladder and high-voltage circuitry.

The SPEDE PCB is mounted on a brass cylinder inside the aluminium chamber which allows the device to move respective to the target position. This also helps separate the signal and cooling cabling from the actual beam pipe, and serves the purpose well. Initially, PT100 thermistors were mounted along this beam pipe and on the back of the SPEDE PCB but seemed to contribute majorly to electronic noise in SPEDE, and so were removed, leaving only the PT100 on SPEDE PCB itself.

From the bottom, a 6 mm diameter tube passes which circulates an ethanol cooling liquid. Electronics cables pass through two feedthrough boxes on either side of the chamber. Particle detection electronics pass out the other side of the chamber, fitting to the pre-existing MINIBALL feedthrough chamber segment. However, this was not used for in-beam tests in Jyväskylä due to the size of this segment not fitting between the SPEDE chamber and the RITU separator device.

It was initially noted that there were several issues with the fitting together of the 3 main separate segments, which were principally an issue with O-ring diameter and thickness. Subsequently, the main point of failure for system was in the signal connector feedthroughs, which were redesigned resulting in a less fragile fitting with a more secure weld. The most fragile point of the chamber is the support for the target ladder. This has an internal weld between a short-length tube with a large diameter and a hole cut out in the cylindrical middle segment of the chamber. It appears there may be microscopic cracks in this weld which result in the chamber not being completely airtight, a hypothesis confirmed by the increase in measured amounts of helium entering the chamber when a helium stream is introduced to this area. However, whilst the system is being pumped it has a pressure of around 10^{-5} Pa, satisfactory for the experimental conditions required.

Beyond the chamber itself the target ladder is also an integral part of the spectrometer. It operates by hand, with a piston that is moved up or down and fixes into place with a notch, in four positions. Running through this mechanism is a wire which applies a positive 5 kV potential difference to the target position, affixed by a spring clip. The ladder was changed for the second part of commissioning in Finland in order to ensure a better alignment.

Dimensions and drawings of the SPEDE chamber are given in Figure 4.13.

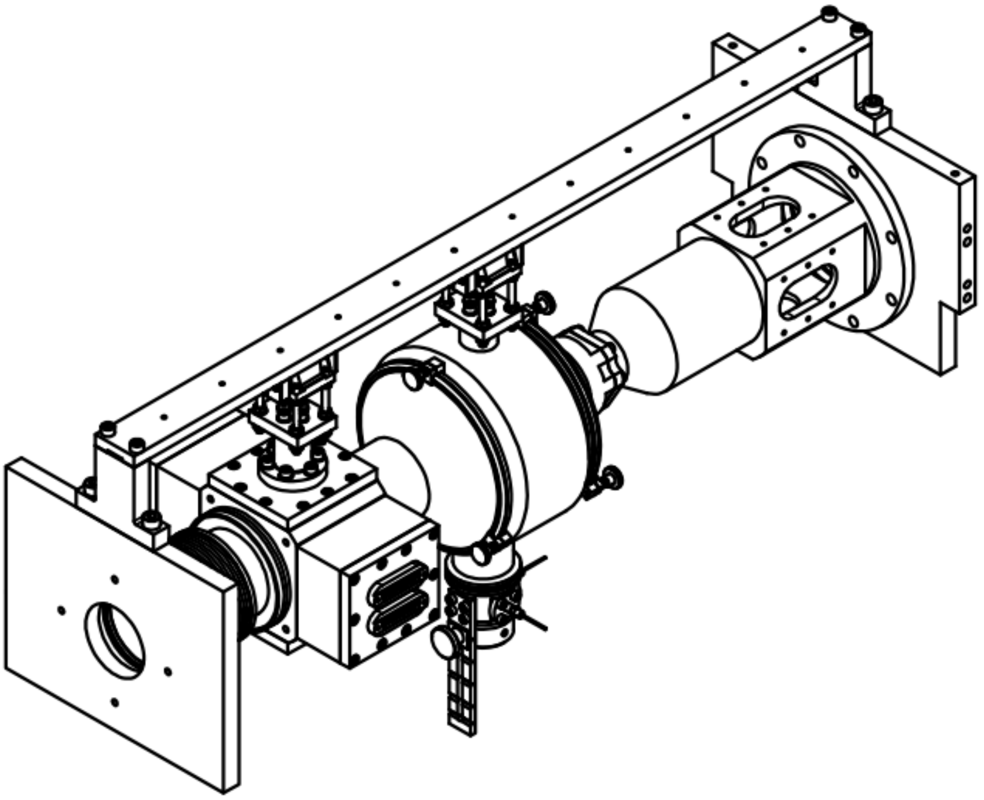

Figure 4.13: An overview of the full SPEDE chamber presented from the original mechanical drawings. Access to SPEDE is by removing the bellows, and the chamber sliding freely on the guide rail.

4.6 In-beam tests

In-beam testing took place in the 'γ-RITU' area of JYFL laboratory, situated on the Ylistönrinne campus at the University of Jyväskylä, as mentioned previously. The laboratory has a K-130 cyclotron, details of which are presented in Table 4.2, used to provide beams of up to 130 MeV to a variety of experimental setups. Rather than being coupled with the MINIBALL array, tests were performed coupled with detectors from the JUROGAMII detector array (although the full array was never used), and a series of expedient PIN diode arrays in place of the CD detector used in conjunction with the MINIBALL setup.

4.6.1 In-beam electronic setup

Data was recorded using the Total Data Readout (TDR) DAQ system developed by the GREAT collaboration with analysis done using the GRAIN software package. GRAIN is a Java analysis framework developed by Panu Rahkila for the TDR system. This software is used to sort through the data in order to make sense of the time-stamped raw energy events recorded by the detectors. A full description of the TDR system and GRAIN can be found in [91], with a schematic shown in Figure 4.14 (taken from the same publication).

The TDR system is a triggerless DAQ system where each channel operates individually, with each event timestamped using a 100 MHz clock signal. This has an advantage over traditional setups that use a hardware trigger to store data. By storing all events and the time they occur, triggers can be set via software, ensuring maximum efficiency from the data processing setup for studying nuclei and their decays.

Due to the way GRAIN is structured, it is very simple to create new sort code for each experiment. However, it is not possible to define a new detector system, which SPEDE is. A user creates sort code by extending the GRAIN sorter. This sorter initially sorts each event into event arrays separately for each type of detector array at Jyväskylä, for example GREAT or JUROGAM clover detectors. SAGE, an existing electron spectrometer at the University of Jyväskylä, is also one of these existing detector arrays included with GRAIN, and so therefore the event sorting for SPEDE, and subsequent analysis, was done using channels defined in the program as belonging to SAGE. Since this is merely a way of arranging the data from a group of segments into a similar array of events, without confusing it with other type of events such as γ-rays detected by the JUROGAMII detectors, it is a valid approach.

GRAIN writes data to an AIDA (Abstract Interface for Data Analysis) file, which was developed by researchers at CERN, LAL, and SLAC, to define a set of interfaces and formats for representing common data analysis objects. AIDA files are written using a compressed version of XML, but which is not directly compatible with the C++ ROOT libraries for displaying data. However, ROOT does include algorithms from libxml2, a

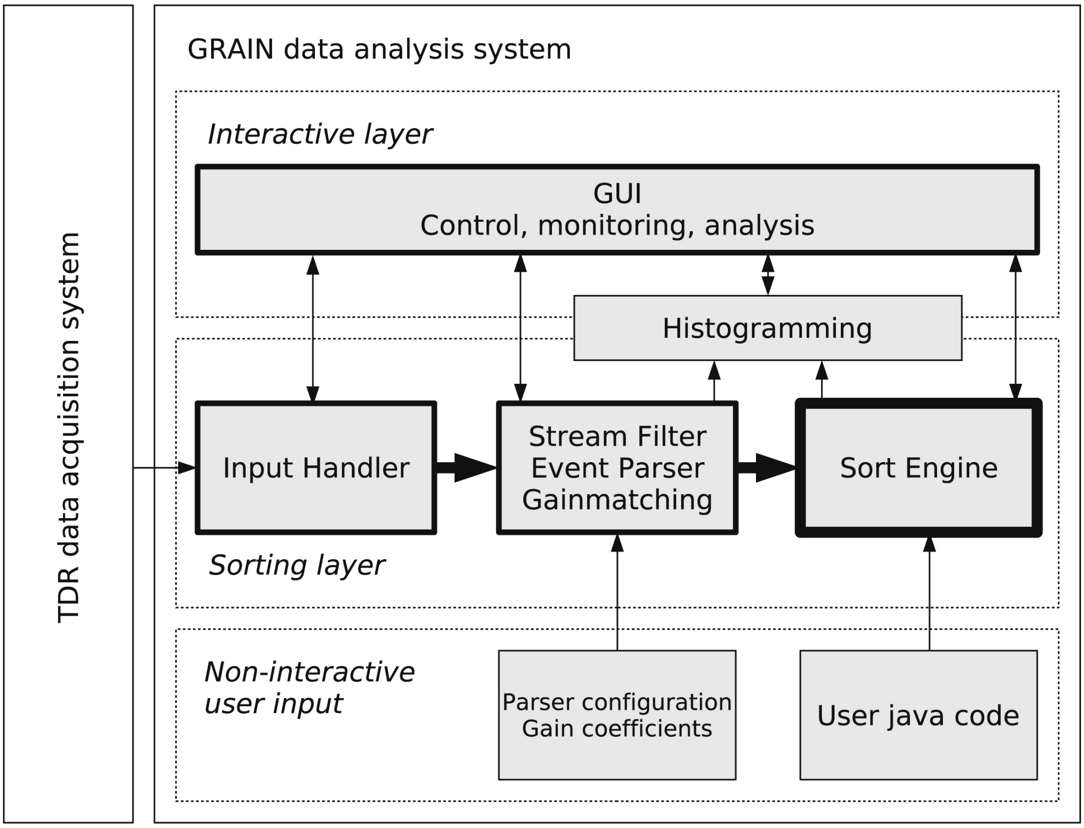

Figure 4.14: A schematic for the TDR DAQ system at the JYFL laboratory, Finland. This system was used to capture and process the events seen by SPEDE during in-beam testing.

software package written in ANSI C for parsing XML documents. Therefore, a parser was created to extract data from the AIDA files and use it to create ROOT files, as there is no method to create the ROOT file from the timestamped data produced by the TDR.

4.6.2 In-beam detector setup

Due to the upgrades at the ISOLDE facility in CERN, and for advantages in flexibility, it was decided to combine SPEDE with facilities at the University of Jyväskylä, including the JUROGAMII germanium array. JUROGAMII is an array of Compton-suppressed HPGe detectors provided by the EUROBALL collaboration and the UK-France detector loan pool, and includes 24 clover detectors (each in four segments) surrounding the target position, and 15 ‘phase-I’ detectors at backwards angles. Compton suppression is provided by BGO shields. The array is seen in Figure 4.15 For the series of experiments shown in this thesis, three clover detectors were used for initial commissioning, and one phase-I specifically mounted for part two of commissioning.

Typically, particles that interact at the target position of JUROGAMII pass through into RITU (Recoil Ion Transport Unit), a large gas-filled recoil separator. Due to the size requirements of RITU, and that of the electronic feedthroughs for the CD particle detector

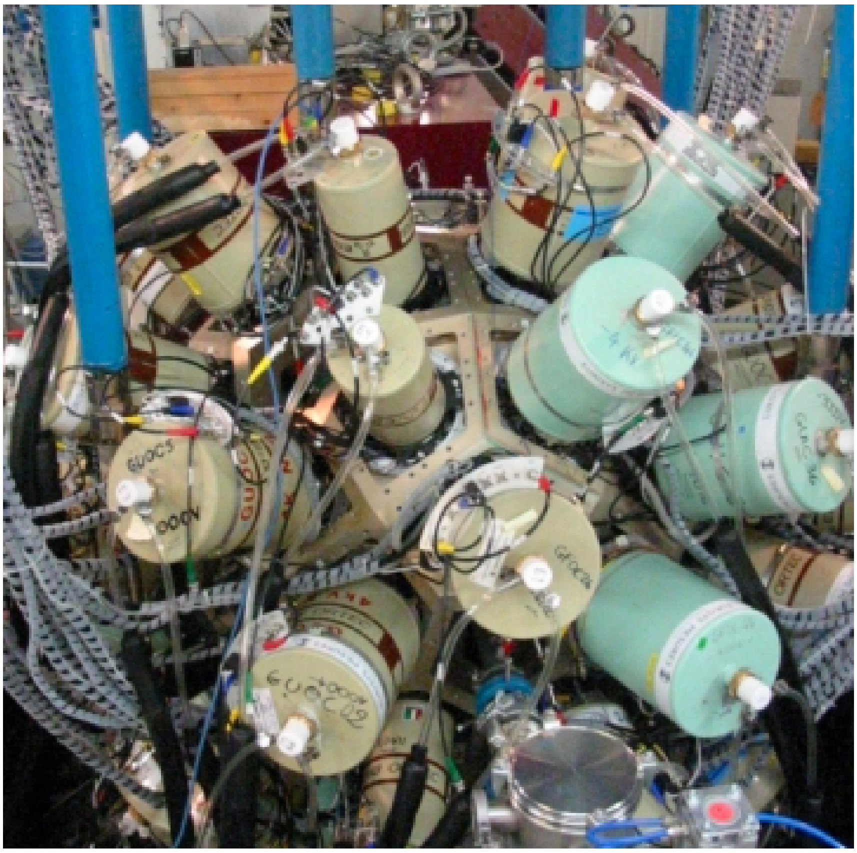

Figure 4.15: The JUROGAMII array

used with MINIBALL, new solutions were required for particle detection. Initially, a small 1 cm^2 PIN diode was used as a beam dump to have a reliable method of observing whether beam was successfully reaching the chamber, but it was not sufficient for particle-electron coincidences. Subsequently, an 8-PIN diode particle detector was made (Figure 4.16), on two rings corresponding roughly to expected high- and low-COM scattering angles of ^{197}Au, with output mediated by a Mesytec preamplifier box. However, the resistance of this device could not be increased enough to compensate for the relatively high energy of the beam particles interacting with the detectors, and thus no energy information could be obtained. The same applied for a particle detector which consisted of one ring of 6 PIN diodes (Figure 4.16), but this was successfully coupled with an attenuator for the final experimental run.

In the scenario outlined, where particle detection can take place but no energy information can be obtained, it may appear that since position information has been obtained, a Doppler correction can be obtained, especially since Coulomb excitation can be approximated using Rutherford scattering (see eq. 2.8) giving us a possible energy range. One could suggest some average value is used, such that the energy dependent terms become constant, and the fractional Doppler shift is represented purely by some function of θ. In the case of the single ring PIN diode array, φ_1 is also constant, such that the variables

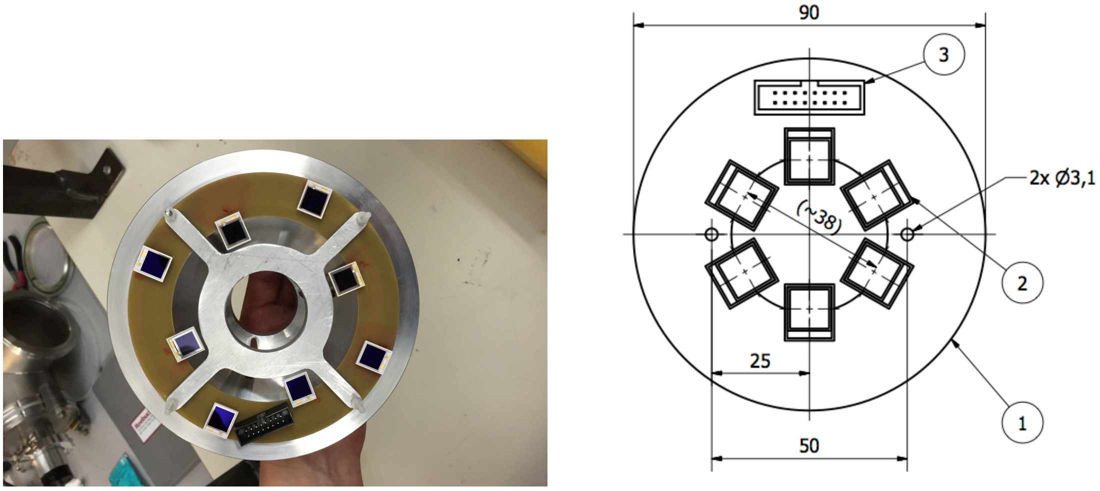

Figure 4.16: Left, the 8-PIN diode array particle detector used for the first part of SPEDE commissioning in February 2015. Right, the 6-PIN diode array particle detector used for the second part of SPEDE commissioning in May 2015, due to issues noted in the first commissioning run.

of interest are ϑ_1, ϑ_2 and φ_2. This leads to, in the case of the 6 PIN array, 144 possible fractional shifts. Since radiation is emitted isotropically in the nuclear frame of reference (ignoring multipolarities), any segment in each ring is equally likely to detect an emitted electron; although between rings the likelihood of detection decreases as the distance from the centre of the detector increases. This is one reason why segmentation is important when dealing with moving sources of radiation, in order to determine cosθ accurately.

Going on, the largest Doppler shift at a given energy will occur when the radiated electron is ejected in an opposite direction to the velocity of the projectile; that is, where θ is 180°. Similarly, the shift is minimised when the radiated electron is ejected at the smallest possible angle to the direction of travel. The Doppler shift also tends to infinity as the speed of the projectile tends towards the speed of light. However, due to the finite width of both SPEDE segments and the PIN diodes, an upper and lower bound can determine how effective a Doppler correction would be. One would expect at beam energies used for ^{197}Au on ^{197}Au reactions in this experiment a minimum fractional shift of about 1%, and a maximum fractional shift of around 8%. The expected scattering of the beam would lead to nuclei with an energy range of around 88 keV/u being detected (about a 3% range compared to the energy of the scattered nuclei). Clearly, this implies that due to the well-known scattering distribution, if the detector positions are known to a high degree of accuracy an energy shift can be inferred that is accurate to less than 0.1 MeV. Without any specific energy information, a distribution of expected shifts can be created using some mean expected energy, and in fact, due to the angular resolution of each segment or PIN diode, this should lead to an accurate Doppler correction within approximately 0.5 keV from the shift that would be measured with the true particle energy detected. However, the experimental setup is still limited by the angular resolution of each segment. It is important to note then that the error in θ can increase rapidly, especially in the case where detectors are close to the target.

The error on eq. 3.13, ignoring the intrinsic resolution of the detectors, is

$$\Delta E_0 = E' \sqrt{(\frac{\beta \sin\theta}{1-\beta\cos\theta})^2(\Delta\theta)^2 + (\gamma\frac{\beta-\cos\theta}{1-\beta\cos\theta})^2(\Delta\beta)^2} \qquad \text{(eq. 4.1)}$$

and the error on $\cos\theta$ is given by

$$\begin{aligned}\Delta\theta = &(\cos\varphi_1 \sin\varphi_2 \cos(\vartheta_1-\vartheta_2) - \sin\varphi_1\cos\varphi_2)\Delta\varphi_1 \\ &+(\sin\varphi_1\cos\varphi_2\cos(\vartheta_1-\vartheta_2) - \cos\varphi_1\sin\varphi_2)\Delta\varphi_2 \\ &-\sin\varphi_1\sin\varphi_2\sin(\vartheta_1-\vartheta_2)(\Delta\vartheta_1+\Delta\vartheta_2).\end{aligned} \qquad \text{(eq. 4.2)}$$

4.7 Simulations

The SPEDE setup was simulated using the Geant4 (GEometry ANd Tracking) toolkit provided by CERN. Geant4 is a library of classes which can be used to model the interactions of particles and matter, with applications encompassing a wide range such as high energy hadronic, nuclear, and accelerator physics, plus medical and space science [92].

Initial simulations were developed by Joonas Konki at the University of Jyväskylä, which were used to determine the optimum number of silicon segments for use in SPEDE that minimised Doppler broadening. This work is summarised in [84].

One change shown here has been to incorporate the use of 'low energy' physics libraries as opposed to the standard electromagnetic Geant4 libraries for simulating particle interactions. This was of particular importance to the simulations as one requirement was to attempt to recreate the δ electron flux from any beam-target interactions, however Geant4 does not model these interactions well, even when using libraries that are more suited to the energy range, principally because it is a framework that was designed with the collisions and resulting jets of particles from high-energy interactions in colliders such as LEP (Large Electron-Positron) and LHC (Large Hadron Collider). These result in fragments with energies orders of magnitude higher than δ electrons, and subsequently the very low-energy data can be ignored.

A major difficulty in simulating a low energy background came from optimisations to the Geant4 package which puts the lower energy for interactions at 0.25 keV. Geant4, compared to Geant3, uses a minimum penetration depth to determine the cut-off energy for ignoring particles. Although this can be set to a very small number, this comes at a high computational cost, as it requires a large number of calculations for each single particle. Even with pulsing, we would expect to see several thousand δ electrons per second, however when simulating a realistic beam-on-target event most events generated were in the forward direction. Although these can be in effect voided by stopping any calculation on deltas that are produced in forward angles, it was still computationally difficult to reproduce a realistic δ electron background. The decision instead was made to simulate three low-energy Gaussian distributions of electrons, with an average energy of 1, 5, and 10 keV.

This is a realistic simulation of the environment that SPEDE is subject to in experimental conditions. There is a noticeable detrimental effect of the number of electrons detected when there is an inclusion of the full geometry of the additional parts of the chamber, as would be expected. The simulations illustrated here do not use nuclear cross-sections for exciting and de-exciting nuclei, but instead, generate a realistic emission of electrons at a given energy. This leads to a more efficient computation, as beam nuclei which do not interact with the target nucleus will not be registered by SPEDE (as no electrons of interest will be emitted), and so can be ignored; not doing so would lead to wasted CPU cycles tracking particles which are of no interest.

The initial package used for simulating the electron paths was standard electromagnetic library 4, included with Geant4. Two packages which are optimised for low energy were used to study any differences at the region where δ production would be expected; these were the Livermore package, produced by the Lawrence Livermore laboratory, and the PENELOPE (PENetration and Energy LOss of Positrons and Electrons) package. These have been evaluated separately as well as in great detail, and, especially PENELOPE, were developed with low energy Monte Carlo simulations in mind [93]. These physics lists use models with an energy range of 250 eV up to 100 GeV for γ-rays, and 10 eV up to 100 GeV for radiated electrons. A cut of 10 μm was used to ensure electrons with low energy would not be discarded by the simulation, whilst ensuring those that would not react significantly were still discarded. 1×10^6 events were created for each simulated run, and each run used the same random seed to ensure results were fully reproducible.

The changing of physics libraries did not result in any noticeable difference between the resulting histogram spectra, neither when simulating a static source, or a beam-target-like production of electrons (that is, with recoiling nuclei). The standard libraries from Geant4 have been used satisfactorily for many other simulations in nuclear physics, such as SAGE and MINIBALL, at the energy range of most gamma-rays and converted electrons. Differences noted between simulated and experimental results could be explained by the low energy thresholds in the data acquisition system used in reality, or be an effect of low-energy pileup that is not simulated well.

Interactions at low energy are in theory best simulated by the alternative physics libraries used, but do not seem to manifest as a noticeable effect seen with different energy events in SPEDE. It is feasible that under actual experimental conditions, many low-energy events occurring within a very short time frame (as would be expected with δ

electrons) would be recorded as one large continuous pulse.

Other changes in the simulations were to include a more realistic geometry (with the inclusion of the target ladder and chamber), and the addition of MINIBALL detectors, rather than JUROGAMII, although none of the data from γ-rays is presented here.

Shown in Figure 4.17, after changes that had been made to materials and detector distances from target, a simulation was run to ensure that the result was still similar to that presented by J. Konki, with a ^{188}Pb beam of energy 2.82 MeV/u incident on a ^{112}Cd target. The simulated FWHM was 10.4 keV, compared to the 9.2 keV seen by Konki.

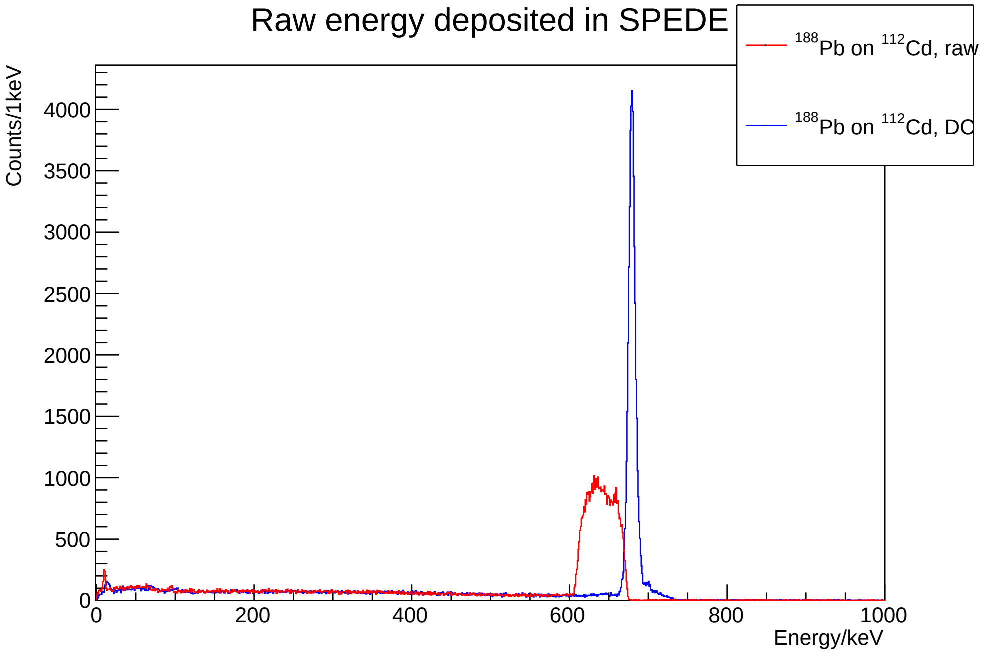

Figure 4.17: Simulated ^{188}Pb on ^{112}Cd, with Doppler correction. This is simulated using the standard electromagnetic libraries. As expected, a clear peak emerges from the particle-gated but kinematically uncorrected data.

This was followed by checking the effect of different energy libraries on the lead data at high energies. Some slight differences were seen in individual counts (illustrated in Figure 4.18), but no change in distribution is noted, implying that they are all equally valid at this energy range.

In order to examine the effect of different beams, beam energies, and electron energies, several different examples were run in order to ensure consistency. Taking an example of a gold beam at 4.1 MeV/u on a cadmium target, nothing unusual is seen within the modified simulations (Figure 4.19).

These initial simulations were used as proof-of-concept that with kinematic correction a segmented silicon detector could produce precise measurements of electron energies. For the experimental runs, with a physical detector, the CD detector was not available for practical reasons in the laboratory environment, and so an array of PIN diodes was used.

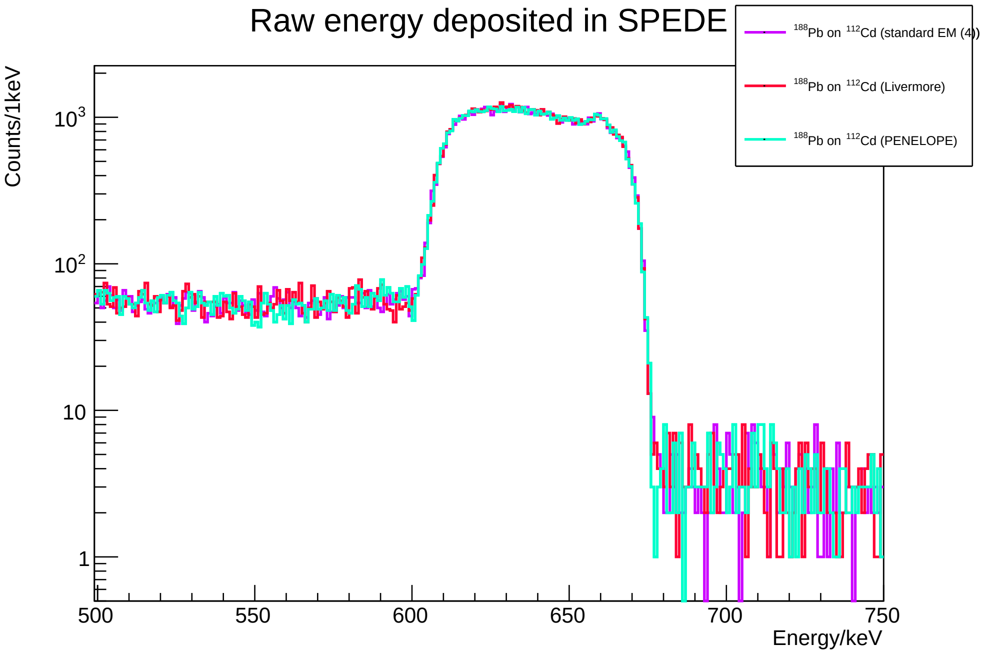

Figure 4.18: Simulated ^{188}Pb on ^{112}Cd using different energy libraries

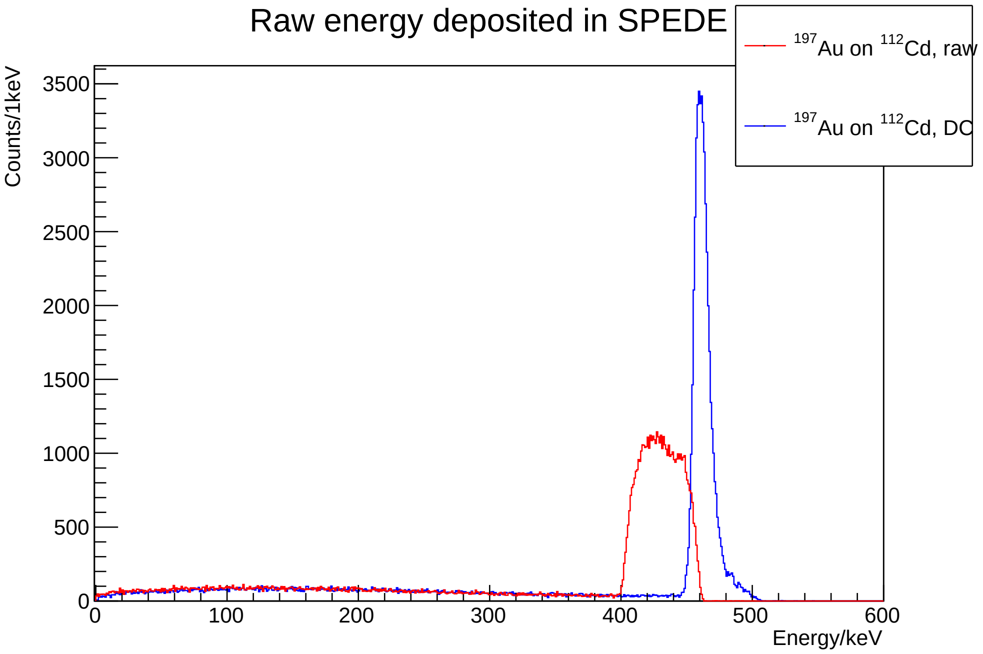

Figure 4.19: Simulated ^{197}Au on ^{112}Cd, with Doppler correction

These were incorporated into the simulation to determine what the expected results should look like. Since the experimental runs did not have an accurate energy measurement, an expected value was used for kinematic corrections for those runs as well as simulated data. As can be seen in Figure 4.20 the peak after Doppler correction has much fewer counts than that seen with the simulation using the CD detector. This is principally due to the much smaller combined area of the particle detection as compared to that of the CD, which essentially covers a large majority of the particle scattering solid angle. A hit map for the two detectors is shown in Figure 4.21.

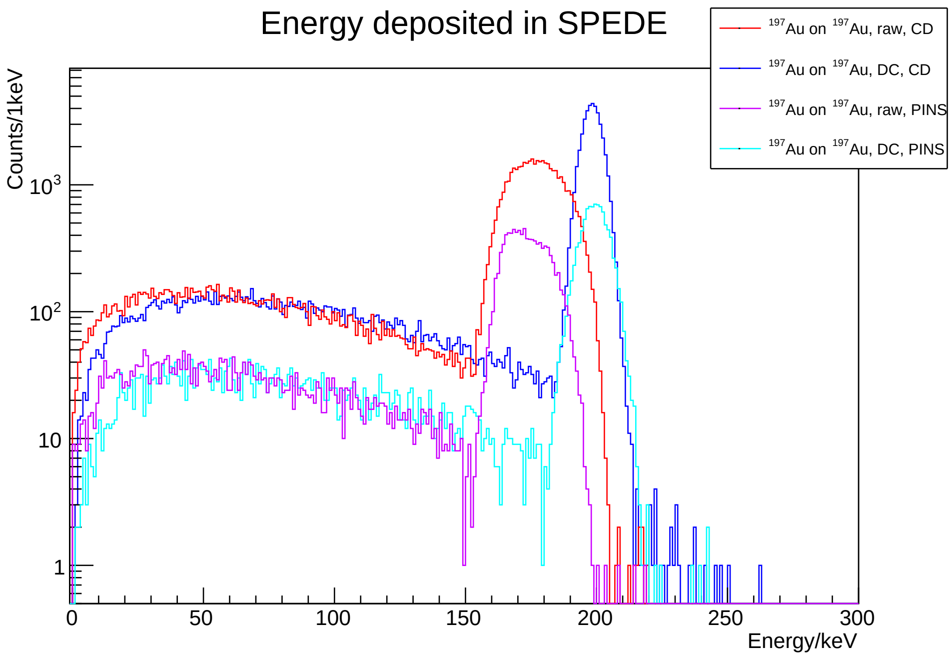

Figure 4.20: Simulated ^{197}Au on ^{197}Au, with Doppler correction, using different particle detectors. Using the CD detector, the number of electrons detected in coincidence with a particle is higher. Additionally, the resolution is slightly improved.

Two low-lying transitions in ^{197}Au are separated by only 10 keV in energy. These would be expected to appear as a doublet in resulting electron spectra. Using the probability of decay calculated from GOSIA, the simulated spectra were combined, with the results shown in Figure 4.22. The calculated yields from GOSIA are shown in Figure 4.23.

Of particular interest was the effect of different libraries on the low-energy range of the electrons. To do this, three Gaussian distributions of electrons, with a mean of 1, 5, and 10 keV, were simulated with a FWHM of 7 keV. However, the distributions remained very consistent with each other, at all energy ranges. The same was true whether HV was applied or not; in Figure 4.24, with no HV applied, and in Figure 4.25, with 5 kV applied to the target ladder and the resultant EM field simulated, each dataset is consistent with the others within that energy range. The application of the HV does however show the expected effect of shifting the distribution to lower energies. This is illustrated

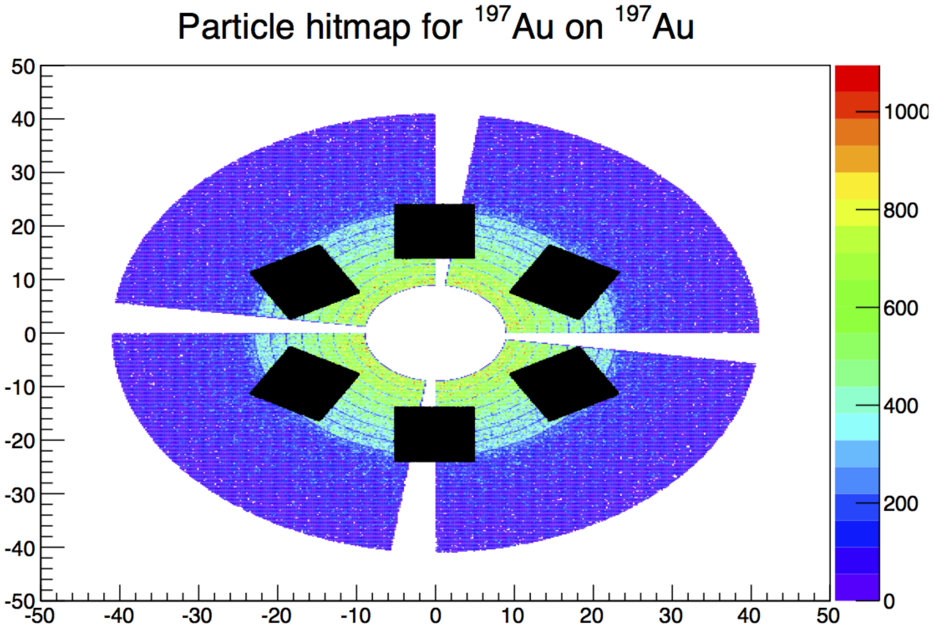

Figure 4.21: Here, the CD detector is shown in colour, with number of simulated hits of ^{197}*Au on* ^{197}*Au given according to the colour scale on the right. A PIN diode array is shown in black on top of this CD illustrating the difference in cross-section for each detector setup.*

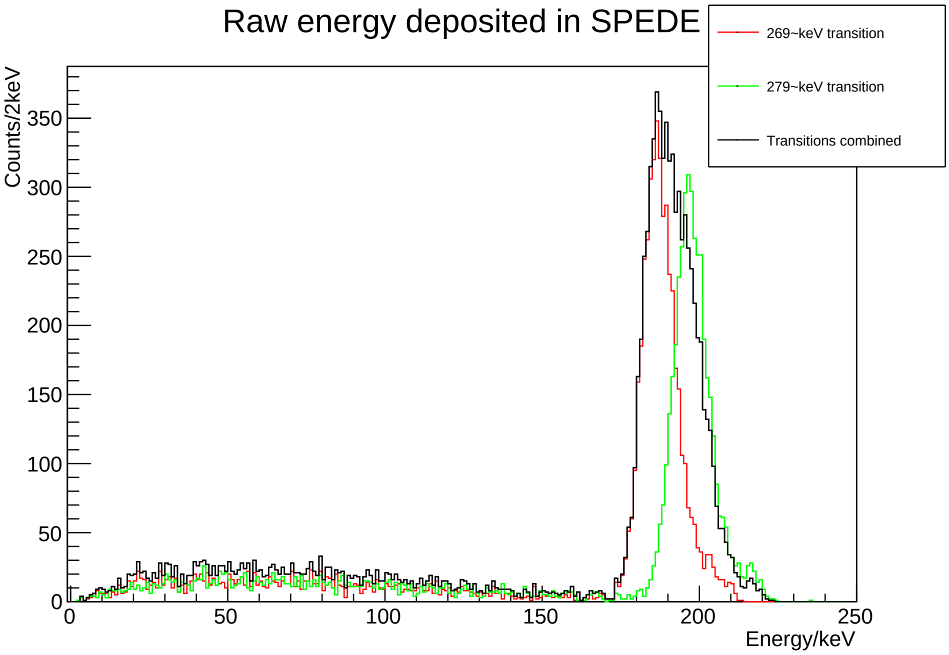

Figure 4.22: Simulated ^{82}*Kr on* ^{197}*Au, combining the 269 keV and 279 keV K-shell decay lines according to a GOSIA simulation of the probability of excitation. The FWHM of each peak is 11.7(1) keV.*

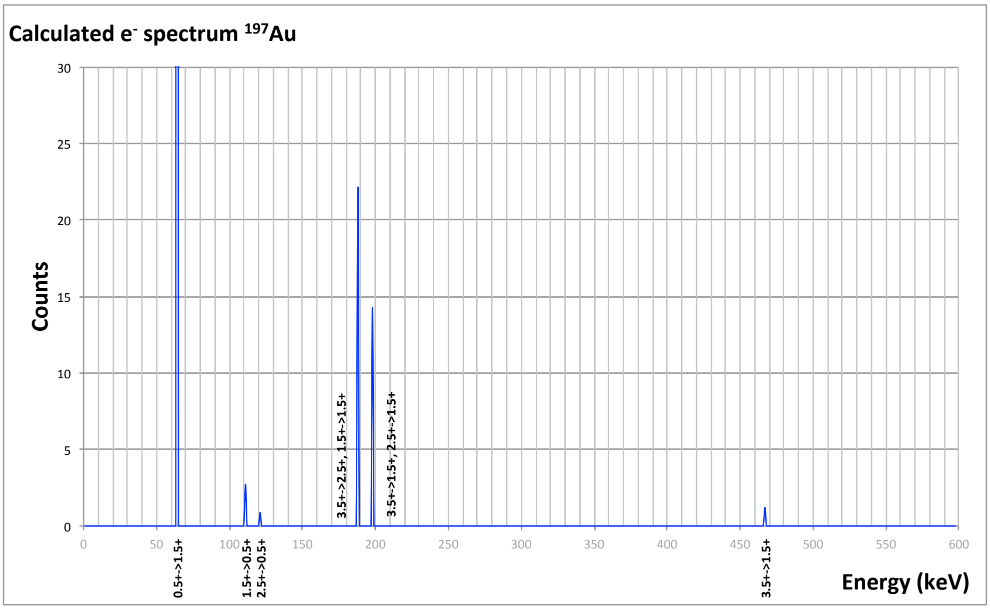

Figure 4.23: Calculated yields of electrons emitted from target nuclei, with a ^{82}*Kr beam incident on* ^{197}*Au. Calculations were performed using GOSIA, and normalised to the 279 keV transition between the* $\frac{5}{2}^{+} \rightarrow \frac{1}{2}^{+}$ *transition.*

in Figure 4.26, using the standard electromagnetic libraries.

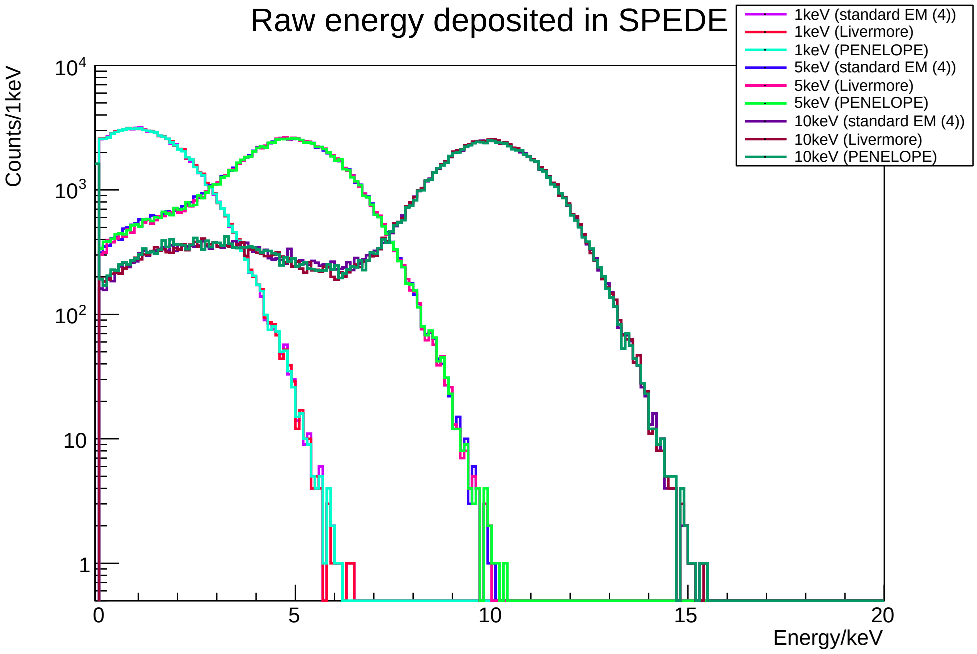

Figure 4.24: Simulated low-energy electron distributions, using different energy libraries. No statistically significant differences appear.

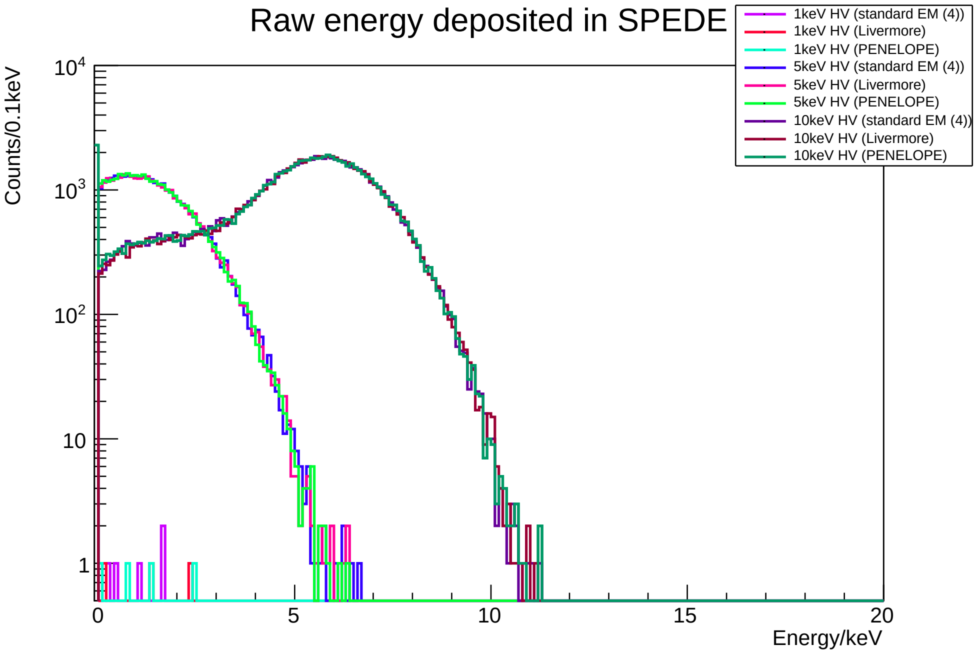

Figure 4.25: Low-energy electron distributions, using different energy libraries, with high voltage simulated. This is similar to Figure 4.24, but it is worth noting that the 1 keV distributions have very few counts. This is expected, and shows the high voltage is being applied in the simulation correctly.

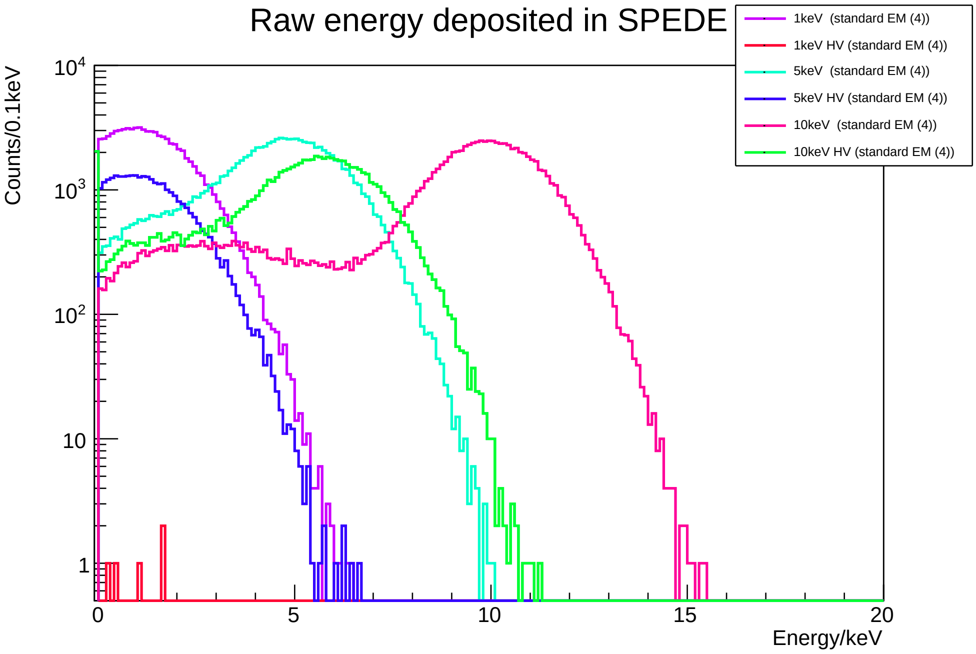

Figure 4.26: Here we can see three distributions using the standard electromagnetic libraries, both with and without high voltage applied. The shift is very clear, although it should be noted that both the 5 keV and the 10 keV distribution appear to shift by only 4 keV rather than the expected 5 keV. There is also a drop in the electron flux when voltage is applied, which is the expected behaviour.

	Type	**Compact**
Magnet	Bending limit	130 MeV
	Focusing limit	90 MeV/u
	Average field	1.77 T
	Number of sectors	3
	Hill angular width	51 - 81 deg
	Spiral	58 deg
	Pole diameter	2.40 m
	Extraction radius	0.94 m
	Hill gap	0.174 m
	Valley gap	0.330 m
	Trim coils	15 x 2
	Harmonic coils	4 sets
	Main coils	2
	Total Ampere Turns	400000 At
	Max current	1000 A
	Iron weight	308 tons
	Total coil weight	15 tons
	Main coil power (max)	130 kW
	Trim coil power (max)	22.5 kW
RF	Frequency	10 - 21 MHz
	Harmonic modes	1, 2, 3
	Number of dees	2
	Dee angular width	78 deg
	Voltage (max)	50 kV
Injection	Ion sources	Multicusp (H-, d-), 6.4 GHz ECR, 14 GHz ECR
	External injection	Axial
	Buncher	Single gap, 1st and 2nd harm
Extraction	Elements	
	Electrostatic deflector	50 kV (max)
	Electromagnetic channel	1250 A (max)
	Passive focusing channels	Horizontal + vertical
	Stripper	For negative ions
Vacuum	2 cryo pumps	5000 l/s each
	Vacuum	5e-6 Pa

Table 4.2: Full description of K-130 cyclotron [90]

5 In-beam experiments

"'Forty-two,' said Deep Thought, with infinite majesty and calm."

Three phases, of testing and development, initial commissioning and final commissioning took place in November 2014, February 2015, and May 2015 respectively. The initial proposal to the JYFL PAC asked for 2 periods of 2 days for testing, and 4 days for commissioning, however due to problems with the cyclotron during the runs this was extended. The GRAIN analysis software was used to sort the data from the acquisition system, outputting AIDA files in a compressed XML format, with that data then sent through an XML parser to produce ROOT files (which are binary files of consecutive data records). Plots in this thesis are presented using the ROOT package, a C++ object-oriented framework for large scale data analysis developed at CERN mentioned previously. Data for fitting parameters, such as for a FWHM (Full Width Half Maximum), were done using the Theuerkauf peak fitting function [94] from HDTV, a successor to the TV program produced at IKP that is integrated with ROOT.

5.1 ^{221}Rn

γ-ray data was taken for ^{221}Rn, with results presented here. This provides more motivation for SPEDE by providing a proven experimental need for the later results presented in commissioning.

5.1.1 Experimental background

The analysis of odd-mass nuclei is complicated by the effect of the single valence particle on the collective effect of the coupled nucleons [25]. Thus experimental evidence is needed to provide limits on theoretical models. Additionally, odd-mass nuclei provide an important probe into atomic EDMs. The parity doublets expected enhance the Schiff moment by a factor of up to 100.

Leander and Chen (1988) [26] have had some success previously in calculating decoupling parameters using a reflection-asymmetric particle-plus-rotor model, to the same order, assuming non-zero β_3. A detailed review of odd-A actinide nuclei, and other nuclei around this region, is provided by Leander and Sheline (1984) [27], as well as Sheline and Sood(1986)) [28] and others. Other proposals have been submitted to study this region further using radioactive beams at the ISOLDE facility in CERN, for which work presented here on ^{221}Rn was done to test the feasibility of such an experiment.

In September 2012, an experiment (code IS475) was performed at the ISOLDE facility in CERN, using the MINIBALL array situated at the end of the REX-ISOLDE beamline. Around 30 hours of beam time was obtained with a ^{221}Rn beam of intensity $\simeq$ 6000 particles/s at an energy 2.85 MeV/u incident on a ^{120}Sn target foil of thickness 2 mg/cm^2. One cluster was missing from the MINIBALL array, meaning 18 channels were unavailable for position information, and 3 unavailable for energy information. The disparity in the number of channels detecting position and energy is due to the fact that the energy information is taken from the core segment of each hexagonal 6-fold detector.

Positional calibration of the detectors was done using a beam of ^{22}Ne, and energy calibration using static ^{152}Eu and ^{133}Ba sources in the target position, with activities of 20 kBq (measured 2012/07/09) and 21.1 kBq (2006/05/12) respectively. The fit used for the calibration was quadratic, although a linear fit is a good approximation since the quadratic term is very small. In order to perform the calibration, peaks were analysed in the HDTV package, with the actual energies for transitions in ^{152}Eu and ^{133}Ba given by data from the ENSDF (Evaluated Nuclear Structure Data File) set from the NNDC (National Nuclear Data Center) [95].

5.1.2 Results

The following figures, Figure 5.1-Figure 5.6, are the results from the data collected for experiment IS475. Acquired data was analysed using the C++ ROOT library provided by CERN. A sort was made on the raw data to find all γ-ray events, and timestamp them, along with the particle events in the DSSSD. These files were then passed to analysis code which sorted events in time and energy to create histograms such as those found in the following figures. This analysis code applied a Doppler correction for both beam and target nuclei, looked for γ-γ coincidences, performed a background-subtraction and was used to fine tune some parameters, for example the time window used for background subtraction and offsets for the Doppler correction.

γ-ray events are coincident with a particle detected by the DSSSD and identified using 2-body kinematics, to determine whether it is a beam (^{221}Rn) or target (^{120}Sn) particle. Doppler correction was done event-by-event, again using 2-body kinematics and angular information from the DSSSD.

γ-γ matrices were created by looking at all the events and plotting them in a 3-dimensional plot against each other, with the z-axis representing the intensity. Gating was done on the energies of each peak ±7.5 keV.

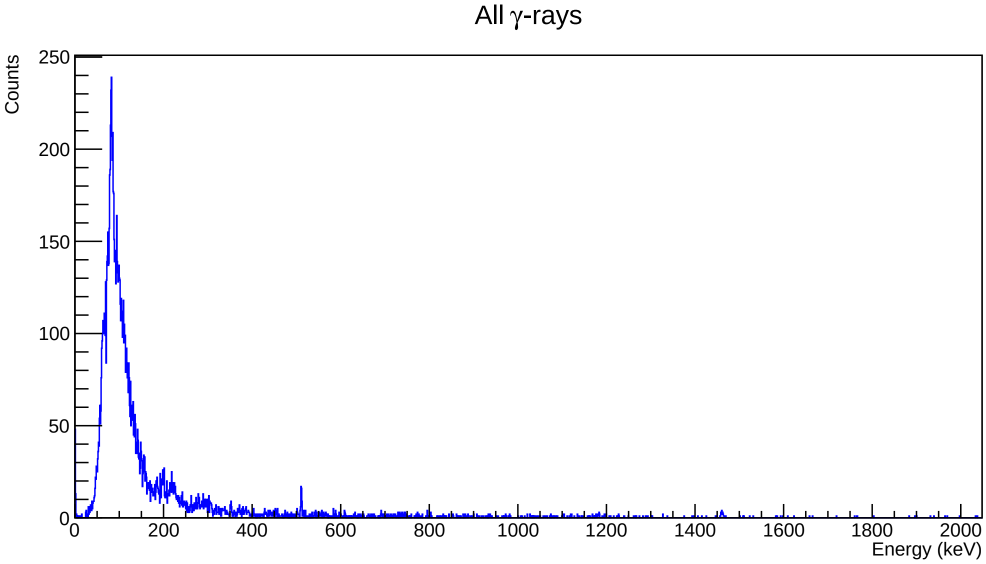

Figure 5.1: γ-ray spectrum showing all γ-rays detected by the MINIBALL array during the course of the experiment. The 511 keV annihilation peak is clearly visible. It is clear that there are a large number of background events. Conditions therefore need to be applied to clear spectra and make peaks visible.

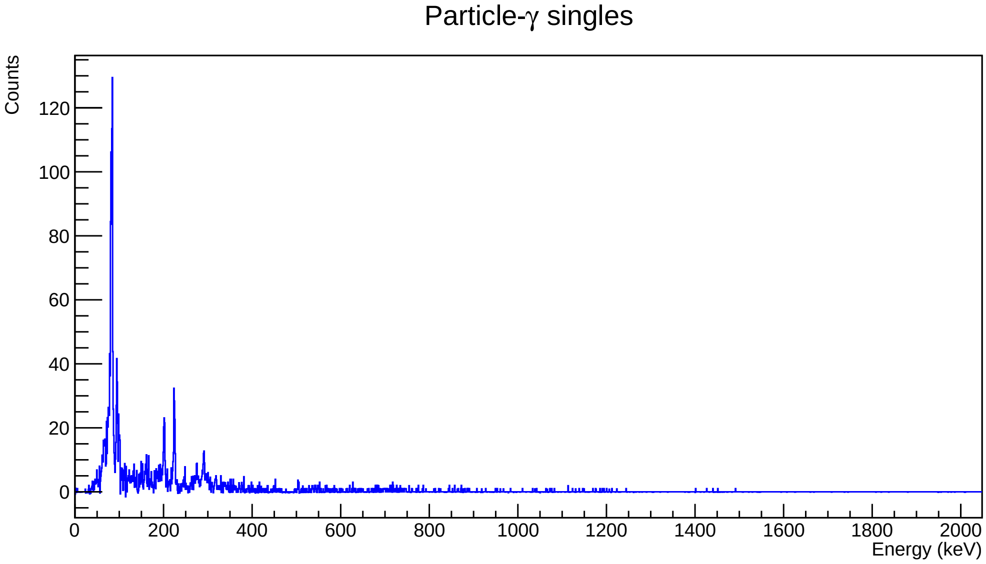

Figure 5.2: γ-ray spectrum showing all γ-rays in coincidence with a particle detected by the MINIBALL array during the course of the experiment.

5.1.3 Discussion

Very little was known about ^{221}Rn before the experiments detailed in this section were conducted in 2012. Three new transitions were observed for the first time, at energies of approximately 200 keV, 223 keV and 289 keV. Coulomb excitation was also performed specifically on odd-mass radon for the first time. As is observed in all the figures (Fig-

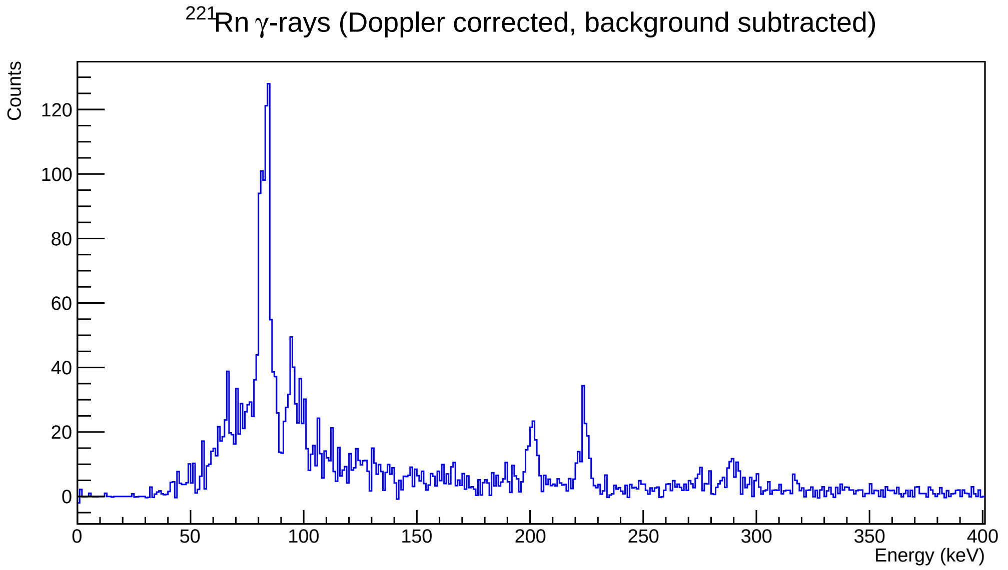

Figure 5.3: Background-subtracted γ-ray spectrum of ^{221}*Rn, Doppler corrected for* ^{221}*Rn. 3 peaks are clearly visible, at 200.4(3) keV, 223.6(4) keV, and 289.7(4) keV.*

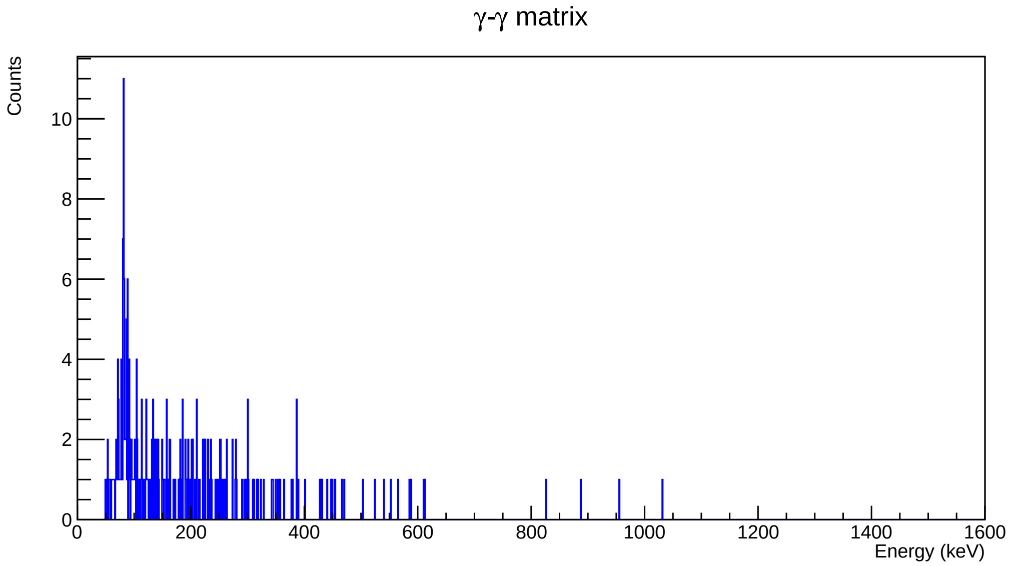

Figure 5.4: Projection of γ-γ matrix showing all coincident γ-ray events.

ure 5.1-Figure 5.6), the count rate is low, and so few peaks are observed in the spectra. This could partly be due to the Coulomb excitation process not exciting any more levels than the 3 shown. However, looking at nuclei around the ^{221}Rn region, it would appear reasonable to expect more levels to be excited. Ignoring X-rays, three peaks are clearly observed in the spectra, labelled A, B and C in Table 5.1.

Efforts were made to look at the possibility of a cascading effect occurring. As peak C had the least counts, it must lie above B and A as lower states have a higher probability of being excited in Coulomb excitation. Due to the fact there were only around 36 counts

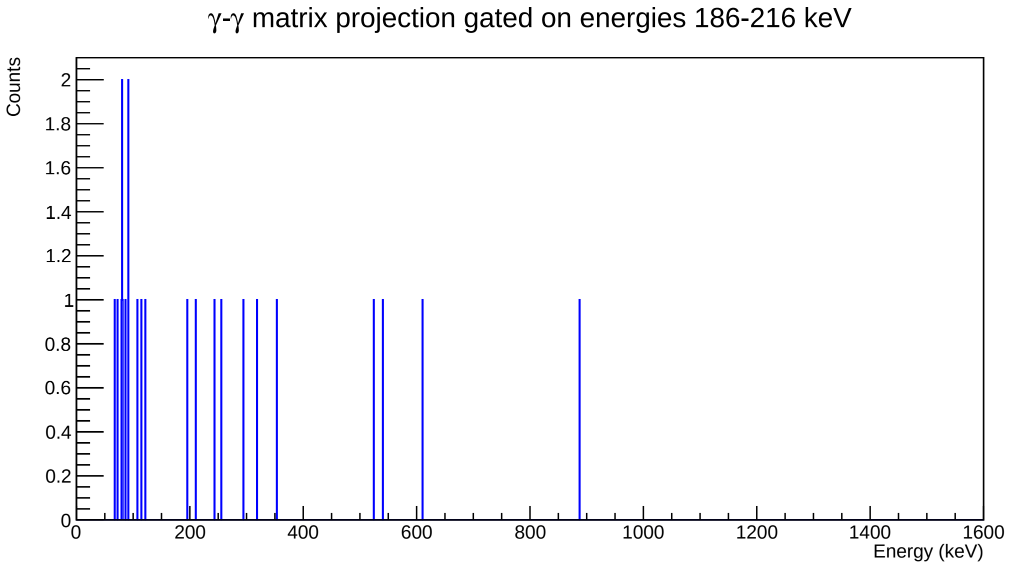

Figure 5.5: Gating on the first peak and projecting the γ-γ matrix, no coincidences with any other γ-ray energies are seen.

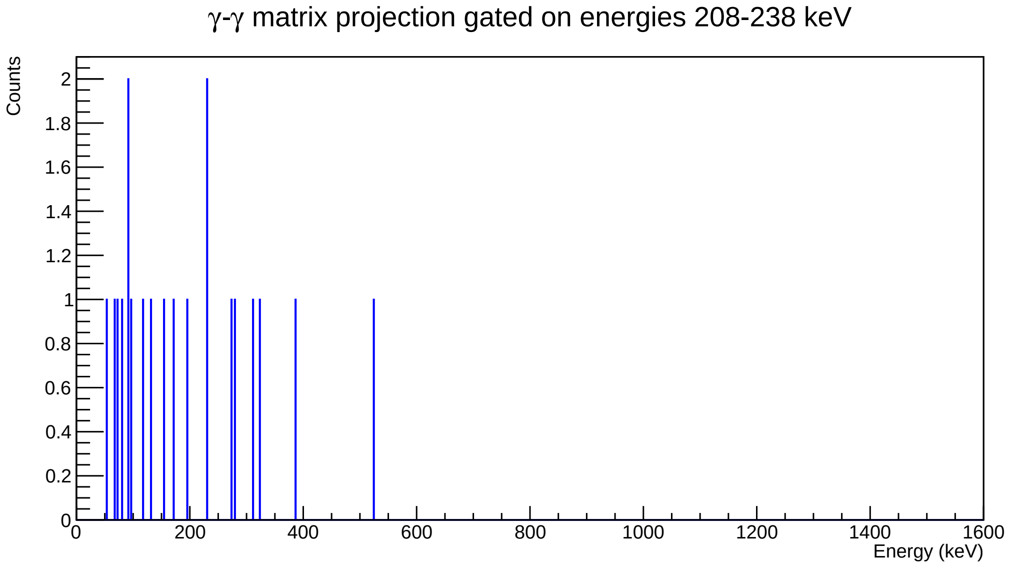

Figure 5.6: Gating on the second peak and projecting the γ-γ matrix, no coincidences with any other γ-ray energies are seen.

in the highest-energy peak C, coupled with the efficiency of the MINIBALL detector ($\simeq$ 10%), the upper limit for counts in any coincidence peak from C would be 3.6 (= 4), assuming a 100% branching ratio and no internal conversion. This is too low to see in these spectra; to separate from random γ-rays all coincident rays would have to occur in the same channel. As a consequence, no conclusions can be made about a cascading effect from peak C coupled with other data. Gating was done on peaks A and B, as seen in Figure 5.5 and Figure 5.6 respectively. Again, as an upper limit the number of counts

Label	E (keV)	Counts	Intensity (raw %)
K_α X-rays	82.4(1)	535(28)	505
K_β X-rays	94.3(3)	99(16)	93.4
A	200.4(3)	84(11)	79.2
B	223.5(3)	106(12)	100
C	288.73(4)	36.5(8)	34.4

Table 5.1: The energies of the three ^{221}Rn γ-ray peaks and the X-rays for all the figures shown in this results section (Figure 5.1-Figure 5.6). Normalised to the highest-intensity γ-ray, B. The separate alpha and beta X-rays were not able to be determined.

from coincidences expected in peak A would be 10, and peak B 12 (taking into account errors on the area of the peaks). No coincidences are seen in peak A or B, however this may imply a low branching ratio for any cascading effects, or a high probability of internal conversion. If there is a high branching ratio, and the transitions proceed by γ-ray decays, then it can be deduced that this is either one state decaying to (probably) the ground state and another low-lying state, or two states lying close to each other decaying to one state (probably ground). Simultaneous γ-e$^-$ spectroscopy will help in identifying any cascading effects.

Efforts were also made using the GOSIA Coulomb excitation code to reproduce the experimental spectrum using the identified peaks and possible structures. However, the ratios of each transition could not be reproduced with any model. Theoretical predictions made by Leander and Chen imply the ground state (of spin $\frac{7}{2}^+$) has a positive parity due to band-mixing with a state near the Fermi level with $K = \frac{5}{2}$, where K is the quantum number of the sum of the total angular momentum of the core electrons, plus the orbital momentum of the outer electron. This is difficult to incorporate into any predictions made using GOSIA.

What is possible to conclude is that by looking at the number of counts seen in the X-ray peaks, it is clear there is a large amount of internal conversion occurring. This indicates a high internal conversion coefficient, and proves the experimental requirement for SPEDE. Simultaneous observation is needed to fully understand the de-excitation processes, by allowing the possibility of determining coincidences between, and the multipolarity of, de-exciting transitions.

With the capabilities of SPEDE, coupled with the benefits of the HIE-ISOLDE upgrade and a higher beam current, much more information can be obtained about this nucleus, making it possible to place the observed transitions into a level scheme, which will in turn enhance the sensitivity on the measurement of an atomic EDM, with increased sensitivity from odd-mass octupole-deformed nuclei.

This leads to several specific constraints on the detector required. First, it must be sensitive to low-energy electrons, since the likelihood for internal conversion decreases as the energy between states increases. Secondly, it must be shielded somehow from δ-

electrons, occurring from the heavy radioactive beam ions colliding with electrons in the target. Thirdly, it must have a good position sensitivity, in order to correct for the Doppler shift of energies from recoiling nuclei. The need for Doppler shift correction is shown from experiment IS475; the expected shift for electrons is even greater.

5.2 Choice of nuclei of study

The aim of the experiment was to best simulate the environment at ISOLDE, which has pulsed low-rate radioactive beams. Several targets were used over the course of the experiments. Various densities and different elements were required in order to produce differing levels of δ-electrons and examine the effect of mitigating measures. The chosen beam-target nuclei combinations also should have decays which are well-separated and so their origin can be easily identified, as well as having good separation with scattering angles so particle identification is possible. An important criterion for selection is the likelihood of internal conversion; with stable beams, this leads to a general requirement for a high proton number. Since the main aim of the experiments was to examine the capability of an in-beam electron spectrometer as opposed to the study of unidentified levels, the level scheme should therefore be well known. The abundance of elements was not important for beam selection, since the number of particles required is small, but the isotope must be easily separated without risk of contamination in the beam. This is easier to control for with stable beam production compared to the challenges from the methods used for rare-beam production. The K130 cyclotron that was used to produce beams performs separation by using precision resonance to extract the nuclei of interest at a specific energy. The number of particles reaching the target position were minimised with the use of a tungsten collimator placed at the very start of the SPEDE chamber.

With the exception of gold beams, other beams were the noble gases neon, argon, krypton, and xenon. Of these, the lowest-lying level is in ^{132}Xe at 668 keV, and so since the excitation probability of this state is low, coupled with a small internal conversion coefficient, decay radiation produced from the beam nuclei could be discounted since it was far above the region of interest for studying the behaviour of SPEDE. Level schemes of these nuclei, along with targets with high excitation energies, are not provided, but are summarised in Table 5.2.

Four nuclei are therefore particularly suited for studies of internally converted electrons. Their level schemes are provided in Figure 5.7 (^{160}Dy), Figure 5.8 (^{170}Yb), Figure 5.9 (^{197}Au) and Figure 5.10 (^{207}Pb). These were generated using the Radware package with data taken from NNDC, as with radon analysis.

Of these, ^{197}Au was of particular interest as a beam could be obtained too. Properties that make it of further interest include low-lying metastable states which are heavily converted.

The kinematic properties of these beam-target combinations can be seen in Figure 5.11.

Nucleus	**Type**	**First excited state (keV)**	**Number of states below 0.5 MeV**
^{197}Au	Both	77.3	3
^{20}Ne	Beam	1633.6	0
^{40}Ar	Beam	1461.0	0
^{82}Kr	Beam	777.0	0
^{84}Kr	Beam	881.6	0
^{132}Xe	Beam	668.0	0
^{58}Ni	Target	1454.0	0
^{106}Cd	Target	633.2	0
^{116}Sn	Target	1294.0	0
^{160}Dy	Target	86.8	2
^{170}Yb	Target	84.2	2
^{207}Pb	Target	569.7	0

Table 5.2: First excited states of nuclei chosen for beam-target selection.

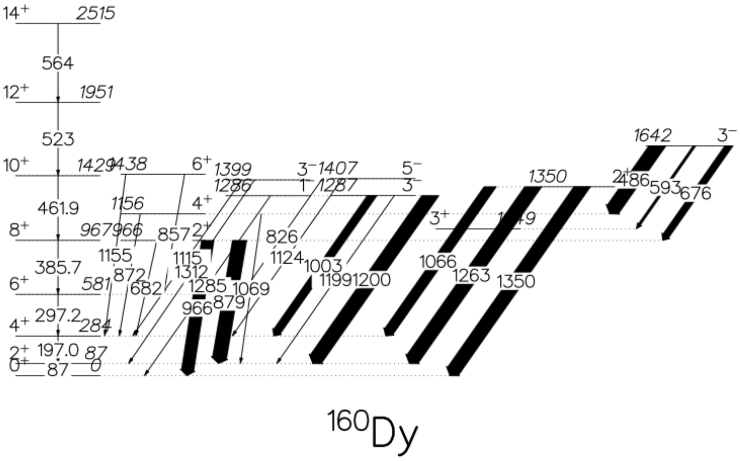

Figure 5.7: Low-lying levels of ^{160}Dy.

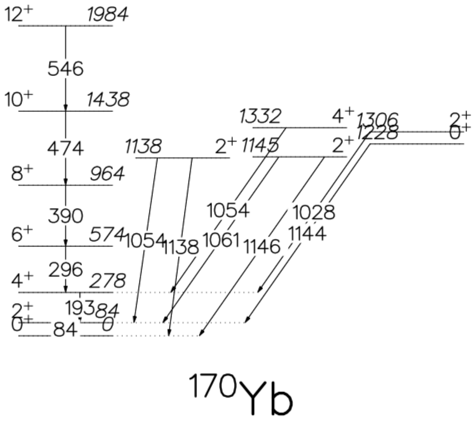

Figure 5.8: Low-lying levels of ^{170}Yb.

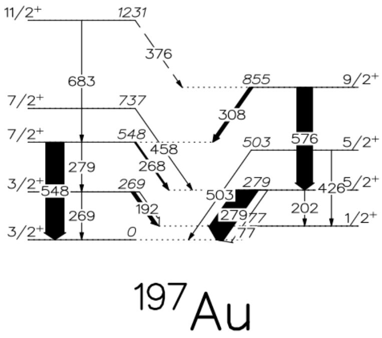

Figure 5.9: Low-lying levels of ^{197}Au.

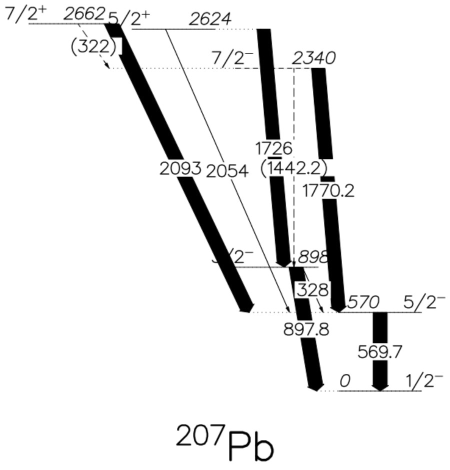

Figure 5.10: Low-lying levels of ^{207}Pb.

The angular coverage of the particle detectors varied depending on the setup used, but the majority of results presented (except where specified) use the 6-PIN diode array positioned 35.9 mm upstream of the target, therefore covering an angular range of 27.3-28.5°. The ideal beam and target combination would have a small change of energy at the position of the detectors, since the energy measurement of the recoiling nuclei was not very accurate, as well as a large separation in energy between the different nuclei. Particle identification for the need of doing a kinematic correction is made much more difficuly by using the same nucleus for the beam and the target material.

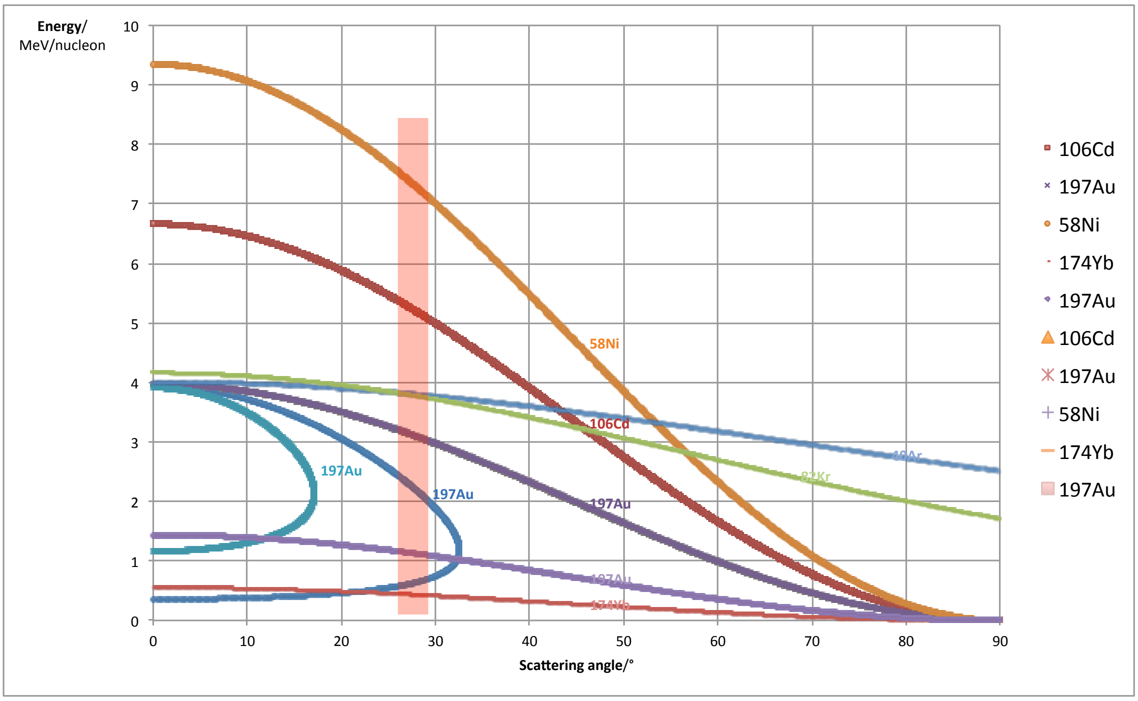

Figure 5.11: This plot shows the energy distribution with angle of scattered nuclei of various beams and targets used in SPEDE tests. Some nuclei, with inverse kinematics, are not seen by the particle detector and therefore can be used for clean gating of the other nucleus. The translucent box shows the approximate angle covered by the 6-PIN array.

5.3 In-beam development (November)

The initial in-beam runs only involved observing SPEDE behaviour in an environment in a production environment, without any γ-ray data from the germanium detectors in JUROGAMII. The small PIN diode used as a beam dump was sufficient to determine whether beam was reaching the chamber, but not for creating particle-electron coincidences, as, with a target in place, no beam could be seen. Two beams were used; ^{40}Ar (10+) and ^{20}Ne (5+), with an energy of 4.1 MeV/u. These were incident on several targets; ^{58}Ni (0.6 mg/cm^2), ^{160}Dy (0.575 mg/cm^2), ^{207}Pb (0.6 mg/cm^2), ^{27}Al (2.7 mg/cm^2) and ^{174}Yb (1.0 mg/cm^2). Plastic was also mounted with beam incident on it in order to determine if there was any mistake in beam alignment, as a result of unusual burn marks noted on the top of the target holder, assumed to have occurred when the target ladder was fully lowered and was being aligned initially. Calibrations were done using a ^{133}Ba source. The resulting calibrated spectrum is seen in Figure 5.12. The PIN diode was uncalibrated, and used purely for hit identification and beam alignment.

Due to the lack of particle information, it was not possible to normalise the data with any degree of accuracy in terms of actual excitation events. An aim was set to keep the time relatively consistent for each run where appropriate. A scaling factor was obtained by finding the largest bin present in the most populated histogram, and using that as a multiplication factor. In this way, the distributions of electrons can be compared. It is a preferred method compared to total beam time or total number of electrons, since the beam current was too low to be measured with a Faraday cup and no particle normalisation was possible meaning the production rate of either δ or converted electrons was unknown when comparing runs.

HV that was applied to the target, in order to shift energies of emitted electrons by -5 keV and thus remove some of the low energy background, was applied with the wrong polarity until run 70, near the end of the experimental run, resulting in accelerating low energy electrons towards the detector. Where appropriate, this is noted expressly in the figure descriptions.

The first run that included beam on a target was ^{20}Ne on ^{58}Ni, shown in Figure 5.13. The beam pulse was set to periods with 100 μs on and 900 μs off. The effect of HV application was not seen with the distribution of electrons and the pileup of δ-electrons not appearing to change, and not enough data is collected to make out any nuclear structure. For either nuclei to decay via internal conversion would be unusual in any case due to the relatively high energies of the first excited state; 2^+ at 1633.7 keV and 1454.2 keV for beam and target respectively. This implies a relatively high background. The lack of effect of HV is noted, as discussed.

With the same parameters, but no target installed (that is, beam was incident on an empty target), δ-electrons were still apparent, as seen in Figure 5.14, implying either a large beam spot or poor centring of the beam on target, such that the beam was striking the target frame. Due to the low beam current and the facilities at Jyväskylä, the beam centring was improved by attempting to minimise the noise from δ-electrons observed on an oscilloscope connected to SPEDE channel 17. Additionally, some peaks can be seen around, for example, 320 keV. This corresponds to a leak of the ^{133}Ba source, which was later confirmed to have leaked into and contaminated the SPEDE chamber. Again HV had no effect due to a negative potential difference applied to the ladder.

An example of the result of a different beam to ^{20}Ne, with ^{40}Ar, is seen in Figure 5.15. What is of particular interest to note is the peaks seen in the range of 500-750 keV for the lead target. They do not appear strongly in the spectrum from ^{160}Dy, but the number of

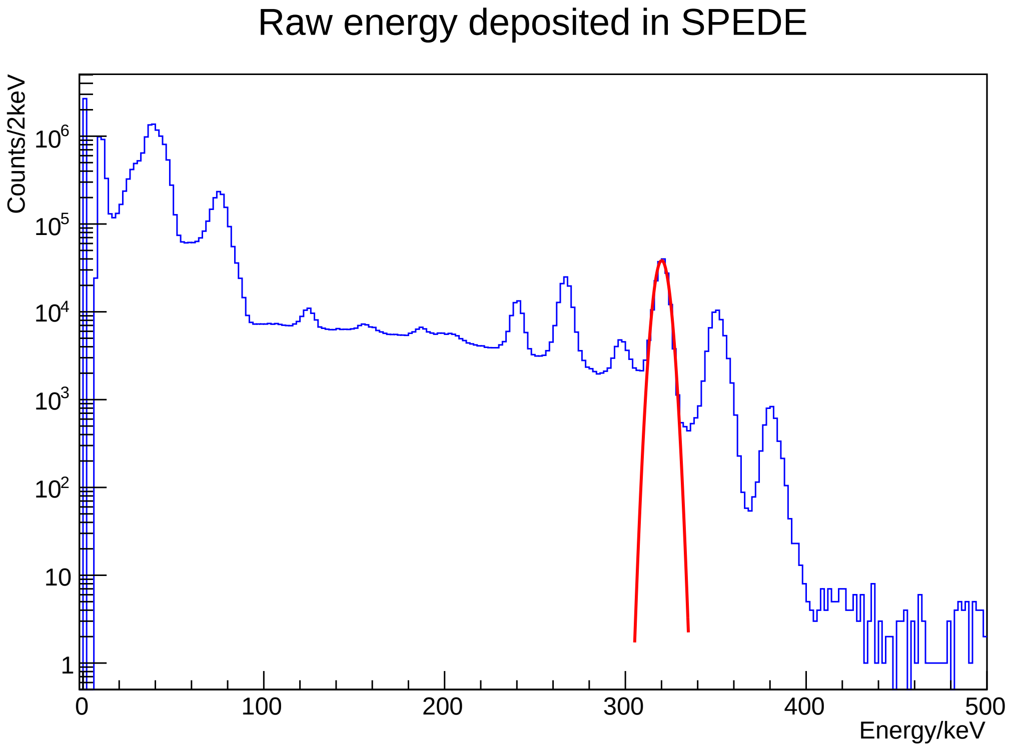

Figure 5.12: Total counts detected by SPEDE from all segments in approximately 40 minutes from a ^{133}*Ba source. No HV or foils are present, and detector is cooled to approximately -30 °C. Position of fitted peak: 320.2(1) keV, FWHM: 7.10(2) keV.*

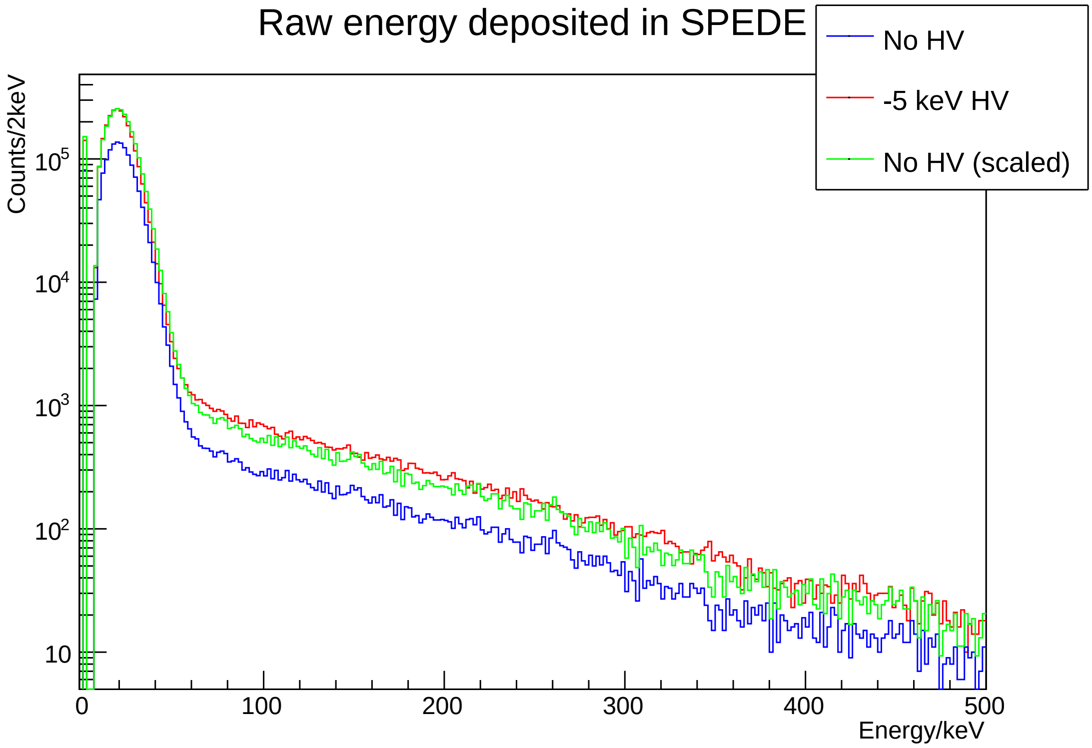

Figure 5.13: Total counts detected by SPEDE from all segments in approximately 3 minutes of ^{20}Ne on a ^{58}Ni target. An aluminised Mylar foil is present. The blue line, illustrating data collected with no HV applied, is scaled to the bin with the maximum counts for HV at 19 keV, and shown by the green line.

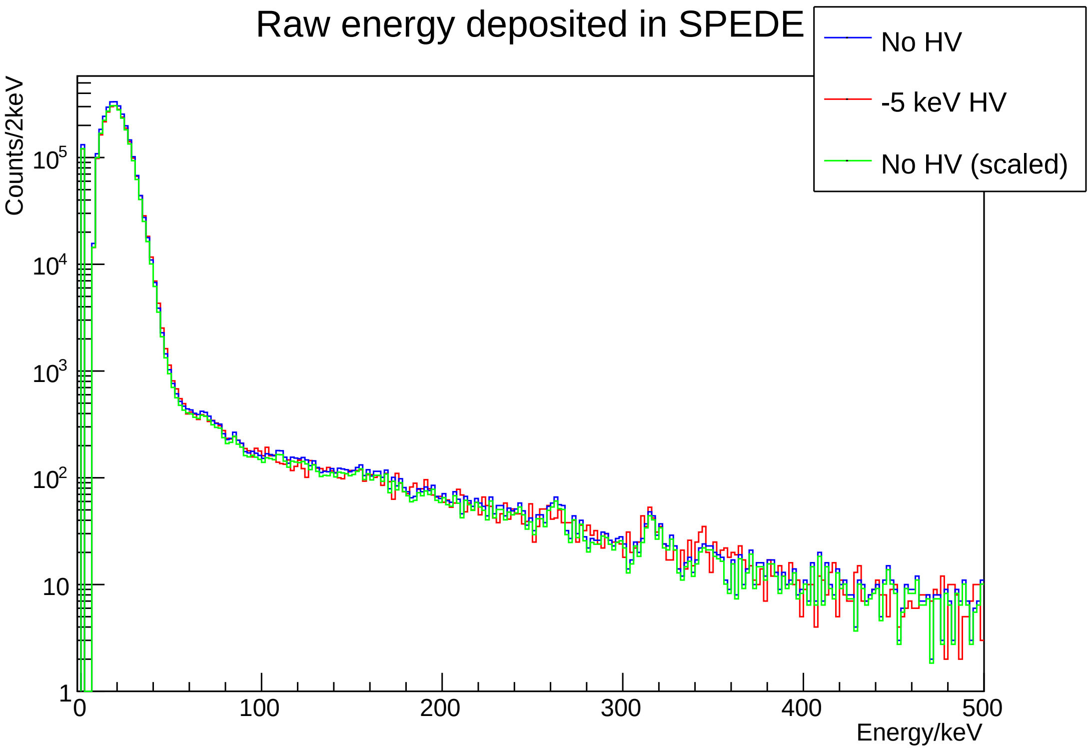

Figure 5.14: Total counts detected by SPEDE from all segments in approximately 4 minutes of ^{20}*Ne on an empty target frame. An aluminised Mylar foil is present.*

counts is of the order of 10^2 less. Peaks would however be expected in any case due to the number of transitions in ^{160}Dy at this range. The lower intensity using this dysprosium target can primarily be attributed to the fact that the pulse off state was 11 times longer; the entire pulse length was increased to 10 ms, with 9.9 ms off. The broad nature of this peak is not in fact likely to be due to Doppler-shifted photons, but instead from the energy of the electrons being greater than the stopping power of the silicon. The broad nature of it would be expected, since different electrons will see a different apparent thickness from hitting the detector at different angles.

^{40}Ar incident on ^{207}Pb is again seen in Figure 5.16. Here, a comparison is shown in the resultant electron distribution when an aluminised Mylar foil (number 1, as mentioned before) with a light guard that was placed in front of the detector. The low energy peak shows a much sharper drop off, implying that the foil performs well in this aspect. It also has a smaller height ratio when compared to the remaining distribution.

At higher energies, no clear peak is seen when compared to the data without a foil present. The broad peak seen around The peaks in this data however correspond to ^{133}Ba contamination, which was removed between the non-foil and foil run.

Although it was not possible during this testing phase to do particle coincidences, it was possible to observe the effect of the application of HV to the target frame on shifting the distribution of electrons, to observe conversion electrons likely emitted from the decay

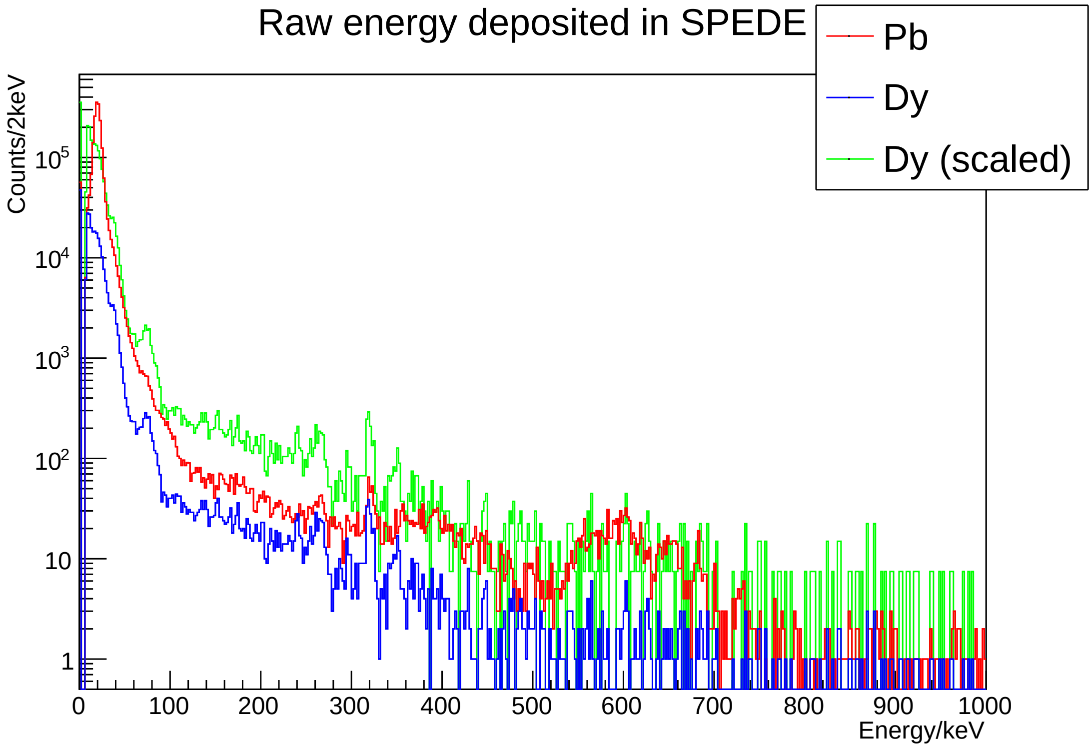

Figure 5.15: Total counts detected by SPEDE from all segments in approximately 12 minutes of ^{40}*Ar on a* ^{207}*Pb (Red) and* ^{160}*Dy (blue) target. No foil is present. Note several peak-like areas over 500-750 keV. Peaks at lower energies can be attributed to contamination from* ^{133}*Ba.*

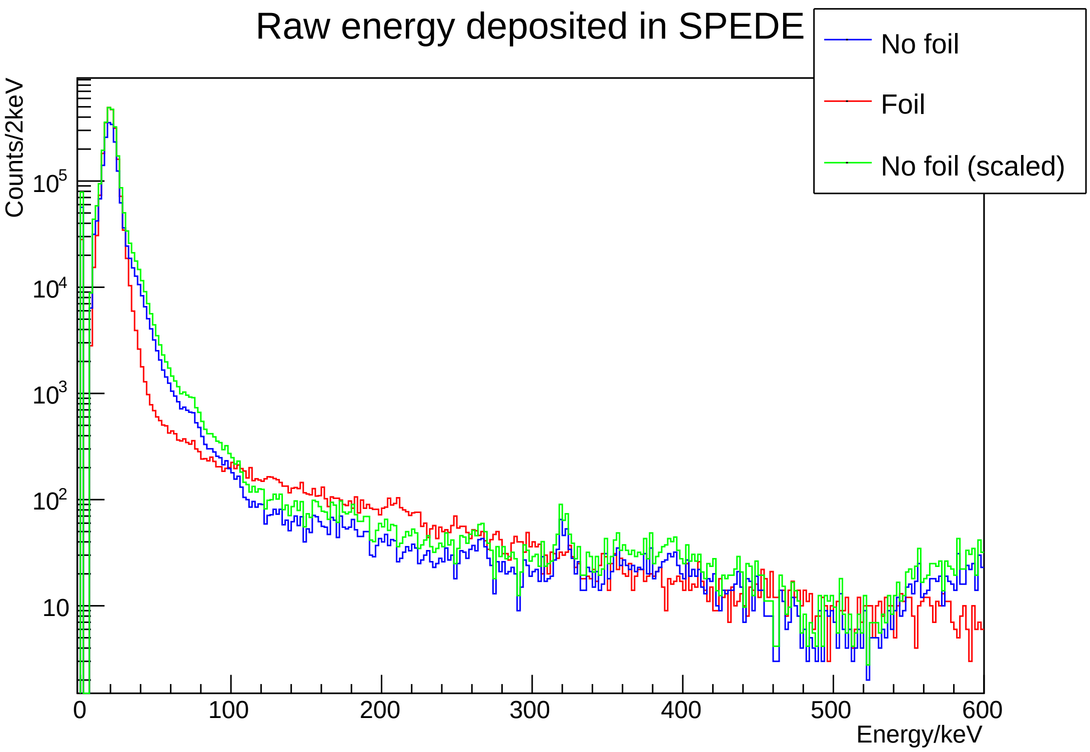

Figure 5.16: ^{40}*Ar on* ^{207}*Pb, with & without foil.*

of nuclei excited via a Coulomb interaction, and to note the attenuation effect of foils in front of the spectrometer. Background from δ-e$^-$ production was suppressed enough to see limited spectroscopic information. This was deemed sufficient to proceed to continue on to commissioning runs, as the concept of in-beam electron spectroscopy without transport fields, using low-rate collimated beams, was proven to be possible.

5.4 Initial commissioning (February)

The first part of commissioning used a bespoke particle detection setup, as well as 4 clover detectors from JUROGAMII. However, one was behaving erratically and could not be fully biased, meaning 12 channels were available for the detection of γ-rays. Due to the size of the SPEDE chamber, the angles used by JUROGAMII in the GRAIN sort code for Doppler correction did not correspond to the true angles in the setup, as the target location was not that which is typically used in order to ensure the geometry is correct in GRAIN.

Due to the energy cut-off seen using the particle detector, it was possible to do particle-gating with an increased count rate compared to the November 2015 runs, but Doppler correction with a correct particle velocity was able to be applied. In order to perform some correction, it was possible to plot an expected value for the energy of scattered particles where the PIN diodes were positioned and able to detect scattered nuclei, although this led to a large overall uncertainty due to the uncertainty in this energy. For the first week, an 8-PIN diode array was used, and in the second, 6-PINs.

Two beams were used in the first weekend; ^{132}Xe (22+) and ^{84}Kr (+14), with an energy of 4.1 MeV/u again. In the second week, a ^{197}Au (35+) beam was used. Again, a selection of targets were used throughout; several ^{197}Au (0.38, 1.2, 1.8 mg/cm^2), ^{58}Ni (1 mg/cm^2), ^{170}Yb (1 mg/cm^2), ^{116}Sn (0.5 mg/cm^2), and ^{106}Cd (1.1 mg/cm^2). Calibrations were done, as in November 2014, using a ^{133}Ba source. The resulting calibrated spectrum is seen in Figure 5.17. The PIN diodes were uncalibrated, as the region of interest was not visible since the Mesytec preamplifiers could not be adjusted to a suitable gain such that a true signal could be obtained resulting in a flat top in the output signal. They could however be aligned using this signal, in order to provide a hit for some kinematic correction across all diodes outside of electronic noise. An expected value for the energy was obtained by examining the position of the PIN diodes and working out the expected value of the energy of detected particles across the range of the detectors.

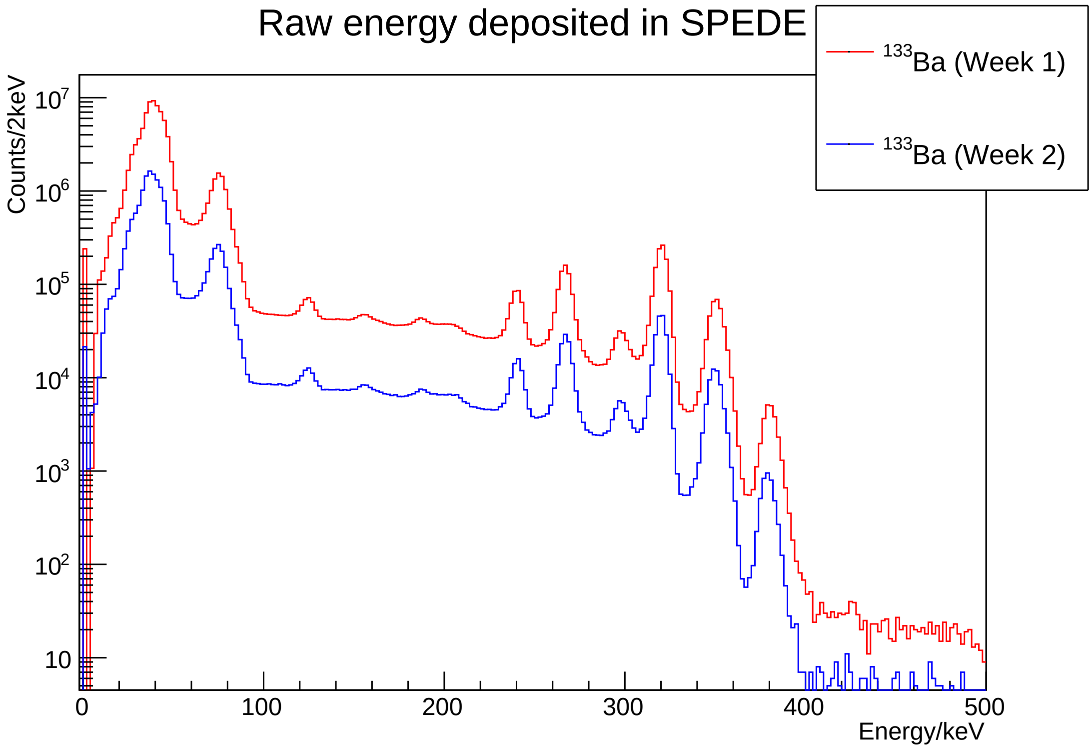

Figure 5.17: Total counts detected by SPEDE from all segments in approximately 280 minutes (week 1) and 60 minutes (week 2) from a ^{133}Ba source. No HV or foils are present, and detector is cooled to approximately -30° C. Note the adjusted thresholds and the effect at low energy. Position of a fitted peak at 320 keV: 320.21(1) keV, FWHM: 7.29(8) keV (slightly worse than initial runs in November 2014).

^{132}Xe (22+) and ^{84}Kr (+14) beams incident on gold targets of varying thicknesses are seen in Figure 5.18, and in Figure 5.19 with HV applied. Assuming a constant number of scattered nuclei are detected with different target thicknesses, a normalisation constant can be applied to see the effect of thickness on δ-electron production. A thicker target results in a smaller low energy peak, but with noticeable straggling in the 100-200 keV range.

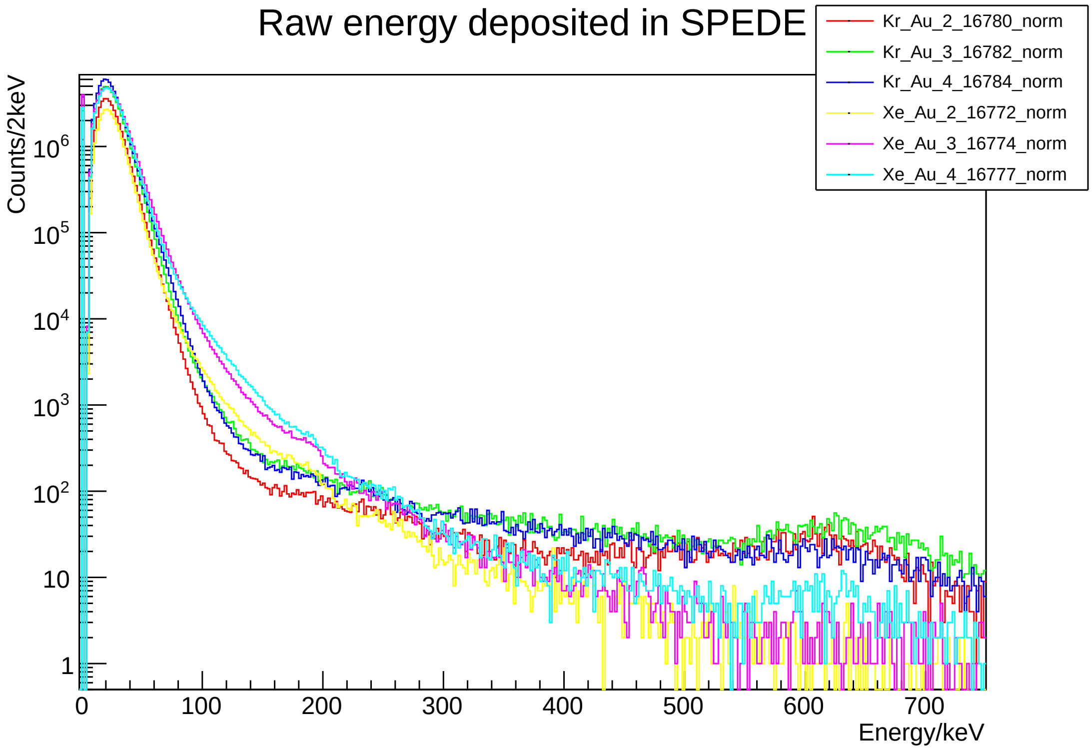

Figure 5.18: ^{132}Xe and ^{84}Kr beams incident on gold targets of various thicknesses.

Efforts were made to look at the effect of placing a foil (aluminised Mylar, foil 1) and light-guard in front of SPEDE again, shown in Figure 5.20. These runs involved an ^{84}Kr beam incident on the second ^{197}Au target (1.1 mg.cm^{-2})). Similar effects are seen when compared to Figure 5.16. Runs are normalised to the number of particles seen during the run.

The second weekend of runs used the 6 PIN diode array. The longest of all runs over the three session was ^{197}Au on ^{197}Au. This makes the kinematics very easy to understand, as the beam and target particles are scattered equally. In Figure 5.21 and Figure 5.22 a shift in energy of 5 keV can be seen in the peaks apparent in the spectra. There is a double peak at 196 (FWHM 22 keV) and 217 keV (FWHM 22 keV). This does not correspond well to expected decay energies for ^{197}Au, which are approximately 188 and 198 keV. The expected yield of electrons from this reaction was calculated using the Coulomb excitation code GOSIA, and is shown in Figure 5.23. This implies the main source of electrons in this reaction is de-excitations of the $\frac{7}{2}^+$ state. With HV on, transitions would be expected at 183 and 193 keV.

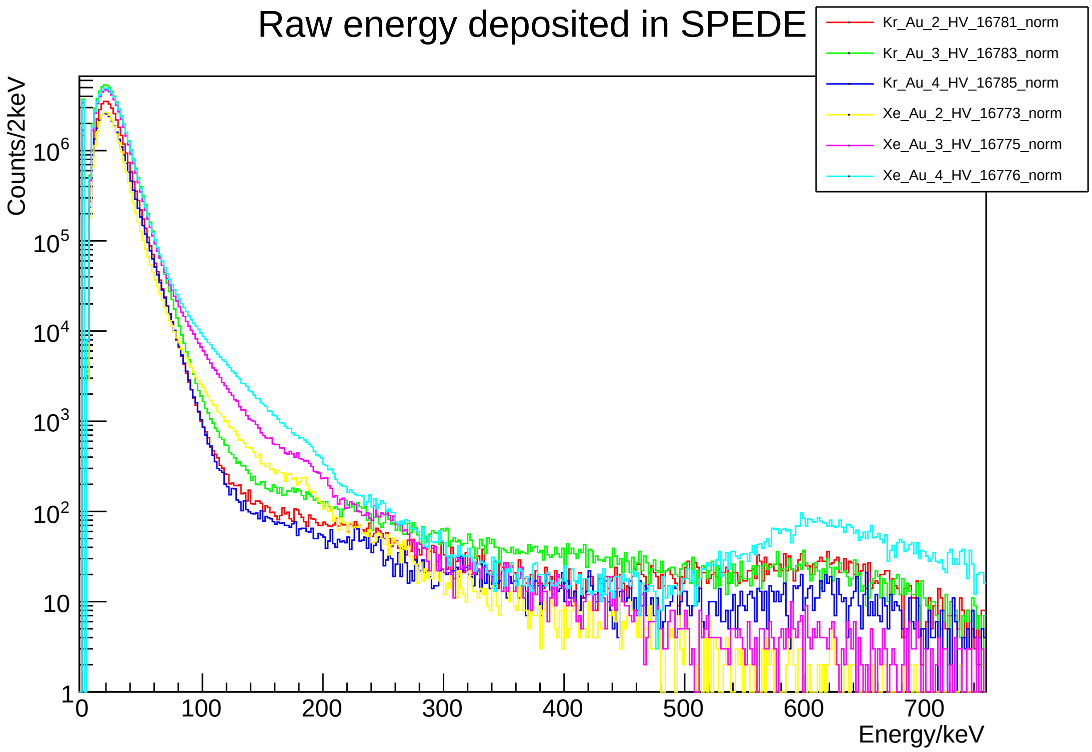

Figure 5.19: ^{132}*Xe and* ^{84}*Kr beams incident on gold targets of various thicknesses (HV).*

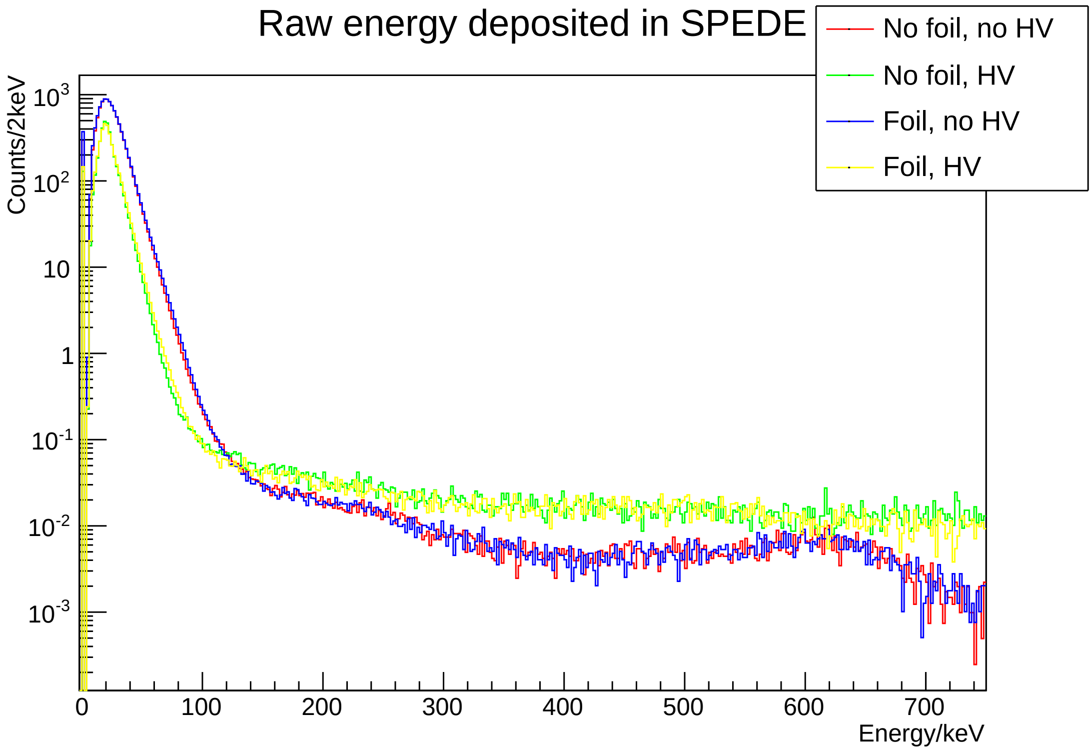

Figure 5.20: ^{84}*Kr on* ^{197}*Au, with & without foil. The higher energy background with foil is lower than without.*

The simulation of ^{197}Au on ^{197}Au, with a transition energy of 198 keV, has a FWHM of 11.7(3) keV, after Doppler correction using the PINS, seen in Figure 4.20. The uncorrected spectrum has a FWHM of 16.9(4) keV centred at 174 keV. This data contained the longest continuous run of data collection using SPEDE in-beam. However, the nuclei scattered in this reaction via Mott scattering. Although the angles and energies can therefore be determined, it is not possible to determine whether the target or the beam nucleus emitted the electron of interest. This then means that the data cannot have a Doppler correction applied.

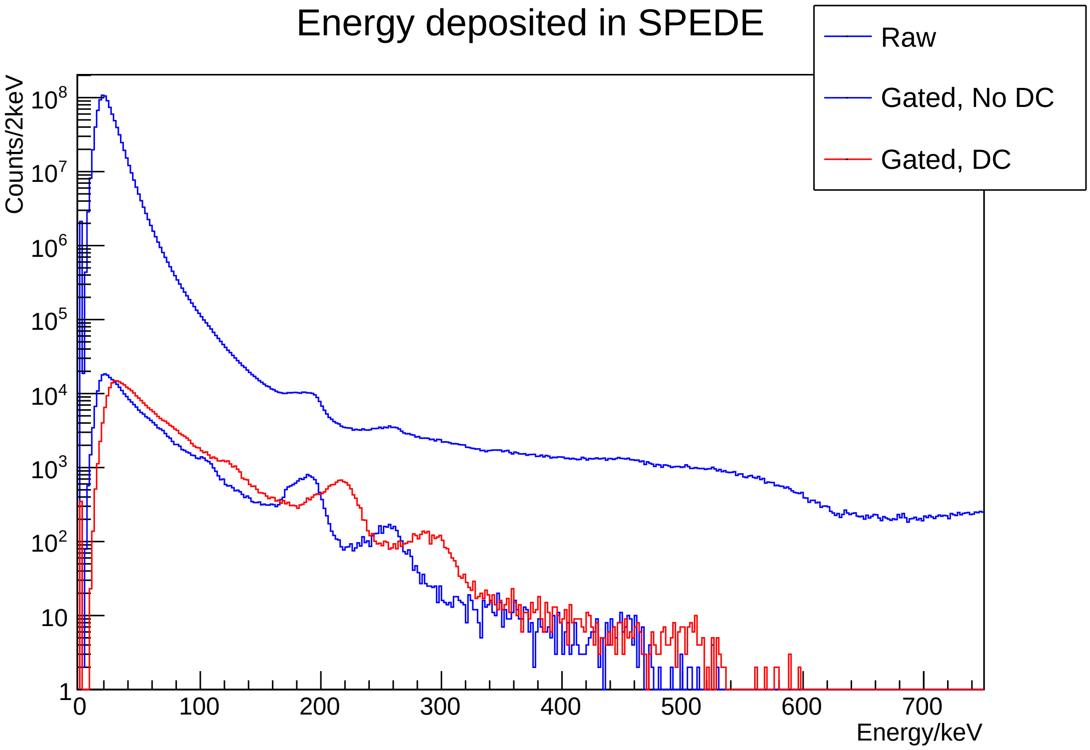

Figure 5.21: ^{197}Au on ^{197}Au. It is not possible to do kinematic correction with this reaction.

5.5 Final commissioning (May)

The second part of commissioning aimed to create usable γ-e$^-$-particle coincidences. A different spectrometer was used, with the same thickness and design as used previously. Additionally, cooling was increased to -40 °C. Only one beam was used; ^{82}Kr (15+), with an energy of 4.3 MeV/u. A ^{197}Au (1.2 mg/cm^2) target was used for the majority of measurements, but data was also collected using ^{106}Cd (1.1 mg/cm^2) and ^{58}Ni (1 mg/cm^2). Calibrations were done, as had been the case in other runs, using a ^{133}Ba source. The resulting calibrated spectrum is seen in Figure 5.24. No foil was used in this run.

Some parameter optimisation was performed, improving resolution by an average of

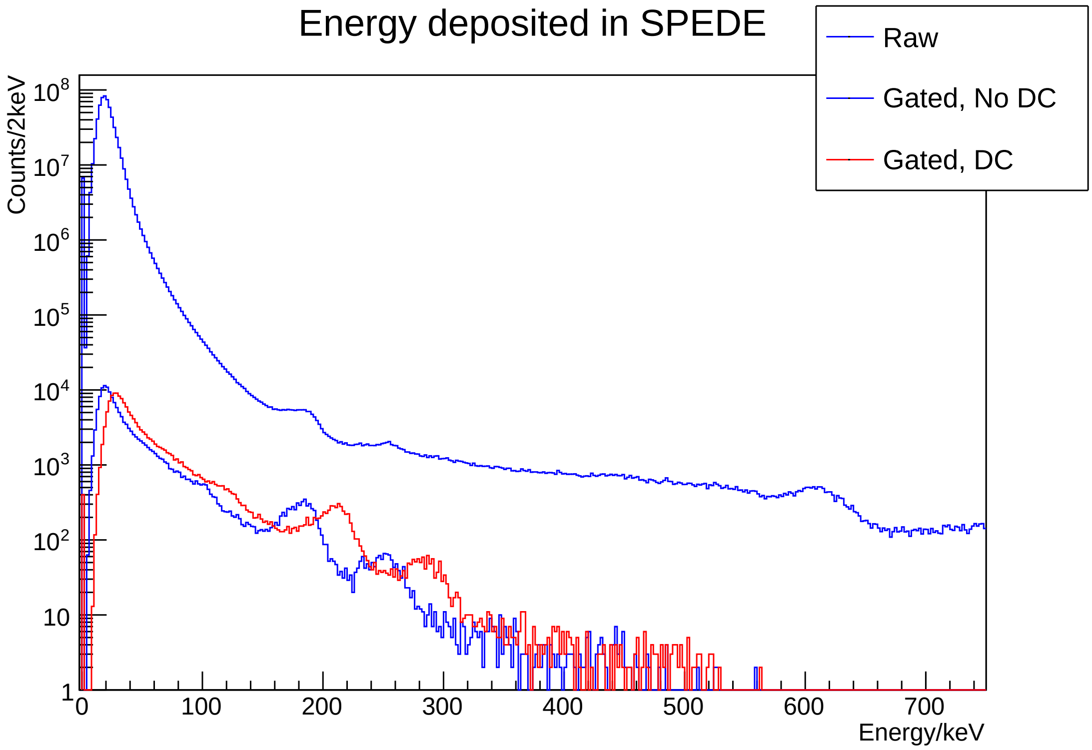

Figure 5.22: ^{197}*Au on* ^{197}*Au (HV). A shift in peaks is observed compared to the runs with no HV.*

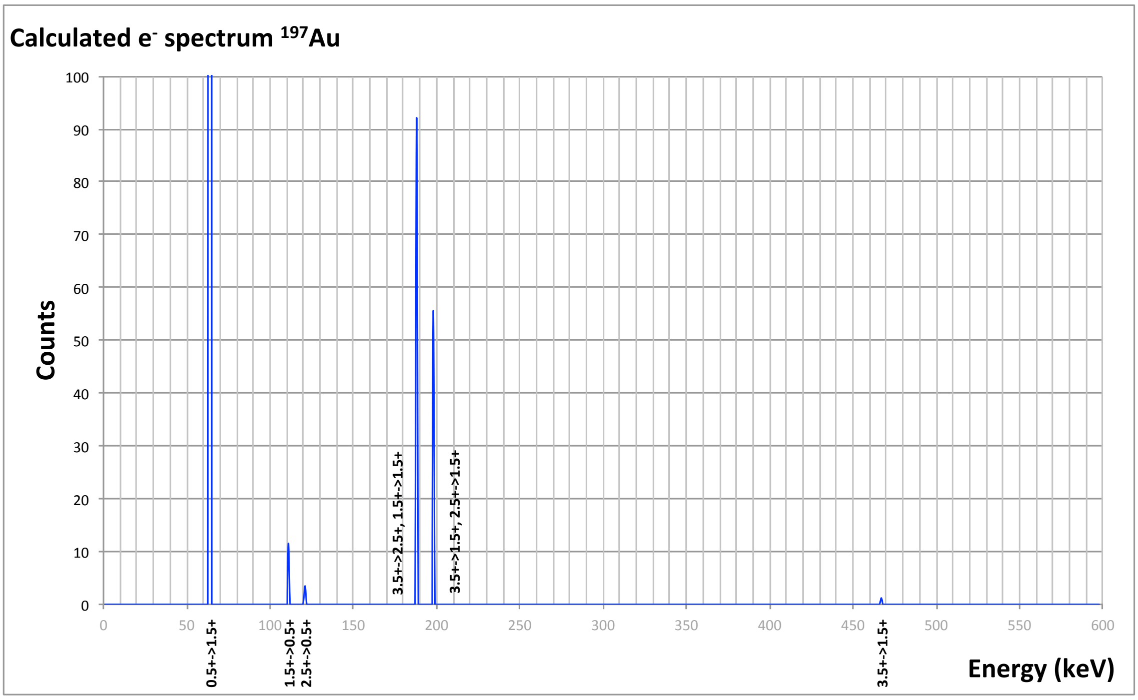

Figure 5.23: Calculated yields of electrons from ^{197}*Au on* ^{197}*Au from GOSIA, normalised to the 279 keV transition between the* $\frac{5}{2}^{+} \rightarrow \frac{1}{2}^{+}$ *transition*

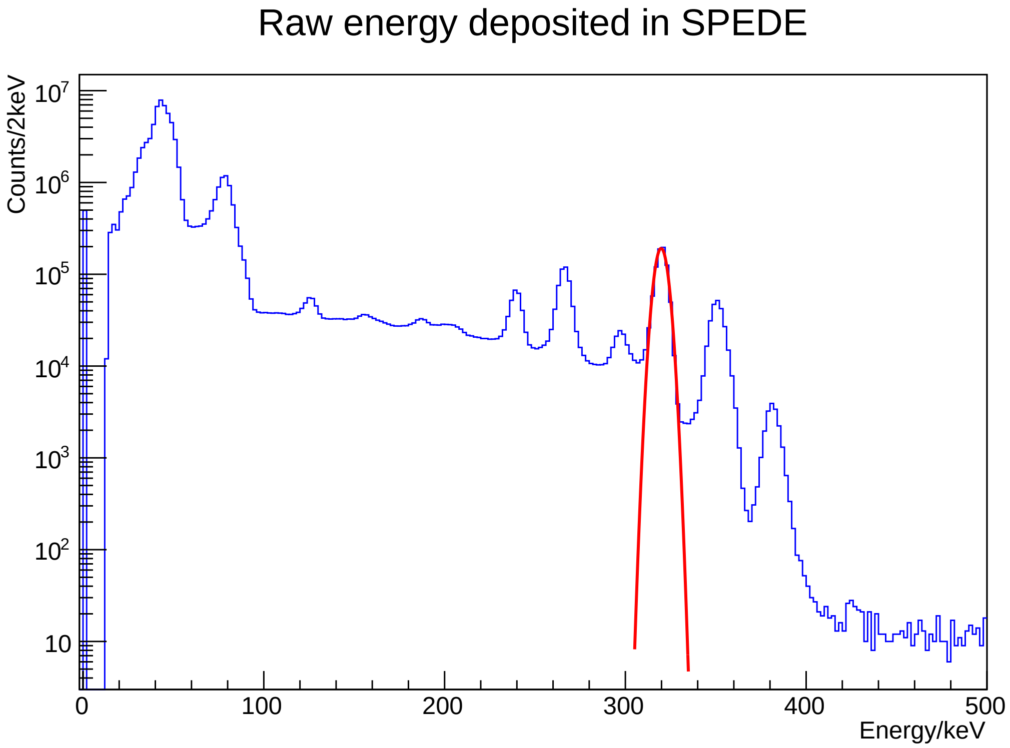

Figure 5.24: Total counts by detected SPEDE from all segments in approximately 170 minutes from a ^{133}*Ba source. No HV or foils are present, and detector is cooled to approximately -°30C. The resolution of each channel that make up this total plot ranged from 6.00 to 7.05 keV. Position of fitted peak: 319.9(4) keV, FWHM: 6.9(1) keV.*

approximately 0.5 keV. The PIN diodes were calibrated using the ^{241}Am source, and were able to be fully utilised for this run. However, only one germanium crystal was used, in a custom position in order to try to obtain γ-spectra with good statistics that can be Doppler corrected precisely.

Using the particle detector, clean gates could be created that allowed for an accurate kinematic correction to be applied. The spectra of uncorrected and corrected data can be seen in Figure 5.25. Correctly aligned peaks are observed after kinematic correction, proving it is possible to do kinematically-corrected in-beam electron spectroscopy.

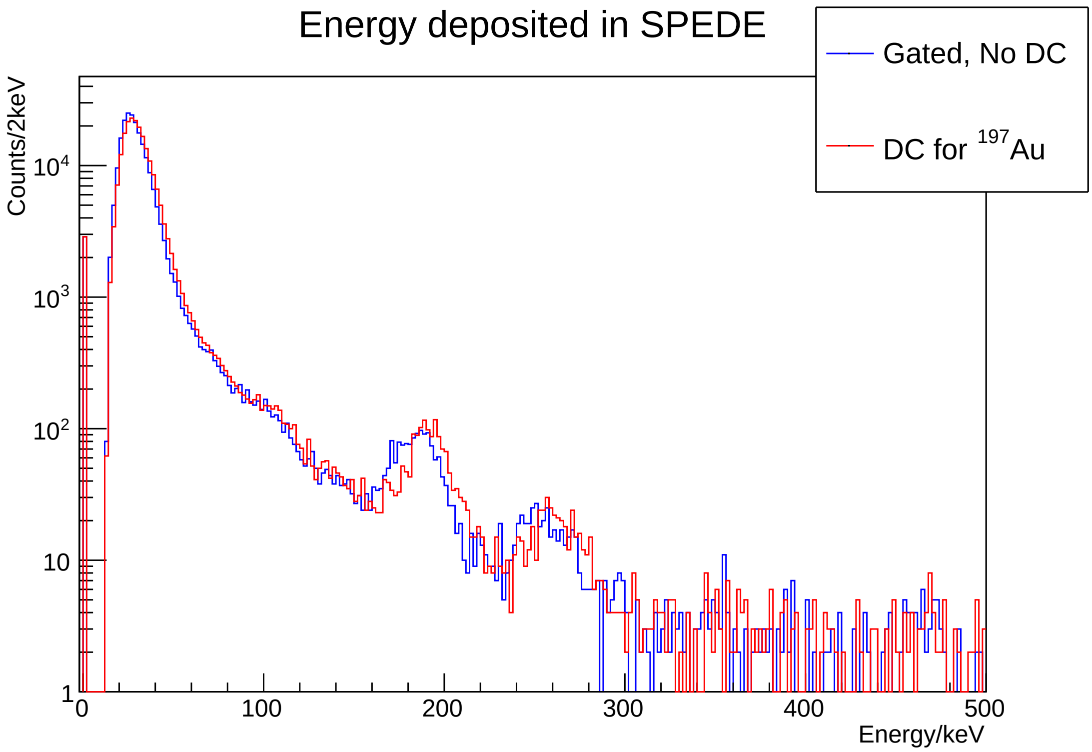

Figure 5.25: Compared to previous figures, the peaks, Doppler corrected for the target, appear much cleaner in this plot of ^{82}*Kr on* ^{197}*Au with HV applied. Centroids for the doublet from the 269 keV and 279 keV transitions appear at 185.6(8) and 195.5(7), with a FWHM of 8.9(9) keV.*

Other beam and target combinations were run, however ^{82}Kr on ^{197}Au provided the best statistics. However, even with this long run only 13 counts could be obtained with particle energy and γ time gates, which offered no statistical significance. A γ-e$^-$ matrix was created without gates as illustrated in Figure 5.26, but the few correlations appear to be mostly random, with a spectrum of γ-radiation in coincidence with the low-energy background in SPEDE.

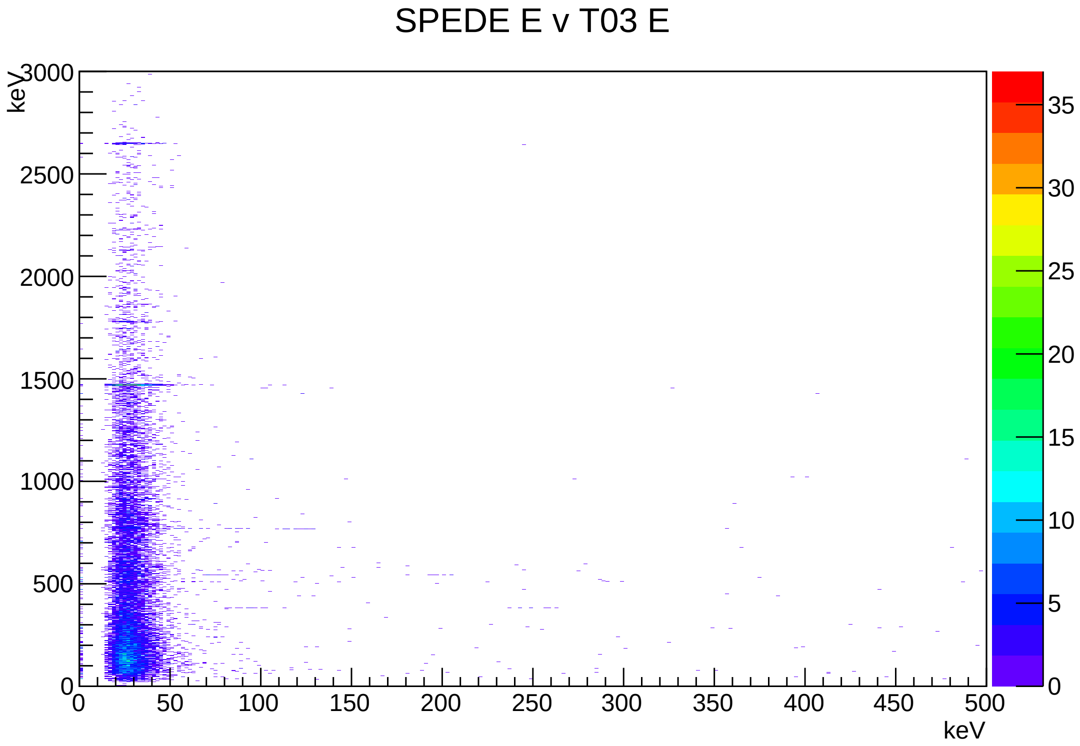

Figure 5.26: ^{82}*Kr on* ^{197}*Au* γ-e^{-} *matrix. Note most coincidences appear in the left hand-side, implying they are random correlations with low-energy pileup within SPEDE, rather than true coincidences from higher-lying gamma-emitting states cascading and being internally converted.*

5.6 Discussion

Improvements in resolution after Doppler correction were better than that predicted by simulations. This may be due to the large intrinsic resolution of 7 keV used to model the simulations. However, there is scope to improve the figure further. Firstly, only quick optimisations were done for Lyrtech parameters. By properly configuring the parameters of the MWD (moving window deconvolution) algorithm, a more precise number can be obtained for the energy of detected electrons. Some improvement was seen between February (Figure 5.17) and May (Figure 5.24). It could also be possible that the low-energy pile-up could affect the resolution, with the high δ production possibly affecting the maximum peak height which is used to shape the trapezoid in the digital electronics. Additionally, the spectra examined most, due to typically having the largest number of counts and the longest experimental runs, were experiments where ^{197}Au was excited. This was an excellent nucleus for studying the performance of an electron spectrometer since it has low-lying states which are highly converted. However, it also has states lying close to each other which result in a double-peak in the resulting spectrum. This has the result of increasing the resolution of fitted peaks depending on the fitting function used, especially in a region where background level changes significantly, although the effect of this is typically minimal if that change is modelled correctly. A further improvement was also seen in the simulated data when using the CD detector that SPEDE will eventually be coupled with. It is therefore reasonable to expect that a similar level of improvement would be expected when using that in final experiments, along with an accurate reading for particle energy.

γ-e^{-}-particle coincidences could not be performed due to low statistics (Figure 5.26). Improvements would be expected when using a full array of detectors, arranged in suitable positions aimed at the target position. Again, this would be expected when coupled with MINIBALL, as each detector is independently adjustable, as opposed to JUROGAM where the frame and detectors are in a fixed position. Although this was resolved in May by aiming an individual phase I detector at the target position, not enough statistics were obtained over runs.

The application of +5 kV applied to the target ladder seemed to significantly alter the distribution of the background electrons without curtailing electrons emitted from the nucleus (beyond shifting them by the expected 5 keV). The impact of foils is more debatable and will require further examination in a test environment where internally converted electron peaks are clearly seen. It would seem that the aluminised foils have a bigger effect on the distribution, but remains to be seen what the effect on resolution would be. It also implies that there may be a large contribution to the low energy peak from ultraviolet light since it is not seen when a simple clear Mylar foil is used. Although a different distribution is seen clearly in Figure 5.16, it is not seen in Figure 5.20, using a thin gold target. The difference could be attributed to a lower δ-electron production rate due to the different densities but principally the thicknesses of the foils. They may be required on a per-case basis; it is shown in Figure 5.18 that heavier beams and thicker targets both result in an increased background, probably as the δ-electron production rate is faster.

The thickness of foils used can be determined from the stopping power of particles in the material using the relation

$$\Delta x = \int_{E1}^{E2} \frac{1}{S(E)} dE. \qquad \text{(eq. 5.1)}$$

where S(E) is stopping power $-\frac{dE}{dx}$. α particles from an ^{241}Am source at the target position were used to determine the thickness of the foils, with results given in Table 5.3. The resultant spectra are seen in Figure 5.27. Since the particles pass through different thicknesses to each different ring, as alphas are incident at different angles from the source, three values were calculated for the thickness and the average was taken to minimise error, ensuring that the cosine of the angle between the beam axis and the ring was used to translate the range that the charged particle was interacting in the material to the true thickness.

Foil	**Thickness**/mg.μm^{-2}
Aluminised Mylar (1)	2.4
Aluminised Mylar (2)	12.8
Mylar	2.0
Aluminium (1 mm hole)	3.4
Aluminium (0.8 mm hole)	1.5

Table 5.3: Foil thicknesses obtained using a ^{241}Am source.

No reliable efficiency data could be collected since the ^{133}Ba source, which emits electrons at a variety of energies so a reliable multi-point calibration can be done, was leaking into the chamber, and the strength could not be reliably determined. Neither were there enough statistics were available to use the known branching ratios of states to be able to determine from excitement of nuclei. Figure 5.28 shows a simulated efficiency plot for SPEDE generated using Geant4, at two different detector distances (2 cm and 2.5 cm).

5.7 Future

SPEDE was shipped to the ISOLDE laboratory at CERN, Geneva, Switzerland, in June 2015. Some initial work has been done to confirm all channels and equipment is working as expected still, and a study using SPEDE in-beam, coupled with the MINIBALL array as intended, took place in November 2015 at the end of the main physics run. This included the full CD detector, and lead to some successful e^{-}-γ-particle coincidence spectroscopy, something not possible at Jyväskylä, but several problems with the setup led to a decision

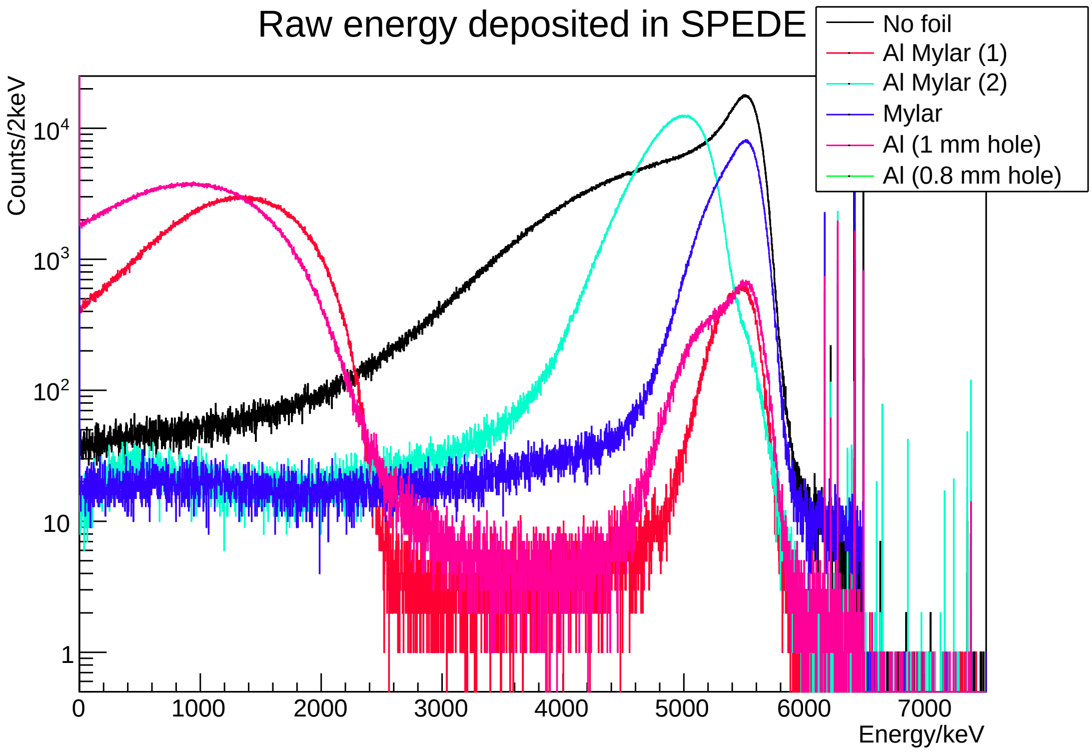

Figure 5.27: ^{241}*Am after passing through various foils, used to determine foil thickness by looking at the attenuation of energy of the main peak.*

being made to take SPEDE back to Finland in order to do further work before final commissioning with radioactive beams. Further tests, after work done in Jyväskylä, will take place in 2016. Already four proposals have been accepted by the ISOLDE and Neutron Time-of-Flight Committee (INTC), and there are four more letters of intent submitted, seen in Table 5.4 and Table 5.5 respectively.

There is also the possibility of ordering thicker detectors in the future, for higher energy requirements. 1000 μm is possible, but a thickness of 1500 μm requires research and development from Micron Semiconductor Ltd, as the laser cutting technique used to produce the silicon detector has not been tried at this thickness before.

5.8 Summary of work

This thesis has presented work on SPEDE, an electron spectrometer tested and commissioned at Jyväskylä, Finland, for use at the HIE-ISOLDE facility at CERN coupled with the MINIBALL array to perform in-beam electron-gamma spectroscopy using post-accelerated radioactive ion beams. Motivation for the need for the detector has also been presented, particular with regards to application on odd-mass transactinide nuclei in the octupole region.

Initial tests took place in Liverpool, UK, as well as at the JYFL facility, with in-

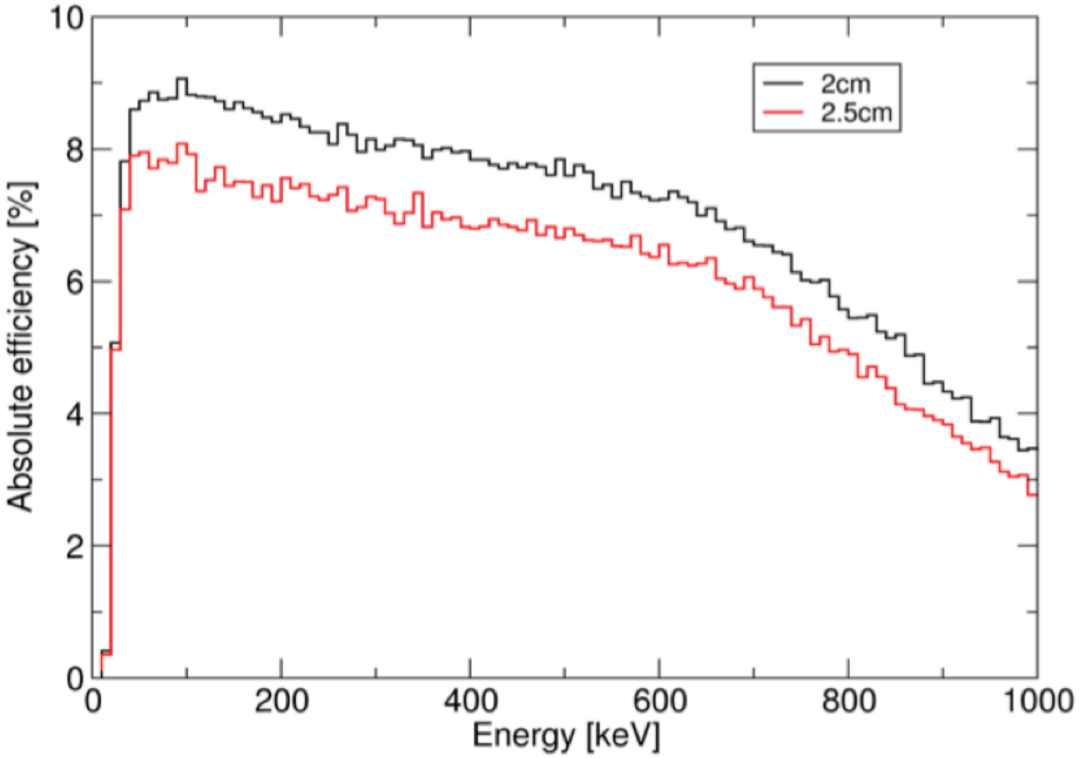

Figure 5.28: Simulated efficiency of SPEDE at 2 and 2.5 cm. An average efficiency of about 8% is seen across the region of interest, dropping rapidly at about 30 keV. Courtesy of D. Cox.

Experiment number	**Experiment name**	**Authors**
IS475	Measurements of octupole collectivity in odd-mass Rn & Ra nuclei using Coulomb excitation	P.A. Butler, D.T. Joss *et al*
IS552	Measurements of octupole collectivity in Rn & Ra nuclei using Coulomb excitation	P.A. Butler, D.T. Joss, M. Scheck *et al*
IS556	Probing intruder configurations in ^{186,188}Pb using Coulomb excitation	J. Pakarinen *et al*
IS563	Coulomb excitation of $^{182-184}$Hg: Shape coexistence in the neutron-deficient lead region	K. Wrzosek-Lipska, D.T. Joss, D.G. Jenkins, J. Pakarinen *et al*

Table 5.4: Accepted proposals by the INTC using the SPEDE spectrometer at HIE-ISOLDE

Experiment name	**Authors**
Measurements of octupole collectivity in odd-mass Rn, Fr & Ra isotopes	P.A. Butler *et al*
Shape studies in the neutron rich $N \approx 60$ region	N. Warr *et al*
Shape coexistence in the neutron-deficient region around $Z = 82$ studied via Coulomb excitation and few-nucleon transfer reactions	P. Van Duppen, D.T. Joss, D.G. Jenkins, J. Pakarinen *et al*
Shape changes and proton-neutron pairing around the $N = Z$ line	D.G. Jenkins *et al*

Table 5.5: Letters of intent for the SPEDE spectrometer at HIE-ISOLDE

beam testing taking place in Finland. A full detector enclosed in the chamber, coupled with electronics and cooling, operated well in an environment similar to what would be expected at the HIE-ISOLDE facility, and in-beam electron spectroscopy without magnetic transport fields was performed for the first time.

Cooling the setup to -30 °C is sufficient enough to get a FWHM of approximately 7 keV at an energy of 320 keV. Effective particle-gating can be used to reduce background significantly and to view peaks clearly, although in this work the efficiency of this was low, and the Doppler correction would be expected to be improved upon deployment to CERN using the CD detector.

Successful physics runs should take place in 2017 at HIE-ISOLDE, CERN.

Bibliography

[1] TD Lee and CN Yang. Conservation of heavy particles and generalized gauge transformations. *Physical Review*, 98(5):1501, 1955.

[2] Ernest Rutherford. The scattering of α and β particles by matter and the structure of the atom. *The London, Edinburgh, and Dublin Philosophical Magazine and Journal of Science*, 21(125):669–688, 1911.

[3] Hans Geiger. On the Scattering of the α-Particles by Matter. *Proceedings of the Royal Society of London. Series A, Containing Papers of a Mathematical and Physical Character*, 81(546):174–177, 1908.

[4] Ernest Rutherford. Nuclear Constitution of Atoms. *Nature*, 105:500–501, 1920.

[5] James Chadwick. Possible existence of a neutron. *Nature*, 129(3252):312, 1932.

[6] E Gapon and D Iwanenko. Zur Bestimmung der isotopenzahl. *Naturwissenschaften*, 20(43):792–793, 1932.

[7] Wolfgang Pauli. The connection between spin and statistics. *Physical Review*, 58(8):716, 1940.

[8] Roger D Woods and David S Saxon. Diffuse surface optical model for nucleon-nuclei scattering. *Physical Review*, 95(2):577, 1954.

[9] LI Schiff. Nuclear Multipole Transitions in Inelastic Electron Scattering. *Physical Review*, 96(3):765, 1954.

[10] BR Fulton. Present and future RIB facilities. In *Journal of Physics: Conference Series*, volume 312, page 052001. IOP Publishing, 2011.

[11] Thomas Nilsson. European RIB facilities–Status and future. *Nuclear Instruments and Methods in Physics Research Section B: Beam Interactions with Materials and Atoms*, 317:194–200, 2013.

[12] D Weisshaar, A Gade, T Glasmacher, GF Grinyer, D Bazin, P Adrich, T Baugher, JM Cook, C Aa Diget, S McDaniel, et al. CAESARA high-efficiency CsI (Na) scintillator array for in-beam γ-ray spectroscopy with fast rare-isotope beams. *Nuclear*

Instruments and Methods in Physics Research Section A: Accelerators, Spectrometers, Detectors and Associated Equipment, 624(3):615–623, 2010.

[13] Marie Sklodowska Curie. *Traité de radioactivité*, chapter IX. Gauthier-Villars, Imprimeur-libraire, 1910.

[14] Nicholas Alfred Jelley. *Fundamentals of nuclear physics*, chapter 4.2. Cambridge University Press, 1990.

[15] PA Butler and W Nazarewicz. Intrinsic reflection asymmetry in atomic nuclei. *Reviews of Modern Physics*, 68(2):349, 1996.

[16] B Bucher, S Zhu, CY Wu, RVF Janssens, D Cline, AB Hayes, M Albers, AD Ayangeakaa, PA Butler, CM Campbell, et al. Direct Evidence of Octupole Deformation in Neutron-Rich Ba 144. *Physical review letters*, 116(11):112503, 2016.

[17] GA Leander, RK Sheline, P Möller, P Olanders, I Ragnarsson, and AJ Sierk. The breaking of intrinsic reflection symmetry in nuclear ground states. *Nuclear Physics A*, 388(3):452–476, 1982.

[18] X Li. Exotic nuclear deformations in nuclei around 218Ra. *Progress in Particle and Nuclear Physics*, 28:435–436, 1992.

[19] JF Smith, JFC Cocks, N Schulz, M Aiche, M Bentaleb, PA Butler, F Hannachi, GD Jones, PM Jones, R Julin, et al. Contrasting Behavior in Octupole Structures Observed at High Spin in 220 Ra and 222 Th. *Physical review letters*, 75(6):1050, 1995.

[20] PA Butler and W Nazarewicz. Intrinsic dipole moments in reflection-asymmetric nuclei. *Nuclear Physics A*, 533(2):249–268, 1991.

[21] Liam Paul Gaffney, Peter A Butler, Marcus Scheck, Adam B Hayes, Frederik Wenander, Michael Albers, Beyhan Bastin, Christopher Bauer, Andrey Blazhev, Sabine Bönig, et al. Studies of pear-shaped nuclei using accelerated radioactive beams. *Nature*, 497(7448):199–204, 2013.

[22] Tim Chupp. Permanent electric dipole moments of atoms and molecules. *Advances In Atomic, Molecular, and Optical Physics*, 59:129–174, 2010.

[23] Liam Paul Gaffney. *Octupole collectivity in 220Rn and 224Ra.* PhD thesis, University of Liverpool, 2012.

[24] J Dobaczewski and J Engel. Nuclear Time-Reversal Violation and the Schiff Moment of Ra 225. *Physical review letters*, 94(23):232502, 2005.

[25] Irshad Ahmad and PA Butler. Octupole shapes in nuclei. *Annual Review of Nuclear and Particle Science*, 43(1):71–116, 1993.

[26] GA Leander and YS Chen. Reflection-asymmetric rotor model of odd A 219–229 nuclei. *Physical Review C*, 37(6):2744, 1988.

[27] GA Leander and RK Sheline. Intrinsic reflection asymmetry in odd-A nuclei. *Nuclear Physics A*, 413(3):375–415, 1984.

[28] Raymond K Sheline and PC Sood. Octupole deformation at high spin in the Ba-Sm region. *Physical Review C*, 34(6):2362, 1986.

[29] AN Andreyev, Marc Huyse, Piet Van Duppen, L Weissman, D Ackermann, J Gerl, FP Hessberger, S Hofmann, A Kleinböhl, G Münzenberg, et al. A triplet of differently shaped spin-zero states in the atomic nucleus 186Pb. *Nature*, 405(6785):430–433, 2000.

[30] C Walz, H Scheit, N Pietralla, T Aumann, R Lefol, and V Yu Ponomarev. Observation of the competitive double-gamma nuclear decay. *Nature*, 526(7573):406–409, 2015.

[31] John L Wood. Do we understand excited 0+ states in nuclei? In *Journal of Physics: Conference Series*, volume 403, page 012011. IOP Publishing, 2012.

[32] JL Wood, Kristiaan Heyde, W Nazarewicz, Marc Huyse, and Piet Van Duppen. Coexistence in even-mass nuclei. *Physics reports*, 215(3-4):101–201, 1992.

[33] Kris Heyde and John L Wood. Shape coexistence in atomic nuclei. *Reviews of Modern Physics*, 83(4):1467, 2011.

[34] RR Chasman. Incipient octupole deformation and parity doublets in the odd mass light actinides. *Physics Letters B*, 96(1-2):7–10, 1980.

[35] CW Raman and S Bhagavantam. Experimental Proof of the Spin of the Photon. *Satyendra Nath Bose â His Life and Times*, page 388, 1932.

[36] A Cambi, TF Fazzini, A Giannatiempo, and PR Maurenzig. A compact electron spectrometer for in-beam measurements of internal conversion coefficients. *Nuclear Instruments and Methods*, 103(2):331–335, 1972.

[37] S Ketelhut, LJ Evitts, AB Garnsworthy, C Bolton, GC Ball, R Churchman, R Dunlop, G Hackman, R Henderson, M Moukaddam, et al. Simulated performance of the in-beam conversion-electron spectrometer, SPICE. *Nuclear Instruments and Methods in Physics Research Section A: Accelerators, Spectrometers, Detectors and Associated Equipment*, 753:154–163, 2014.

[38] Isaac Newton. *PhilosophiæNaturalis Principia Mathematica*, chapter Axioms or Laws of Motion. Londini, Jussu Societatis Regiæac Typis Josephi Streater, 1687.

[39] AH Wapstra, D Maeder, GJ Nijgh, and L Th M Ornstein. The decay of 203Hg, 203Pb and 201Pb. *Physica*, 20(1-6):169–177, 1954.

[40] IM Band, MB Trzhaskovskaya, CW Nestor, PO Tikkanen, and S Raman. Dirac–Fock internal conversion coefficients. *Atomic Data and Nuclear Data Tables*, 81(1):1–334, 2002.

[41] JL Wood, EF Zganjar, Caroline De Coster, and Kristiaan Heyde. Electric monopole transitions from low energy excitations in nuclei. *Nuclear Physics A*, 651(4):323–368, 1999.

[42] JL Wood, EF Zganjar, and Kristiaan Heyde. The strength of electric monopole transitions and the decay out of superdeformed bands. *Zeitschrift für Physik A Hadrons and Nuclei*, 353(4):355–356, 1996.

[43] A Kuhnert, EA Henry, TF Wang, MJ Brinkman, MA Stoyer, JA Becker, DR Manatt, and SW Yates. Search for an M0 transition in Yb 170. *Physical Review C*, 47(5):2386, 1993.

[44] VF Weisskopf. Radiative transition probabilities in nuclei. *Physical Review*, 83(5):1073, 1951.

[45] Morris E Rose and George E Uhlenbeck. The Formation of Electron-Positron Pairs by Internal Conversion of γ-Radiation. *Physical Review*, 48(3):211, 1935.

[46] Roland J Lombard, Charles F Perdrisat, and Jean H Brunner. Internal pair formation and multipolarity of nuclear transitions. *Nuclear Physics A*, 110(1):41–55, 1968.

[47] K Alder and A Winther. Theory of Coulomb Excitation. *Physical Review*, 96(1):237, 1954.

[48] D Cline et al. Gosia User Manual for Simulation and Analysis of Coulomb Excitation Experiments. *Gosia Steering Committee*, 18:19–60, 2012.

[49] C Amsler et al. Pdg. Particle Data Group. *PL B667*, 1, 2008.

[50] HW Koch and JW Motz. Bremsstrahlung cross-section formulas and related data. *Reviews of modern physics*, 31(4):920, 1959.

[51] William Shockley. Currents to conductors induced by a moving point charge. *Journal of applied physics*, 9(10):635–636, 1938.

[52] U Bechthold, S Hagmann, J Ullrich, B Bathelt, A Bohris, R Moshammer, U Ramm, C Bhalla, G Kraft, and H Schmidt-Böcking. Intra-atomic double scattering of binary encounter electrons in collisions of fast heavy ions with atoms and molecules. *Physical review letters*, 79(11):2034, 1997.

[53] Ernest Rutherford. The magnetic and electric deviation of the easily absorbed rays from radium. *The London, Edinburgh, and Dublin Philosophical Magazine and Journal of Science*, 5(26):177–187, 1903.

[54] MB Chadwick, P Obložinskỳ, M Herman, NM Greene, RD McKnight, DL Smith, PG Young, RE MacFarlane, GM Hale, SC Frankle, et al. ENDF/B-VII. 0: next generation evaluated nuclear data library for nuclear science and technology. *Nuclear data sheets*, 107(12):2931–3060, 2006.

[55] Arthur H Compton. A quantum theory of the scattering of X-rays by light elements. *Physical review*, 21(5):483, 1923.

[56] JH Hubbell. Electron–positron pair production by photons: A historical overview. *Radiation Physics and Chemistry*, 75(6):614–623, 2006.

[57] Ugo Amaldi and Gerhard Kraft. Radiotherapy with beams of carbon ions. *Reports on progress in physics*, 68(8):1861, 2005.

[58] J David Jackson and John M Blatt. The interpretation of low energy proton-proton scattering. *Reviews of Modern Physics*, 22(1):77, 1950.

[59] TW Crane and MP Baker. Neutron detectors. *Passive Nondestructive Assay of Nuclear Materials*, pages 379–406, 1991.

[60] Peter R Menge, G Gautier, A Iltis, C Rozsa, and V Solovyev. Performance of large lanthanum bromide scintillators. *Nuclear Instruments and Methods in Physics Research Section A: Accelerators, Spectrometers, Detectors and Associated Equipment*, 579(1):6–10, 2007.

[61] Glenn F Knoll. *Radiation detection and measurement.* John Wiley & Sons, 2010.

[62] V Drndarevic, P Ryge, and T Gozani. Digital signal processing for high rate gamma-ray spectroscopy. *Nuclear Instruments and Methods in Physics Research Section A: Accelerators, Spectrometers, Detectors and Associated Equipment*, 277(2-3):532–536, 1989.

[63] S Paschalis, IY Lee, AO Macchiavelli, CM Campbell, M Cromaz, S Gros, J Pavan, J Qian, RM Clark, HL Crawford, et al. The performance of the gamma-ray energy tracking in-beam nuclear array GRETINA. *Nuclear Instruments and Methods in*

Physics Research Section A: Accelerators, Spectrometers, Detectors and Associated Equipment, 709:44–55, 2013.

[64] S Akkoyun, Alejandro Algora, B Alikhani, F Ameil, G De Angelis, L Arnold, A Astier, Ayşe Ataç, Y Aubert, C Aufranc, et al. Agataadvanced gamma tracking array. *Nuclear Instruments and Methods in Physics Research Section A: Accelerators, Spectrometers, Detectors and Associated Equipment*, 668:26–58, 2012.

[65] John Simpson. The AGATA project. In *Journal of Physics: Conference Series*, volume 41, page 72. IOP Publishing, 2006.

[66] MP Metlay, JX Saladin, IY Lee, and O Dietzsch. The ICEBall: a multiple element array for in-beam internal conversion electron spectroscopy. *Nuclear Instruments and Methods in Physics Research Section A: Accelerators, Spectrometers, Detectors and Associated Equipment*, 336(1):162–170, 1993.

[67] W Neumann, L Cleemann, J Eberth, N Wiehl, and V Zobel. Details of conversion electron spectroscopy with mini-orange spectrometers. *Nuclear Instruments and Methods*, 164(3):539–545, 1979.

[68] J Van Klinken, SJ Feenstra, K Wisshak, and H Faust. Mini-orange spectrometers for in-and off-beam observation of conversion electrons. *Nuclear Instruments and Methods*, 130(2):427–441, 1975.

[69] PA Butler, PM Jones, KJ Cann, JFC Cocks, GD Jones, R Julin, and WH Trzaska. Electron spectroscopy using a multi-detector array. *Nuclear Instruments and Methods in Physics Research Section A: Accelerators, Spectrometers, Detectors and Associated Equipment*, 381(2):433–442, 1996.

[70] PA Butler, RD Humphreys, PT Greenlees, R-D Herzberg, DG Jenkins, GD Jones, H Kankaanpää, H Kettunen, P Rahkila, C Scholey, et al. Conversion Electron Cascades in N 102 254 o. *Physical review letters*, 89(20):202501, 2002.

[71] J Uusitalo, P Jones, P Greenlees, P Rahkila, M Leino, AN Andreyev, PA Butler, T Enqvist, K Eskola, T Grahn, et al. In-beam spectroscopy using the JYFL gas-filled magnetic recoil separator RITU. *Nuclear Instruments and Methods in Physics Research Section B: Beam Interactions with Materials and Atoms*, 204:638–643, 2003.

[72] P Papadakis, R-D Herzberg, J Pakarinen, PT Greenlees, J Sorri, PA Butler, PJ Coleman-Smith, D Cox, JR Cresswell, K Hauschild, et al. The SAGE spectrometer: A tool for combined in-beam γ-ray and conversion electron spectroscopy. In *Journal of Physics: Conference Series*, volume 312, page 052017. IOP Publishing, 2011.

[73] J Pakarinen, P Papadakis, J Sorri, R-D Herzberg, PT Greenlees, PA Butler, PJ Coleman-Smith, DM Cox, JR Cresswell, P Jones, et al. The SAGE spectrometer. *The European Physical Journal A*, 50(3):1–11, 2014.

[74] B Harss, RC Pardo, KE Rehm, F Borasi, JP Greene, RVF Janssens, CL Jiang, J Nolen, M Paul, JP Schiffer, et al. Production of radioactive ion beams using the in-flight technique. *Review of Scientific Instruments*, 71(2):380–387, 2000.

[75] Otto Kofoed-Hansen and Karl Ove Nielsen. MEASUREMENTS ON SHORT-LIVED RADIOACTIVE KRYPTON ISOTOPES FROM FISSION AFTER ISOTOPIC SEPARATION. *Kgl. Danske Videnskab. Selskab, Mat.-fys. Medd.*, 26, 1951.

[76] Y Blumenfeld, Thomas Nilsson, and Piet Van Duppen. Facilities and methods for radioactive ion beam production. *Physica Scripta*, 2013(T152):014023, 2013.

[77] M Lindroos, Peter A Butler, Marc Huyse, and Karsten Riisager. Hie-Isolde. *Nuclear Instruments and Methods in Physics Research Section B: Beam Interactions with Materials and Atoms*, 266(19):4687–4691, 2008.

[78] Erich Kugler. The ISOLDE facility. *Hyperfine interactions*, 129(1-4):23–42, 2000.

[79] MJG Borge. Highlights of the ISOLDE facility and the HIE-ISOLDE Project. *Nuclear Instruments and Methods in Physics Research Section B: Beam Interactions with Materials and Atoms*, 376:408–412, 2016.

[80] William R Leo. *Techniques for nuclear and particle physics experiments: a how-to approach*, chapter 14. Springer Science & Business Media, 2012.

[81] Luigi Bardelli. *Development of sampling and digital signal processing techniques with applications to Nuclear Physics detectors.* PhD thesis, Firenze Univ., 2005.

[82] A Georgiev, W Gast, and RM Lieder. An analog-to-digital conversion based on a moving window deconvolution. *IEEE transactions on nuclear science*, 41(4):1116–1124, 1994.

[83] Lars Evensen, Anders Hanneborg, Berit Sundby Avset, and Martin Nese. Guard ring design for high voltage operation of silicon detectors. *Nuclear Instruments and Methods in Physics Research Section A: Accelerators, Spectrometers, Detectors and Associated Equipment*, 337(1):44–52, 1993.

[84] J Konki, P Papadakis, J Pakarinen, PA Butler, P Davies, PT Greenlees, RD Herzberg, Mark Huyse, DG Jenkins, R Julin, et al. Combined in-beam gamma-ray and conversion electron spectroscopy with radioactive ion beams-Simulations of a silicon detector for the SPEDE spectrometer. In *EPJ Web of Conferences*, volume 63, page 01019. EDP Sciences, 2013.

[85] Martin J Berger. ESTAR, PSTAR, and ASTAR: Computer programs for calculating stopping-power and range tables for electrons, protons, and helium ions. *Unknown*, 1992.

[86] BL Wall, John F Amsbaugh, A Beglarian, T Bergmann, HC Bichsel, LI Bodine, NM Boyd, Tom H Burritt, Z Chaoui, TJ Corona, et al. Dead layer on silicon p–i–n diode charged-particle detectors. *Nuclear Instruments and Methods in Physics Research Section A: Accelerators, Spectrometers, Detectors and Associated Equipment*, 744:73–79, 2014.

[87] Lutz Handschug, Helmut Backe, and Helmut Bokemeyer. A kinematic Doppler correction method for high resolution in-beam conversion electron spectroscopy after (HI, xn) reactions. *Nuclear Instruments and Methods*, 161(1):117–122, 1979.

[88] OFCOM. UK Frequency Allocation Table, availale at https://www.ofcom.org.uk/spectrum/information/uk-fat.

[89] Vinzenz Bildstein, Roman Gernhäuser, Thorsten Kröll, Reiner Krücken, Kathrin Wimmer, Piet Van Duppen, Mark Huyse, Nikolas Patronis, Riccardo Raabe, T-REX Collaboration, et al. T-rex. *The European Physical Journal A*, 48(6):1–10, 2012.

[90] Esko Liukkonen. New K130 cyclotron at Jyväskylä. 1992.

[91] P Rahkila. Graina java data analysis system for total data readout. *Nuclear Instruments and Methods in Physics Research Section A: Accelerators, Spectrometers, Detectors and Associated Equipment*, 595(3):637–642, 2008.

[92] Sea Agostinelli, John Allison, K al Amako, J Apostolakis, H Araujo, P Arce, M Asai, D Axen, S Banerjee, G Barrand, et al. GEANT4a simulation toolkit. *Nuclear instruments and methods in physics research section A: Accelerators, Spectrometers, Detectors and Associated Equipment*, 506(3):250–303, 2003.

[93] Francesc Salvat, José M Fernández-Varea, and Josep Sempau. PENELOPE-2006: A code system for Monte Carlo simulation of electron and photon transport. In *Workshop proceedings*, volume 7, 2006.

[94] Jürgen Theuerkauf. *Die Analyse von zwei-und mehrdimensionalen yy-Koinzidenzspektren an Beispielen aus Hochspinexperimenten in der Massengegend um 146 Gd.* PhD thesis, Universität zu Köln, 1994.

[95] NNDC ENSDF. online data service, ENSDF database, 2015.